Systems Engineering For Optically Pumped Magnetometry

A thesis presented in candidature for the degree Doctor of Philosophy.

Written By

MARCIN SZYMON MROZOWSKI

The University of Strathclyde
Department of Physics
Glasgow, Scotland

2023

Declaration of Authors Rights

Abstract

This thesis describes the design, development, testing and evaluation of instrumentation designed to work with and enable the performance of spin-exchange relaxation-free magnetometers. The instrumentation includes ultra-low noise bi-polar current sources for driving magnetic field nulling coils and exhibiting ≈ 15 ppb/$\sqrt{\text{Hz}}$ wideband noise and narrow 1/f noise bandwidth of 1 Hz. Custom photodetectors featuring very low noise of ≈ 52 nV/$\sqrt{\text{Hz}}$ after 100 Hz for transimpedance gain of 150 kV/A were designed, built, and characterised. The detector also features adjustable gain and bandwidth, with the ability to accept a range of photodiodes to suit different applications. A custom laser driver for driving vertical-cavity surface-emitting (VCSELs) lasers was also developed, featuring very low current noise of 40 pA/$\sqrt{\text{Hz}}$ at 10 Hz and diode temperature controller capable of stabilising the temperature to < 0.5 mK.

The thesis also describes the development of two, spin-exchange relaxation-free magnetometers. One utilising ^{87}Rb, which is a lab-based experiment and a portable sensor that uses ^{133}Cs as its alkali species. Both experiments benefit from custom instrumentation developed, achieving ultimate sensitivity of 24.7 fT/$\sqrt{\text{Hz}}$ and 90 fT/$\sqrt{\text{Hz}}$ respectively.

Additionally, the thesis describes an investigation of low-power and low-intensity noise vertical-cavity surface-emitting lasers as an alternative coherent light source to distributed Bragg reflector lasers commonly used for optically pumped magnetometers. The change to inexpensive and power-efficient laser light sources offers a benefit for the development of portable magnetometers.

Acknowledgements

With the completion of my project work and thesis writing, I would like to express my gratitude to the people who have helped me during the duration of my PhD.

First and foremost, I would like to thank my supervisors for their unwavering support throughout the duration of my PhD. To my primary supervisor, Paul F. Griffin for his guidance, support, help with revisions and countless chats that we had related and unrelated to the project work. To my second supervisor, Erling Riis for his insight, guidance, and approval of all my electronic components orders. My supervisor's help and guidance allowed me to become a better researcher.

I would like to extend my gratitude and thanks to Iain Chalmers, for his guidance, support, never-ending patience with the revisions of the thesis and the paper, and also for all of the chats about electronics and life.

I would also like to thank all of the members of SERF team: Rach Dawson, Dominic Hunter, Ed Irwin and Carolyn O'Dwyer. This project would not have been successfully completed without their contribution, knowledge exchange and enthusiasm. Special thanks go to research fellow, Stuart J. Ingleby for his guidance and support throughout project work. I would also like to thank all of the members of the magnetometry team for their useful discussions.

My thanks also go to the examination committee: Alessandro Rossi and Kevin Weatherill for the engaging discussions and guidance on the improvement of my thesis. Special thanks also go to my examination convener, James McGilligan for organising the examination.

Finally, this PhD journey could not have been completed without the support of my family and friends who were there for me when I was struggling. I want to thank my parents for their love, support and for keeping my spirits up. I would also like to thank my brother, for joining me for PhD work and the engaging discussions and knowledge exchange that we had during the duration of my PhD.

CONTENTS

List of Figures

List of Tables

List of Acronyms

Chapter 1

Introduction

The earliest known use case for observation of magnetic effect was for navigation. One of the earliest instrument examples being a polished spoon made out of lodestone, which when set on a flat surface, the handle would show the direction of magnetic south. The first example of magnetisation and use for navigation other than lodestone was "directional fish" which was a thin strip of iron made to reassemble a fish. The iron was placed in a coal fire and after becoming red-hot the "tail" of the instrument was quenched while being magnetised by the lodestone [1]. The shape allowed the device better directional accuracy than the spoon and allowed it to float on water. Only later, compass needles made out of iron were developed.

The earliest examples of magnetometers only provided the ability to measure the direction but not the absolute field strength. It would take until 1832 when Carl Fredrich Gauss was able to measure the absolute magnetic field of the Earth [2]. The instrument consisted of a magnet suspended by a silk thread over a scale, where the oscillations produced by the movement of the magnet due to geo-magnetic influence were observed as a reflection of scale on the telescope and recorded. This method is believed to have been accurate to within 1% and commonly used right into the 20th century.

The work of Hans Christian Ørsted in 1820, provided a link between electric current and magnetism when he observed that a compass needle deflects under the influence of electric current flowing through the wire close to the compass needle [3]. This brought interest to the idea of electromagnetism and spun much research into this topic.

One of the results of Ørsted's experiment was Michael Faraday's work into the magneto-optical phenomenon, today known as the Faraday rotation effect [4]. Where a linearly polarised light was used to pass through a piece of leaded glass and under influence of a magnetic field along the axis of the light, the polarisation of the light through the medium can be rotated. Depending on the magnetic field strength applied, the rotation could be varied.

This experiment was recreated by Macaluso and Corbino in 1898, but this time in an atomic vapour [5] to further the understanding of the Faraday effect. In the experiment, they used a sodium sample illuminated by sunlight, close to the absorption lines and altered the magnetic field applied. Through this, they noted an increase in the optical rotation when the light was in resonance with the absorption resonance of the sodium sample, laying the foundation for what would become the optically pumped magnetometers (OPMs) used today.

OPMs are devices that utilise the principles of optical pumping, through means of lasers or discharge lamps [6, 7], for the formation of a magnetically sensitive state in the medium [6, 8] and are ultimately used for the detection of magnetic fields. OPMs are very sensitive devices, which historically (1970s) were capable of achieving magnetic sensitivities up to 100 $\mathrm{fT}/\sqrt{\mathrm{Hz}}$ [9, 10] and in the early 2000s this was improved to levels previously only reserved for Super Conducting Quantum Interference Devices (SQUIDs) [11] which exploit the Josephson junctions that require cryogenic cooling for operation [12]. This sensitivity was further increased in 2002, by operating the magnetometer in a spin-exchange relaxation-free (SERF) regime (explored in Chapter 2) which is a region of high atomic vapour density at near zero magnetic fields [13]. This new regime allowed it to achieve aT sensitivity [14] making it more sensitive than SQUIDs, albeit working only at near zero magnetic fields (< 20 nT) and with limited bandwidth (< 30 Hz). In addition, the sensor was developed to explore the physical limits of the scheme rather than the practical limits. As such practical devices typically achieve fT sensitivities.

Advances in microfabrication of vapour cells and miniaturised laser light sources allowed for building these sensors into compact, portable devices [15–17].

These advances in sensitivity and useability make OPMs, using different interrogation methods ideally suited for a myriad of high sensitivity applications ranging from: biomedical [16, 18–21], geophysics [22, 23], low field nuclear magneto resonance (NMR) [24, 25], electromagnetic induction imaging [26, 27], defence [28] and fundamental science [29, 30].

However, the sensitivity offered by OPMs can be easily spoiled by the use of inadequate instrumentation that will limit their performance. This is primarily due to over-reliance on commercial off-the-shelf (COTS) instrumentation in the laboratory which targets a broad range of tasks but does not target specific applications required by an OPM. Another issue, in particular, is the lack of instrumentation designed to work for moving the sensors which are lab-based experiments into practical portable devices. A prospect of a portable device that requires multiple high-end COTS instruments quickly diminishes its value as a commercially viable product, or worse cannot be realised at all because it is unsuitable.

Another aspect that is important for compact devices is their size, weight and power (SWaP), which is crucial for applications that require multiple sensors, such as whole head magnetoencephalography (MEG) [21, 31]. This is difficult to realise with lab-based instrumentation, which might be more suited for lab-based proof of concept solutions rather than application based ones that provide more constraints.

The work presented in this thesis aims to address some of these issues by looking at the process of design, development, testing and evaluation of custom instrumentation aimed at OPMs with a particular focus on SERF magnetometry application in a laboratory-based experiment and a portable sensor. The work will focus on identifying aspects limiting the practical sensitivity of OPMs and addressing these limitations through a design of custom instrumentation. This includes ultra-low-noise current source used to drive magnetic field nulling coils, custom low-noise photodetectors and amplifier architecture, a high stability laser driving system, as well as custom components such as non-magnetic heaters.

1.1 Thesis Structure

This thesis describes two SERF magnetometer experiments, their theoretical background and the instrumentation developed for each. Chapter 2 introduces the atomic physics theory required to understand the experimental work. Chapter 3 describes the experimental setups of a ^{87}Rb, lab-based SERF magnetometer and a portable SERF magnetometer based around ^{133}Cs. The lab-based magnetometer was used as a test bed for instrumentation and techniques later used with the portable SERF magnetometer. This chapter also focused on the characterisation of the performance of the lab-based SERF magnetometer in terms of sensitivity, and steps taken to get to that performance are described. Chapter 4 discusses the development and testing of ultra-low-noise, highly stable, multichannel current sources that are used for driving field nulling coils in magnetometry applications as well as both SERF magnetometers described in Chapter 4. This chapter is based on the author's published work in the Review of Scientific Instruments journal [32]. Chapter 5 details the development process of custom optoelectronics instrumentation including low-noise photodetectors and a laser driver for vertical-cavity surface-emitting laser (VCSEL) diodes. Chapter 6 focuses on the investigation of VCSEL diodes as an alternative laser source to the distributed

Bragg reflector (DBR) laser, currently used in the portable SERF magnetometer.

1.2 Work involvement

The work described here began in parallel with other, PhD laboratory members, Edward Irwin, whose thesis describes the atomic side of the Rb SERF experiment, Rachel Dawson, who focused on the Cs SERF as well as machine learning for optimisation of the experiment. Each made a contribution to the other's work. The work reported here is the author's contribution. The author also made a contribution to the free-induction decay (FID) project involving post-doctoral researcher Dominic Hunter and PhD candidate Allan McWilliam. This work is ongoing and is not reported here.

Publications Arising from This Work

- M. S. Mrozowski, I. C. Chalmers, S. J. Ingleby, P. F. Griffin, and E. Riis, "Ultra-low noise, bi-polar, programmable current sources" Review of Scientific Instruments 94, 014701 (2023), 10.1063/5.0002964

- D. Hunter, M. S. Mrozowski, A. McWilliam, S. J. Ingleby, T. E. Dyer, P. F. Griffin, E. Riis, "Optical pumping enhancement of a free-induction-decay magnetometer" Journal of Optical Society of America B, 40, 2664-2673, (2023)

- R. Dawson, C. O'Dwyer, E. Irwin, M. S. Mrozowski, D. Hunter, S. J. Ingleby, E. Riis, and P. F. Griffin, "Automated Machine Learning Strategies for Multi-Parameter Optimisation of a Caesium-Based Portable Zero-Field Magnetometer" Sensors 23, 4007 (2023), 10.3390/S23084007

- D. Hunter, C. Perrella, A. McWilliam, J. P. McGilligan, M. Mrozowski, S. J. Ingleby, P. F. Griffin, D. Burt, A. N. Luiten, E. Riis, "Free-induction-decay magnetic field imaging with a microfabricated Cs vapor cell" Optics Express, 31, 33582-33595 (2023), 10.1364/OE.500278

- S. J. Ingleby, P. F. Griffin, T. Dyer, M. S. Mrozowski, and E. Riis, "A digital alkali spin maser" Scientific Reports, 12, 1-7 (2022), 10.1038/s41598-022-16910-z

Chapter 2

Theory of SERF OPMs relevant to the experimental work

This section presents the core atomic physics theory and concepts required to describe experimental work focused on optically pumped magnetometers.

2.1 Atomic Energy Structure

Alkali metal atoms find their use in metrological instruments such as magnetometers and atomic clocks due to their simple electronic structure consisting of a single unpaired electron in the outer energy shell that can be manipulated with ease. Additionally, the presence of optical transitions in visible and near infra-red (NIR) makes them easily accessible with laser technology. Because of this, the energy can be well approximated by considering only the valence electron and the nucleus, while neglecting the electrons in the inner energy shells.

Orbital angular momentum of the electron $\vec{L}$ is constrained in the range of $0 \leq L \leq n-1$, where L is the magnitude of the vector $\vec{L}$ and n is the principal quantum number. Alkali metal atoms consist of a single outer valance electron and a single electron spin $S = 1/2$, with spin angular momentum $\vec{S}$ [33].

The sum of the orbital angular momentum of the electron $\vec{L}$ and total spin angular momentum $\vec{S}$, gives rise to the total angular momentum of the electron $\vec{J}$. The quantum number J, which is the magnitude of $\vec{J}$, can range from $|L-S| \leq J \leq |L+S|$ and is restricted to integer values in that range. The spin-orbit coupling ($L-S$ coupling) thus results in the splitting of energies for states where $L > 0$, giving rise to fine structure splitting.

The spectroscopic notation used to specify an occupied quantum state is given in the form $|L, S, J\rangle = {}^{2S+1}L_J$. The energy eigenstates of fine structure splitting are hence described by $|n\ell, {}^{2S+1}L_J\rangle$. For Cs, the ground state $L = 0$ does not result in splitting due to spin-orbit coupling, while the first excited state $L = 1$ is split into two states $6p\,^2P_{1/2}$ and $6p\,^2P_{3/2}$ respectively. The transitions from the ground state $6s\,^2S_{1/2}$ to $6p\,^2P_{1/2}$ and $6p\,^2P_{3/2}$ states is described as the D_1 and D_2 transitions [34]. These transitions are one of the key elements used in the processes of optical pumping and detection in atomic magnetometers with D_1 being the most popular in magnetometry application, demonstrating superior optical pumping efficiency in comparison to D_2 when there is collisional mixing in excited state [35]. D_1 also presents more widely spaced hyperfine levels in the excited state, it also features dark states that allow for optical pumping into unperturbed Zeeman states.

D_2 transition is typically used in dual beam setups, where D_2 is used for pumping while D_1 is used for detection [35].

The interaction between the electron's angular momentum $\vec{J}$ and the nuclear spin $\vec{I}$, (quantum number I) gives rise to total angular momentum $\vec{F}$ that can range in integer values $|I-J| \leq F \leq |I+J|$ which leads to much narrower atomic energy splitting known as the hyperfine splitting.

The hyperfine splitting levels F can further split into magnetic sublevels with quantum numbers m_F, which can be described by $2F+1$ for a corresponding F level. In the absence of a magnetic field, the m_F levels become degenerate. The values of m_F range from $-F, m_F, F$. The energy eigenstates in the hyperfine structure can be described by $|n\ell, {}^{2S+1}L_J, F, m_f\rangle$ [36, 37]. The Cs energy structure

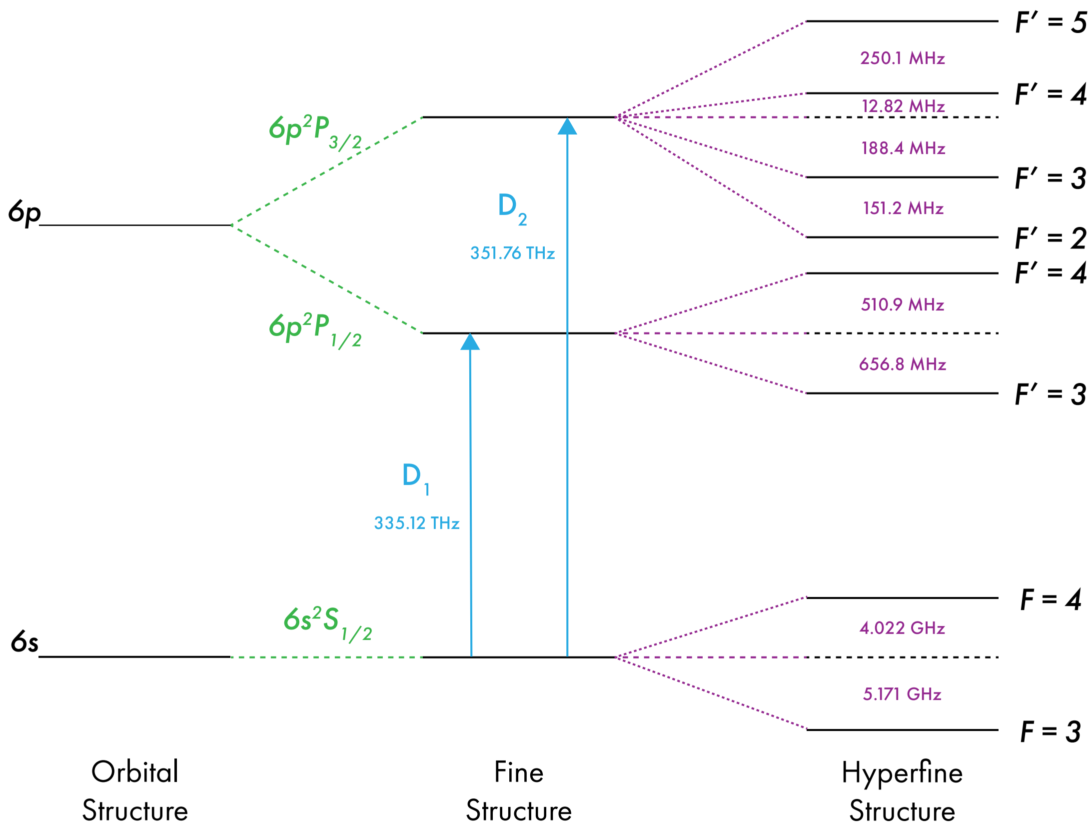

Figure 2.1 – Cs energy structure diagram, illustrating splitting of the ground state and the first excited state. The D_1 and D_2 transitions arise from the fine structure interaction and the hyperfine structure from the coupling of the electron angular momentum with the nuclear spin. This process is denoted by the quantum number F for ground state splitting and F' for excited splitting. Splittings illustrated are not to scale.

diagram, including D_1 and D_2 transitions as well as their corresponding hyperfine splitting, is presented in Fig. 2.1.

2.2 Zeeman effect

Previously mentioned m_F levels are degenerate in the absence of a magnetic field. This degeneracy can be lifted if an external static magnetic field is applied, due to the interaction of magnetic moments of electrons and protons with the external field [36]. This process can be described using the Zeeman effect where the m_F levels act as the projection of the total angular momentum F onto the external magnetic field axis. For magnetic fields B that is sufficiently small (as is the case for SERF magnetometers) the energy shift ΔE can be given as [36]:

$$\Delta E = g_F \mu_B B m F \ , \tag{2.1}$$

where g_F is the hyperfine g-factor described in Eq. 2.2 and μ_B is the Bohr magneton.

$$\begin{aligned} g_F = & g_J \left(\frac{F(F+1) + J(J+1) - I(I+1)}{2F(F+1)} \right) - \dots \\ & g_I \left(\frac{F(F+1) - J(J+1) + I(I+1)}{2F(F+1)} \right) \ . \end{aligned} \tag{2.2}$$

For higher fields, where the magnitude of the energy shifts becomes comparable to other effects the Zeeman effect has to be redefined. An analytical solution exists for states with ($J = 1/2$), which is relevant for the ground state of alkali metals and can be calculated using the Breit-Rabi equation for the ground state levels when $L = 0$ [36]. As the magnitude of the fields used in this thesis is close to zero fields (< 1 μT), only the low magnetic field energy shift Eq. 2.1 is considered, which is valid for fields < 30 μT for Cs [38].

If the external magnetic field B defines the quantisation axis, then under this condition m_F is a good quantum number. This leads to the evolution of the m_F state, where the hyperfine states precess with the frequency ω_F given in Eq. 2.3.

$$\begin{aligned} \omega_{F=I\pm1/2} &= \pm \frac{g_j \mu_B B}{(2I+1)\hbar} \\ &= \pm \gamma B \ . \end{aligned} \tag{2.3}$$

The ω_F is known as the Larmor precession frequency [39], governed by the gyromagnetic ratio γ and the external magnetic field B. It is important to note that for the ground state of alkali atoms where $F = I - J$ for the lower ground state and $F = I + J$ for the upper ground state will result in opposite sign g-factors, that result in opposite Larmor precession direction [37]. This fact is important and is covered in the later section 2.6.1 as it is a primary source of relaxation due to spin-exchange collision.

2.3 Absorption Spectral Line

The observed absorption spectra depends on the alkali species, giving rise to its natural linewidth as well as any additional broadening mechanisms present in the system. These broadening mechanisms can be split into homogenous and inhomogeneous broadening mechanisms. Homogeneous broadening mechanisms affect all the atoms present in a sample (such as a vapour cell) in the same way. One such mechanism is pressure broadening, which depends on the operating temperature of the sample or the buffer gas type and pressure. Inhomogeneous broadening mechanisms affect individual atoms in different ways, such as with the Doppler broadening in thermal atoms.

2.3.1 Natural Linewidth

The natural resonance linewidth is based on the natural lifetime of the atomic transition $\tau = 1/(2\pi\Gamma_0)$ [35], where Γ_0 is the resonance linewidth given as full-width-at-half-maximum (FWHM) [40]. The natural linewidth stems from the time-energy uncertainty relation, which prevents atomic transitions from having singular frequencies. The lifetime depends on species and for the D_1 transitions of ^{133}Cs and ^{87}Rb is 34.791 ns [41–43] and 27.679 ns [44–46] respectively. The natural linewidth is a homogeneous broadening mechanism and thus has a Lorentzian distribution, $\mathcal{L}$. Its normalised distribution is presented in Eq. 2.5

$$\Gamma_0 = \frac{1}{2\pi\tau} \tag{2.4}$$

$$\mathcal{L}(\nu) = \frac{1}{\pi}\frac{\Gamma_0/2}{(\nu-\nu_0)^2+(\Gamma_0/2)^2} \ . \tag{2.5}$$

2.3.2 Broadening mechanisms

Among other homogeneous broadening mechanisms that are recognised is the broadening due to atom collisions known as pressure broadening Γ_{P}. Alkali-alkali collision that increases with density and alkali-buffer gas collisions in the presence of buffer gas decreases the lifetime of the transition and in turn, increases the broadening effect. Similar to natural linewidth, the pressure broadening follows the Lorentzian distribution found in Eq. 2.4. As both the natural linewidth Γ_0 and pressure broadening Γ_{P} follow Lorentzian distribution, their effects can be combined to produce total homogenous broadening $\Gamma_{\mathrm{T}} = \Gamma_0 + \Gamma_{\mathrm{P}}$.

The other broadening mechanism that needs to be considered is inhomogeneous broadening. Atoms have a thermal velocity and their root-mean-square (RMS) value can be described as $v = \sqrt{3k_BT/m}$, where k_B is the Boltzmann constant, T is the temperature, and m is the mass of the atom. Considering that atoms will have a component of their velocity along the direction of the laser light, each will experience a shift in the light frequency due to the Doppler effect. This effect will present a spread of frequencies interacting with the atoms which broaden the linewidth. This process is dependent on the temperature of the sample and is governed by the Gaussian distribution with a FWHM presented in Eq. 2.6 where c is the speed of light in vacuum.

$$\Gamma_{\mathrm{D}} = \frac{\nu_0}{c}\sqrt{\frac{2k_BTln2}{m}} \ . \tag{2.6}$$

A way to describe the combined broadening mechanism is to use a Voigt distribution [47] which is the convolution of Lorentzian and Gaussian distributions. Typically in cells that operate at elevated room temperatures, Doppler broadening (Γ_{D}) dominates [36]; however, when sufficient buffer gas pressure is present, the pressure broadening (Γ_{P}) can dominate and has a bigger impact with the spectral linewidth taking a $\mathcal{L}$ Lorentzian distribution.

2.3.3 Absorption cross-section

The probability of a photon being absorbed by the atom is known as the absorption cross-section. For a typical Lorentzian line shape caused by a homogeneously broadened transition of $\Gamma_{\mathrm{T}} \approx \Gamma_{\mathrm{P}}$ and natural linewidth Γ_0 the absorption cross-section is given as Eq. 2.7 [48]

$$\sigma_{\mathrm{abs}} = \frac{\lambda^2}{2\pi} \frac{2J'+1}{2J+1} \frac{\Gamma_0}{\Gamma_{\mathrm{T}}} , \tag{2.7}$$

where λ is the wavelength of the transition, J is the total electronic momentum of the ground state while J' is the total electronic momentum of the excited state. As the linewidth Γ_{T} broadens, the absorption cross-section σ_{abs} will also broaden, such that peak absorption is lowered and as a consequence, the light absorption will decrease. To retain an adequate level of absorption, a higher number density of the medium is required. This is achieved by heating the atoms in the cell.

2.4 Optical pumping

Optical pumping can be described as using the degrees of freedom of light to create non-equilibrium states of matter; when a photon is absorbed it transfers its angular momentum, which is dependent on the light polarisation on the atom. In this section, we consider the role of this transfer, plus spontaneous emission, on population redistribution within a single hyperfine state.

The selection rules define the excitation of the m_F magnetic sublevels. Driving a π transition, where the k vector is perpendicular to the B field and the light polarisation is parallel to B, the excited state transition is given as $\Delta m_F = 0$. For

σ^+ transition the excitation is given as $\Delta m_F = m_F + 1$ and for the σ^- transition, it is given as $\Delta m_F = m_F - 1$. The atom does not remain in the excited state forever and quickly decays to the ground state. The decay process follows the same selection rules, where the probability of decaying to a particular ground state is governed by the Clebsch-Gordan coefficients [36].

In this thesis, the $F = 4 \rightarrow F' = 3$ of the the D_1 line of ^{133}Cs and $F = 2 \rightarrow F' = 1$ of the D_1 line of ^{87}Rb are mainly used for the optical pumping. When the circularly polarised light driving σ^+ transition is used, atoms will experience the repeated cycles of absorption and decay, moving the atomic population to increasingly large Δm_F levels. This process eventually stops when the atoms reach the dark state, either $m_F = 3$ or $m_F = 4$, where no further absorption happens due to selection rules.

By continuing this process most of the atomic population will be located in the dark state and a net magnetisation $\mathcal{M}$ is formed which is called the orientation moment with a preferred direction. The direction of the orientation can be changed by pumping the population with a circularly polarised light driving σ^- transition which will encounter a dark state in the $m_F = -4$ or $m_F = -3$ state in this particular case assuming no decay to $F = 3$ occurs.

If however, linearly polarised light driving π transition would be used, the population would be split, occupying mostly both dark states, $m_F = \pm 4$ and forming an alignment moment that does not feature preferred direction and is only concerned with the axis [49]. The population and redistribution for orientation and alignment moment are presented in Fig. 2.2.

Despite optical pumping into either alignment or orientation, some leftover atoms will decay and occupy the $F = 3$ state, potentially leading to spin exchange collision with atoms in $F = 4$ and scrambling of the polarisation of the spins. The $F = 3$ population can be evacuated with another laser source through a process called re-pumping; however, this work is concerned with a single beam and as such repumping mechanism is not considered here. At the same time, the SERF magnetometer configuration aims to suppress the effects of the spin exchange mechanism covered in Section 2.6.3.

Magnetometers described in this thesis use the orientation moment to build a population in the dark state and a $B = 0$ crossing is detected with the use of a ground state Hanle effect (GSHE), where the transmission signal is proportional to the polarisation [50].

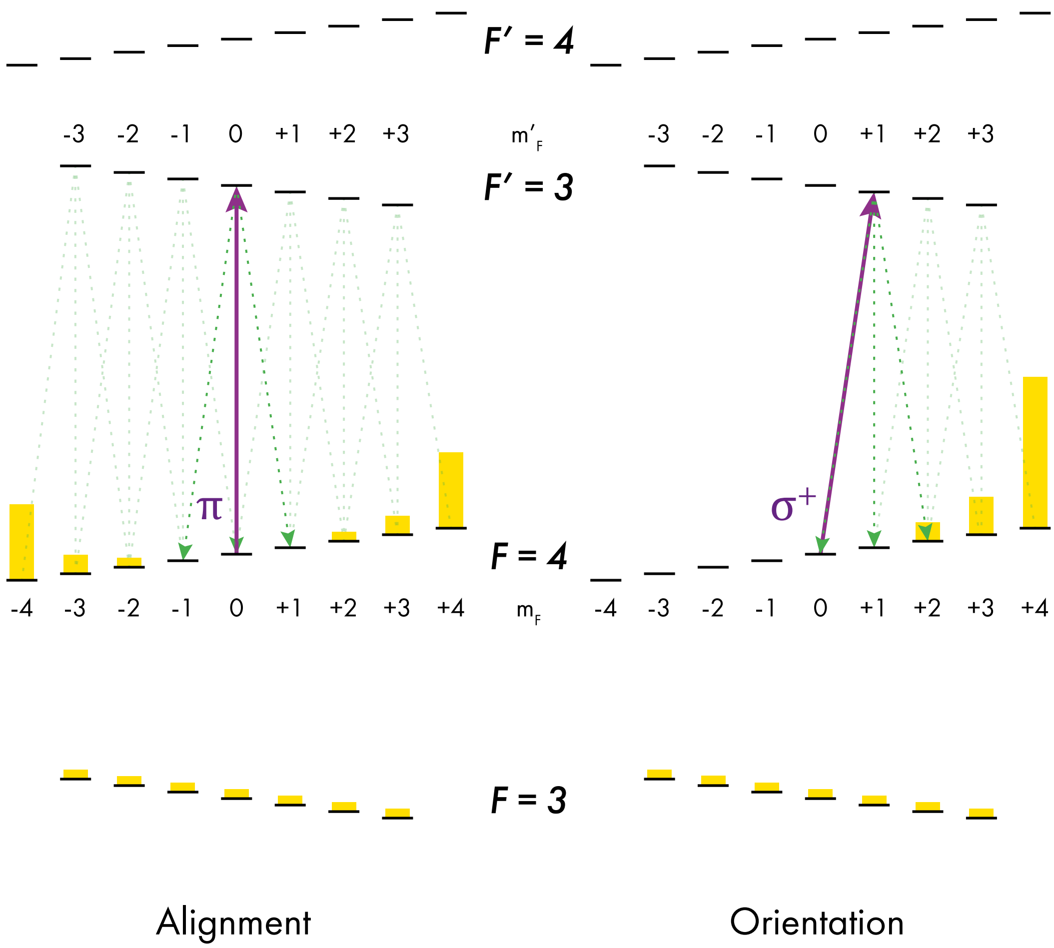

FIGURE 2.2 – Level diagram of ^{133}Cs D_1 line of the hyperfine states with their corresponding resolved excited hyperfine states. The atomic population is shown pumped into alignment and orientation states with the use of linearly polarised light driving π transition, and right-circularly polarised light driving σ^+ transition resonant to $F = 4 \rightarrow F' = 3$ respectively. The relative population of atoms occupying given states is shown with the height of yellow bars.

2.5 Ground State Hanle Effect

In the 1920s Wilhelm Hanle observed that the degree of polarisation of fluorescent light radiation in a dilute atomic medium is dependent on the magnetic field applied in the particular direction [51]. The effect manifests itself as resonance structure centred at $B = 0$ and is known as the depolarisation of resonance fluorescence, zero-field crossing or Hanle Effect [52]. The same effect also occurs in the ground state of the optically pumped atoms, where an external magnetic field transverse to the pump direction can be detected by scanning it through a zero field as a function of absorption [9, 50].

In the magnetometers described in this thesis, the alkali atoms are polarised with circularly polarised light and eventually reach the dark state where no further optical pumping occurs. Assuming that the magnetic field had been nulled in all axis, maximum transmission through the cell will be achieved as atoms no longer absorb light[50, 53].

In the experiment, the z-axis is used for pumping and monitoring transmission through the cell. If the field appears along the x-axis, atoms will experience torque and be able to evolve in time, causing precession out of the dark state enabling absorption manifesting as a peak when crossing through $B_x = 0$. If the field along the pumping axis is $B_z = 0$ and B_x and B_y are not nulled the atoms will precess out of the dark state and start to absorb the light manifesting as a dip in transmission [50, 53]. The width of the magnetic resonance δB is dependent on the T_2 relaxation time described in Section 2.6 where δB is given by [13]

$$\delta B = (2\pi q T_2 \mu_0)^{-1} . \tag{2.8}$$

Here, T_2 is the transverse relaxation time, μ_0 is the permeability of free space and q is the nuclear slowing-down factor which will be described in the later section 2.6.3.

From Eq. 2.8 it can be determined that T_2 time plays an important role in the overall sensitivity of the device to magnetic fields.

2.6 Spin Relaxation

For magnetometers in which the total magnetic field B is present perpendicular to z, the electronic spins of the alkali atom will precess about the field. By extending the coherence time of this precession, higher magnetometer sensitivity can be obtained. For this to happen the spins need to remain polarised for as long as it is possible. This spin coherence time is known as the transverse relaxation time, T_2. The longitudinal relaxation time is known as T_1 which defines the lifetime of the longitudinal spin polarisation. It is typically much longer than the T_2 [54], as such the T_2 is the sensitivity limiting factor.

There are multiple processes that cause depolarisation and negatively impact the T_2 time. One such process is the collision of atoms with glass cell walls. When an atom collides with a glass wall it adsorbs into the surface for some finite time before being ejected back into the cell atomic volume. During the adsorption time, the atom experiences local magnetic and electric fields of the glass, which randomise the spin direction, depolarising the atom in the process [35, 55]. The impact of this effect can be lessened by coating cell walls with inert materials which prevent atoms from reaching the glass walls or by adding buffer gas into the cell. One of the most commonly used materials is paraffin. However, paraffin melts at around 60 - 80 °C and is thus unsuitable for SERF which operates at temperatures higher than the paraffin melting point. Higher temperature synthetic coatings exist but were not considered for this experiment as they are typically only applicable to glass-blown cells [35, 56] while microelectromechanical systems (MEMS) cell fabrication with such coatings requires special consideration [57].

Buffer gas causes atoms to experience the diffusive motion that extends the time for the alkali atom to reach cell walls. The buffer gas has to be chemically inert, and for this reason, noble or inert gasses are typically used. It is common for nitrogen to be used, which has the added benefit of acting as a quenching gas which suppresses the spontaneous emission of a photon and prevents radiation trapping [58, 59] which could otherwise limit the atomic polarisation [35]. Magnetometers often use noble gasses with an addition of nitrogen for quenching [60, 61]. The cells used in the experiments covered in this thesis all use nitrogen as both the buffer gas and quenching gas only, due to manufacturing complexity. The presence of buffer gas can, however, lead to spin-destruction collisions between alkali atoms and gas atoms/molecules leading to additional relaxation. For this reason, buffer gas pressure needs to be balanced for optimal diffusion and spin-destruction collisions.

2.6.1 Spin-Exchange Collisions

Another source of spin relaxation is spin-exchange collisions. Alkali atoms can collide with one another which causes a transfer of their polarisation between electronic and nuclear spins [62]. These collisions conserve the total angular momentum but can redistribute the angular momentum among the hyperfine sub-levels of the ground state. For alkali atoms, spin-exchange cross-sections are considered large with a typical order of 10^{-14} cm^2. Spin-exchange collisions thus contribute to the T_2 relaxation time as each collision can alter the F quantum number, leading to a change in the direction of precession [13, 62]. This phenomenon is presented in Fig. 2.3. The collision rate is proportional to the atomic density and is typically the main relaxation contribution, especially at higher temperatures. The rate of spin-exchange collisions can be given as R_{SE} and is presented in Eq. 2.9

$$R_{\mathrm{SE}} = \eta q_{\mathrm{SE}} \sigma_{\mathrm{SE}} \bar{v} \ , \tag{2.9}$$

where η is the alkali metal vapour density, σ_{SE} is the spin-exchange cross-section, q_{SE} is the spin-exchange broadening factor [35] and $\bar{v}$ is the average thermal velocity of the alkali atoms in the vapour cell given as $\sqrt{8k_bT/\pi m}$.

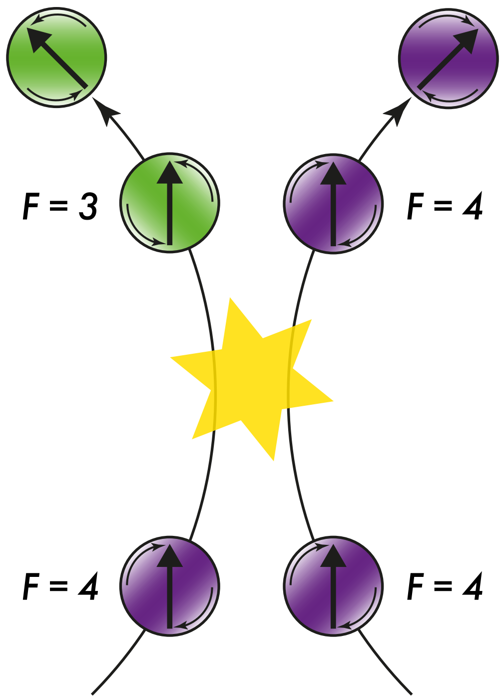

FIGURE 2.3 – Diagram presenting spin-exchange collision between two Cs-metal atoms precessing in the presence of the magnetic field. As the atoms collide with each other they have a chance to change their hyperfine state and begin to precess in opposite directions losing their coherence. Atoms in $F = 3$ state are shown in green and $F = 4$ in purple.

2.6.2 Spin-Destruction Collisions

Spin-destruction collisions differ from spin-exchange collisions in that they do not preserve the total spin polarisation of the atom ensemble. These collisions transfer spin-angular momentum to the rotational angular momentum of the affected atoms [35], randomising the spin direction and decohere the precession. Spin-destruction collision can occur between alkali-alkali, alkali-buffer gas or alkali-quenching gas collisions. The spin-destruction rate is described in Eq. 2.10,

$$R_{\mathrm{SD}} = \eta q \sigma_{\mathrm{SD}} \bar{v} \ , \tag{2.10}$$

where q is the nuclear slowing down factor and σ_{SD} is the spin-destruction cross-section. The nuclear slowing down factor describes the degree to which spin coherence is maintained [13, 35]. Spin-destruction cross-section σ_{SD} is typically two orders of magnitude smaller than the spin-exchange cross-section σ_{SE}, which makes these collisions less frequent and of lower impact on relaxation than spin-exchange collisions in a typical magnetometer.

2.6.3 SERF Regime

As mentioned previously, spin-exchange is the dominant transverse relaxation mechanism in most magnetometers as described in Section 2.6.1. Alkali atom collisions of this type lead to precession in opposing directions, leading to loss of coherence.

However, at low enough magnetic fields, where $R_{\mathrm{SE}} \gg \gamma B$, and sufficiently high atomic density, the spin-exchange collisions occur much faster than the precession rate. The precession of single atoms evolves only by a minimal angle between each collision. Because this process occurs faster than the Larmor precession, the atom will experience the ensembled averaged evolution of all Zeeman sublevels of the ground manifold. However, the atom will spend more time in the upper hyperfine level due to it containing more Zeeman sublevels in comparison to the lower hyperfine level. This is especially true for polarised ensembles, with most of the population occupying a stretched state of the upper hyperfine level. The two hyperfine levels precess at the same frequency but, due to the imbalance in population occupancy, the upper hyperfine state will statistically dictate the precession direction [35].

In this process, the hyperfine states involved can be thought of as being "locked together" and precess at the same, modified rate due to the slowing down factor q [63]. This rate is given in Eq. 2.11 [13]

$$\omega_0 = \frac{g_j \mu_B B}{q\hbar} \ , \tag{2.11}$$

where $q = S(S+1) + I(I+1)/(S(S+1))$. Due to this averaging phenomenon, the spin-exchange relaxation mechanism vanishes [64], drastically increasing the coherence polarisation lifetime. This regime is known as the spin-exchange relaxation-free (SERF) [13, 14] regime, illustrated in Fig. 2.4.

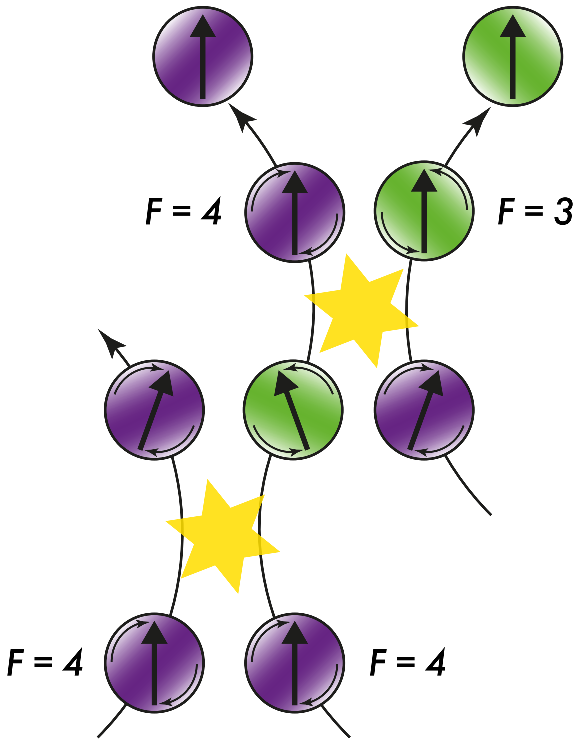

FIGURE 2.4 – Diagram presenting spin-exchange relaxation free regime collisions between Cs-metal atoms precessing in the presence of the magnetic field. The atoms perform two spin-exchange collisions in rapid succession. The collision causes the atoms to change their hyperfine state but as the collision rate is faster than the precession frequency it allows for the atoms to regain their original hyperfine state on the second collision. Atoms in the $F = 3$ state are shown in green and $F = 4$ in purple.

To achieve the SERF regime, sufficiently high atomic density [63] is required to enable frequent collision, fulfilling $R_{\mathrm{SE}} \gg \gamma B$. Vapour pressure is highly dependent on temperature due to their low melting points [65]. For alkali metals used in this thesis, sufficient densities to reach SERF have been achieved at 135 °C and 150 °C for Cs and Rb respectively where a density of $\approx 10^{14}$ cm^3 is achieved. With the elimination of spin-exchange relaxation, the main source of polarisation relaxation becomes spin-destruction collisions [62].

Chapter 3

SERF Experiments

This thesis focuses on two, single beam SERF experiments tackling different requirements. The first one is a lab-based experiment that uses ^{87}Rb as its alkali specie and aims to achieve high sensitivity (< 100 fT/$\sqrt{\text{Hz}}$) which could be used to explore low-field physical phenomena such as the detection of NMR [17]. The second one is the portable, ^{133}Cs base SERF magnetometer to be used for biomedical applications. The lab-based experiment is also used as a test bed for techniques and optimisation later implemented in the magnetometer covered later in Section 3.5. This magnetometer is a portable design using ^{133}Cs as its alkali specie.

The initial Rb SERF magnetometer experimental work was a collaborative effort with other PhD candidates: Edward Irwin and Rachel Dawson as well as postdoctoral researcher, Carolyn O'Dwyer.

The work presented here, on the updated lab-based magnetometer setup, was based on collaborative work with a postdoctoral researcher, Dominic Hunter.

In this chapter, the experimental setups of both a lab-based Rb magnetometer and a portable Cs magnetometer will be explored. The primary focus of this chapter is the evaluation of the instrumentation around these magnetometers, that enable their performance. The instrumentation includes ultra-low noise current source used as a coil driver for driving the nulling field Helmholtz coils covered in Chapter 4, as well as low noise amplified photodetector covered in Section 5.1 of Chapter 5.

3.1 Lab-based SERF Experimental setup

The magnetometer was designed in a single-beam configuration. Single-beam configurations provide an advantage in their simplicity, streamlining the process of scaling down the lab-based experiment into a portable one due to the reduced number of optical elements and a need for a single light source. Single-beam configuration however suffers from reduced pumping efficiency [35] and achieves lower sensitivity than the two-beam, pump and probe setups.

Magnetometer sensitivity is directly correlated with polarisation lifetime T_2, as mentioned in Section 2.6. T_2 time is negatively affected by the rate of spin-exchange collisions, R_{SE} and the rate of spin-destruction collisions, R_{SD}. In the SERF regime, spin-exchange collisions are eliminated and only spin-destruction collisions remain. In the selection of an alkali specie for a magnetometer, cross-sections of both spin-exchange and spin-destruction need to be considered. Both cross-sections define the rate at which collision can occur. For sensitivity only the spin-destruction cross-section, σ_{SD} is important. Alkali metals with smaller cross-section experience smaller spin-destruction rates and higher sensitivity. At the same time spin-exchange cross-section σ_{SE} should be as large as possible to enable SERF operation at a lower temperature which is directly correlated with the density of the alkali metal. Unfortunately, alkali metals with higher density and σ_{SE} feature higher σ_{SD}. σ_{SE} and σ_{SD} for different alkali metals is presented in Tab. 3.1.

Table 3.1 – Cross-section values for spin-exchange σ_{SE}, spin-destruction between alkali atoms $\sigma_{\mathrm{SD}}^{\mathrm{self}}$ and spin-destruction between alkali atoms and nitrogen buffer gas $\sigma_{\mathrm{SD}}^{\mathrm{N_2}}$. Data obtained from [66–70]

Alkali metal	σ_{SE}	$\sigma_{\mathrm{SD}}^{\mathrm{self}}$	$\sigma_{\mathrm{SD}}^{\mathrm{N_2}}$
Cs	1.9×10^{-14} cm^2	2×10^{-16} cm^2	60×10^{-23} cm^2
Rb	1.65×10^{-14} cm^2	9×10^{-18} cm^2	10×10^{-23} cm^2
K	1.45×10^{-14} cm^2	1×10^{-18} cm^2	7.9×10^{-23} cm^2

Initially, the lab-based SERF experiment used a ^{133}Cs as its alkali species, which was housed in a micro-fabricated vapour cell as an investigation into low-power, and low-temperature SERF magnetometer. Low power consumption and lower temperature are of particular interest for medical applications in which magnetometers are typically used in arrays and require to be skin safe (≤ 43 °C) [31, 71, 72]. It was however decided to move to ^{87}Rb, in pursuit of maximising sensitivity in single-beam setups, while ^{133}Cs was explored in a portable SERF setup covered later in Section 3.5. The Rb SERF magnetometer setup is presented in Fig. 3.1.

3.1.1 Vapour cell

The experiment is based around a 10 mm^3 internal dimension (1 mm thick walls), glass blown cell manufactured by TwinLeaf LLC, containing enriched ^{87}Rb filled with 200 Torr of N_2 buffer gas. A photograph of the cell used is presented in Fig. 3.2.

The vapour cell is housed in an oven made out of two FR4 printed circuit boards (PCBs) that carry two custom field-cancelling heaters. The boards are retained with two nylon bolts with the heaters bonded to the cell with a non-magnetic Boron-nitrate thermal compound improving thermal conductivity. A flat, T-type, non-magnetic thermocouple is attached near the cell stem using reinforced polyimide tape enabling temperature measurements of the cell. The

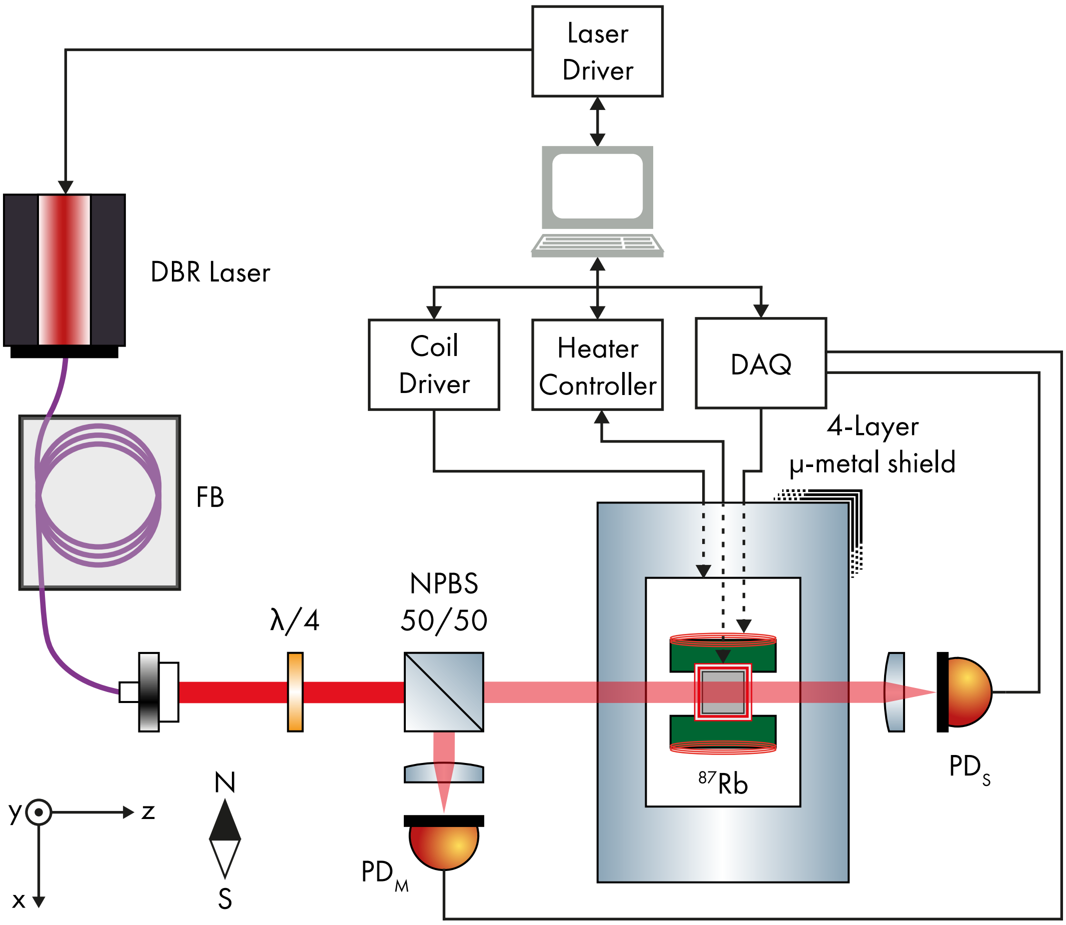

Figure 3.1 – Diagram presenting experimental setup of the Rb SERF magnetometer. DBR Laser: distributed Bragg reflector laser; FB: fiber box; $\lambda/4$ quarter-wave plate; NPBS: non-polarising beam splitter; ^{87}Rb: enriched rubidium 87 vapour cell; $\mathrm{PD_M}$: monitor photodetector; $\mathrm{PD_S}$: signal photodetector; DAQ: data acquisition system. The figure also shows a 4-layer magnetic shield.

assembly is insulated with SuperWool® HT felt mat and wrapped with polyimide tape, to increase heating efficiency. The oven assembly is then inserted into a coil former that houses the B_{RF} coil to supplement the field cancellation coils present in the mu-metal shield assembly. The coil former is a 3D printed part, made out of high-temperature resin [73] to withstand the cell temperature. The former is secured to the integrated nylon breadboard of the shield.

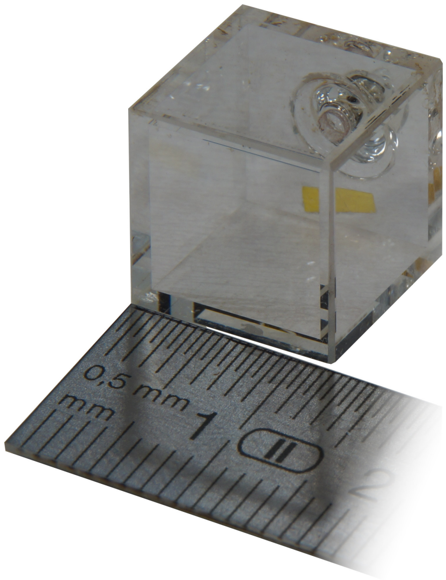

Figure 3.2 – Photograph of the enriched ^{87}Rb 10 mm^3 internal dimension glass blown vapour cell used in this experiment.

3.1.2 Magnetic shield

The whole assembly is housed in a four-layer mu-metal shield (MS-1L) from TwinLeaf. Its purpose is to effectively attenuate static and oscillating fields that would otherwise saturate the sensor. Static fields such as the Earth's field lines are re-directed around the shielded surface, due to the very high permeability of the shield providing an effective path for the field lines to follow. mu-metal can also be used for attenuation of oscillating fields such as alternating current (AC) mains. Low-frequency AC fields are better attenuated due to the wave-impedance increase at the barrier, however, their effectiveness drops as the frequency increases due to a reduction in permeability [74].

The shield also features built-in field-nulling coils as well as a set of gradient coils. Field nulling coils are used to cancel the remaining magnetic field in the shield providing field nulling in B_x, B_y which is in the order of few nT, as well as applying static fields to test the magnetometer. The static field coils are driven with a custom ultra-low noise multi-channel current source, which is covered in

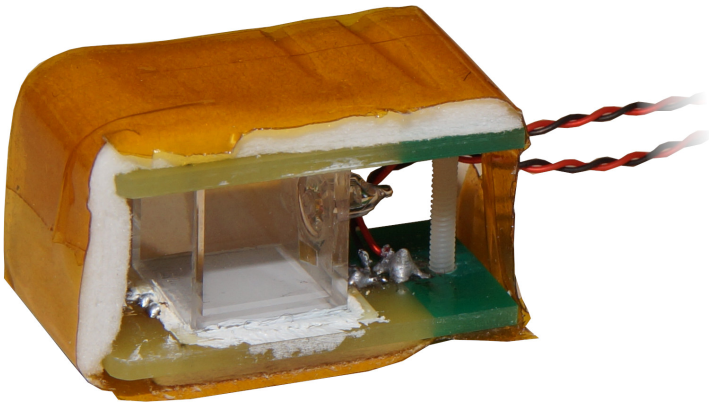

Figure 3.3 – Photograph of the partially assembled oven housing Rb cell and field cancelling heaters. After the T-type thermocouple is attached to the cell with reinforced polyimide tape, the rest of the assembly is covered in insulating material leaving only optical access windows of the size of the cell wall.

detail in Chapter 4. The coils feature a field to current ratio of 67.305, 67.875 and 122.336 μT/A for B_z, B_y and B_x coils respectively. Gradient coils can be used to correct for any magnetic field gradients experienced in the cell. These gradients contribute to relaxation due to atoms experiencing different magnetic fields affecting their precession [75, 76]. Gradient coils have not been used in this experiment due to the size of the cell and the overall uniformity of the generated B field through the static field coils.

The shield's long side (along the x-axis) has been orientated in the direction along magnetic North to better shield against the earth's magnetic field as seen in Fig. 3.1.

3.1.3 Optical Setup

A coherent laser light source is provided by a single frequency, DBR laser tuned to the $F = 2 \rightarrow F' = 1$ of the D_1 line of ^{87}Rb. The DBR laser used is a fibre-coupled, 40 mW maximum output power, 795 nm, single frequency laser in a butterfly package [77]. The butterfly package integrates an optical isolator, thermo-electric cooler (TEC), thermistor and a monitor photodiode. These lasers were found to have their polarisation not fully aligned with the slow axis of the fiber. The consequence of this is that any perturbation to the fiber will cause a change in polarisation [78]. For this reason, a small box was 3D printed that houses the fiber, insulated with SuperWool® material used for insulating the cell assembly. To minimise environmental effects on the fiber only short sections of the fiber are exposed to the environment.

The laser light beam with a 3.6 mm diameter first travels through a quarter-wave plate which is used to turn the linearly polarised light into circularly polarised light. This light is split with a non-polarising beam splitter and sent to a custom low-noise photodetector $\mathrm{PD_M}$ which serves as a monitor photodiode while the other portion of the beam is incident with the cell inside the shield. The circularly polarised light optically pumps the ^{87}Rb atoms to a dark state in the absence of a magnetic field. Deviation from zero magnetic fields allows for the atoms to exit the dark state and change the transmission of light through the cell as described in Section 2.5. The change in intensity is detected with the signal photodetector $\mathrm{PD_S}$, which is configured in an identical configuration to $\mathrm{PD_M}$. The use of $\mathrm{PD_M}$ and $\mathrm{PD_S}$ allows for the cancellation of common mode noise, which in this case is the intensity noise of the laser. The photodetectors have lenses mounted in front of them in order to fit the beam size that is incident on the active area of the photodetector.

All of the optics are mounted on small raising breadboards screwed to the optics table with 1.5″ thick posts, raising the optics to the shield optical access holes in order to minimise vibration susceptibility. All of the optics are then attached to the shield using a cage-mount system, in an attempt of making any vibration common mode with the rest of the setup. A photograph of the setup is presented in Fig. 3.4.

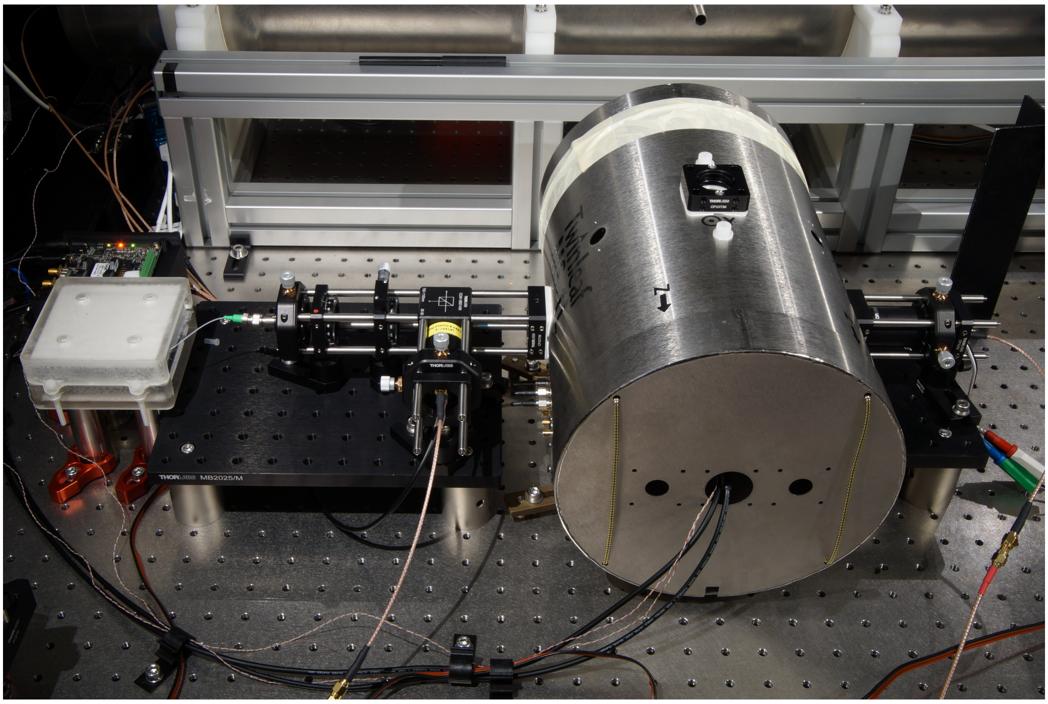

Figure 3.4 – Photograph of the Rb SERF setup. The optical setup is housed on two breadboards raised with 1.5″ posts and mounted in a cage mount system to limit the impact of vibration coupling into the setup.

3.1.4 Electronic Setup

The laser detuning and optical power are controlled with a CLT200, digital butterfly laser diode controller made by Koheron. This driver features a very low current noise of ≈ 1.5 nA/$\sqrt{\text{Hz}}$ at 10 Hz and an RMS noise of 130 nA in a bandwidth of 10 Hz to 1 MHz. Low current noise is important for any magnetometer as it directly affects intensity noise as well as the frequency noise of the laser. The frequency noise of the laser comes from changes in carrier density in the gain section caused by injection current [79].

For a DBR laser used in this application, this value is relatively small at 0.0014 nm/mA or ≈ 664 MHz/mA. For a 200 torr N_2 broadened cell the D_1 transitions broaden to ≈ 5.4 GHz. Converting the RMS current noise into frequency yields ≈ 86.3 kHz which is negligible and allows to resolve the pressure broadened D_1 transition.

The detuning of the laser can also be tuned by controlling its package temperature, which in turn affects the physical cavity length of the laser and the refractive index [80]. The DBR laser used here features a tuning of 0.06 nm/K or $\approx$ 28.5 GHz/K. The CTL200 laser controller features a TEC controller capable of controlling the package temperature of the DBR laser down to 1 mK which yields 28.5 MHz, well below the pressure broadened D_1 transition.

The photodetector signals are sampled and digitised by a NI PCIe-6353, which is the 16-bit data acquisition system (DAQ). The signals are sampled at the same time and later subtracted in software to remove common mode noise, such as intensity noise. The DAQ also drives the B_{RF} coils with AC to modulate the magnetometer signal.

The heaters used in the experiment are custom-made, with a nominal resistance of 12 Ω. These heaters are manufactured on double-sided PCB made out of high glass transition substrate (TG-180) to withstand the temperature of the cell. The substrate has a thickness of 200 μm that feature bifilar counter winding made out of copper tracks on both sides for better magnetic field cancellation. The heating area is 11 mm^2 which presents a good overlap with the cell that has a side of 12 mm. A photograph of the heater resistor is presented in Fig. 3.5.

The non-magnetic heaters are driven with a custom heater driver, that is based around an H-bridge configuration where the load is not referenced to the ground but rather floats between bridge arms. This configuration is known as the bridge-tied load (BTL), which increases the voltage output by two times and power by four according to $P = V^2R$ in comparison to a single-ended configuration [81]. The driver achieves its high efficiency through the use of an H-bridge configuration which outputs a square wave signal at frequencies much higher than the bandwidth of the magnetometer. In this experiment, the heater operates at a frequency of 137.231 kHz. This odd frequency was selected to avoid coupling to any other common frequencies used in the lab. The heater output power is controlled by

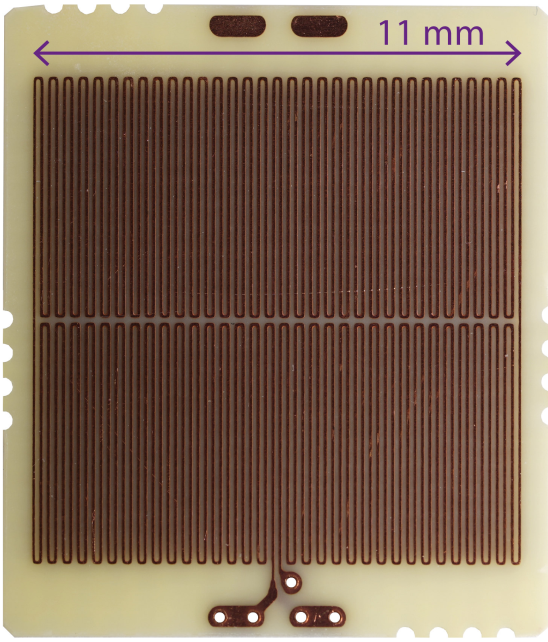

Figure 3.5 – Photograph of the field cancelling heater with scale provided for the active area side. The heater features bifilar counter winding on both sides to reduce magnetic field generation.

delaying the phase of one side of the H-bridge that will present an overlap with the other side and cancel its effect. This method allows for effective control of the duty cycle of the signal. The heater circuit features a thermocouple monitor for monitoring the temperature of the cell. The temperature monitor is based around an MCP9600 (Microchip) thermocouple amplifier and digitiser that allows for measurements of the cell down to ≈ 0.07 °C.

The laser, coil and heater drivers and the DAQ, are all controlled with a PC using custom LabVIEW software. This enables the automated operation of the magnetometer for optimisation and testing.

3.2 Magnetometer Figures of merit

The GSHE described earlier in Section 2.5, manifests as a change in the transmission of light through the atomic vapour as a function of crossing through zero magnetic field. The observed transmission displays a Lorentzian distribution on the axes transverse to the direction of the laser beam. In order to estimate the sensitivity of the magnetometer a conversion from photodetector voltage into magnetic sensitivity needs to take place.

After the field is nulled on each axis, the magnetic field modulation is applied along the component transverse to the beam direction. The previously described Lorentzian lineshape is modulated, and a dispersive signal is obtained from the demodulated signal. The gradient of the slope of the dispersive signal can be then extracted, and a conversion of voltage on the photodetector to magnetic sensitivity (V/T) is obtained. Lorentzian resonant structure and its resulting dispersive signal are presented in Fig. 3.6.

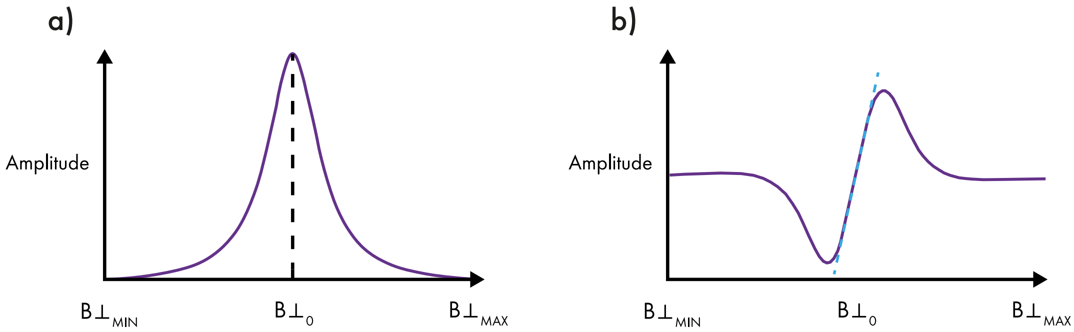

FIGURE 3.6 – Drawing of a zero B-field crossing resonance lineshape (a) and its resulting dispersive signal (b). The gradient of the dispersive signal (blue dashed line) provides a conversion from the voltage (V) read on the photodetector to magnetic sensitivity (V/T).

To estimate the noise floor of the magnetometer, the modulating magnetic field is continuously applied (with the other axis nulled). The signal from the photodetector is monitored and an noise spectral density (NSD) can be obtained.

The Lorentzian lineshape width and height contain information about the sensitivity as well as the bandwidth of the magnetometer and its dynamic range. In general, the optimisation is based on the "sharpness" of the gradient of the dispersive signal as well as the noise floor of the setup. The measured slope can be approximated by taking the ratio of the height and width of the Lorentzian lineshape. A detailed operational procedure of the magnetometers described in this thesis, as well as the optimisation procedure, are described in the theses of Rachel Dawson and Edward Irwin. Further detail is also provided in a yet unpublished article and recently published work [82].

3.3 Magnetometer Performance estimation

The lab-based magnetometer described in this chapter is affected by different, external noise sources present in the experiment. In an ideal scenario, the magnetometer sensitivity should be photon shot noise limited, however, in practice, it is difficult to remove all other noise sources from affecting the magnetometer sensitivity. For a 5 mW beam with a diameter of 3.6 mm (that is used in our experiment) focused on the photodetector with a responsivity of 0.6 A/W yields a photocurrent I_p of 3 mA. Under these conditions, the photon shot noise contribution is 31 pA/$\sqrt{\mathrm{Hz}}$, which for a detector with transimpedance gain of 2 kV/A (configuration used in the experiment) gives a total output voltage spot noise of 62.4 nV/$\sqrt{\mathrm{Hz}}$ when used with our detector. The estimated output voltage noise already includes all other noise sources later discussed in Section 5.2.3. At optimal parameters in our experiment (laser power, laser frequency detuning, modulation and demodulation parameters) the demodulated signal gives a slope of 14.3 mV/nT.

If the magnetometer would only be limited by the photon shot noise, it would achieve a sensitivity of 4.4 fT/$\sqrt{\mathrm{Hz}}$.

The second source of magnetic noise that typically limits the sensitivity of the magnetometer is the thermal noise originating from the mu-metal shield. For frequencies up to 1 kHz the typical magnetic noise is 16 fT/$\sqrt{\mathrm{Hz}}$ up to 40 Hz and 10 fT/$\sqrt{\mathrm{Hz}}$ after 1 kHz [83]. The noise in a mu-metal shield depends on the shield aspect ratio.

Here, it can be seen that the shield will limit the previously photon shot noise limited sensitivity to > 16 fT/$\sqrt{\text{Hz}}$. There are two ways to go around this.

One is to use a shield with a different aspect ratio, so that the walls are further away from the atomic vapour cell, reducing the impact of Johnson noise. The other option is to use an internal ferrite shield in place of the innermost mu-metal layer.

The magnetic shielding factor of a ferrite shield is slightly lowered due to the reduction of the permeability of the ferrite in comparison to mu-metal. Ferrite however features higher electrical resistance compared to mu-metal, which reduces the Johnson current noise, in turn reducing the magnetic field noise [84]. Ferrite inner shields feature a typical magnetic noise of ≈ 1 fT/$\sqrt{\text{Hz}}$ [85] or a 10 times reduction compared to mu-metal shields of the same geometry [84, 86].

The magnetic noise contribution from the coil driver configured to provide 10 mA (a field of 1200 nT) produces magnetic noise of ≈ 17.8 fT/$\sqrt{\text{Hz}}$ from 1 Hz up to 100 Hz. and thus becomes the next sensitivity limiting factor.

The radio frequency (RF) coil is excited with a current generated by the analogue output of the NI PCIe-6353 DAQ card. It is a simple voltage source driving a resistor (1 kΩ) in series with the load that acts as a current source. This source unlike the coil drive does not produce constant current and is dependent on the resistance of the coil and the voltage applied. Initially, the RF coil produced noise of 60 fT/$\sqrt{\text{Hz}}$ at the modulation frequency and featured a maximum B-field amplitude of ≈ 1 μT. After finding out the optimal modulation amplitude does not exceed 50 nT, the output resistor was replaced (15.9 kΩ) to maximise the useful dynamic range to 64 nT maximum amplitude and lower the noise to ≈ 4 fT/$\sqrt{\text{Hz}}$. As the RF generation is filtered

It was also discovered that the DAQ card outputs low frequency interference at frequencies of 5, 22 and 150 Hz of the unknown origin. The output resistor was changed to a passive high-pass filter (HPF) with an output resistance of 15.9 kΩ, helping to attenuate unwanted low frequency harmonics in the system. The noise contribution of the RF generation below the modulation frequency is attenuated at a rate of 20 dB per decade. This provides noise of 0.4 fT/$\sqrt{\text{Hz}}$ at 40 Hz. External noise sources affecting the magnetometer are presented in Tab. 3.2.

Table 3.2 – List of external noise sources affecting the magnetometer: at the optimal f_{mod} frequency, in a typical operational bandwidth of 1 - 150 Hz and the estimated total noise contribution.

Source	**Magnetic spot noise at 10 Hz**
Detector photon shot	4.4 fT/$\sqrt{\text{Hz}}$
mu-metal shield	16 fT/$\sqrt{\text{Hz}}$
Coil driver	17.8 fT/$\sqrt{\text{Hz}}$
RF coil	0.3 fT/$\sqrt{\text{Hz}}$
Total	24.3 fT/$\sqrt{\text{Hz}}$

To however be able to resolve the signal of the total noise presented in Tab. 3.2 the analogue input of the DAQ required a modification. The device features a native range of $\pm$ 10 V and a set of pre-amplifiers providing ranges of $\pm$ 5, $\pm$ 2, $\pm$ 1, $\pm$ 0.2 and $\pm$ 0.1 V. The range at which the AC couple photodiode is sampled for noise estimation is at $\pm$ 0.2 V. It was found that the noise floor of the DAQ at the f_{mod} is equal to $\approx$ 234 nV/$\sqrt{\text{Hz}}$ (16.4 fT/$\sqrt{\text{Hz}}$) which is above the photon shot noise σ_{sh}. The solution to this was to operate the AC coupled DAQ channel at its native range of $\pm$ 10 V and then provide our own low-noise pre-amplifier with a gain of 50 to create a custom $\pm$ 0.2 V range. The amplifier was based around OPA2211, which is the same amplifier used for the coil driver that features very low voltage noise and narrow 1/f contribution. The pre-amplifier brings the noise floor down to $\approx$ 20 nV from 100 Hz (1.4 fT/$\sqrt{\text{Hz}}$), allowing for resolution of the photon shot noise. The results of the conversion are presented in Fig. 3.7. The pre-amplifier also features a band-pass filter (BPF) in a range of 0.1 Hz - 5 kHz, to strip the photodiode signal of the direct current (DC) component, and to limit

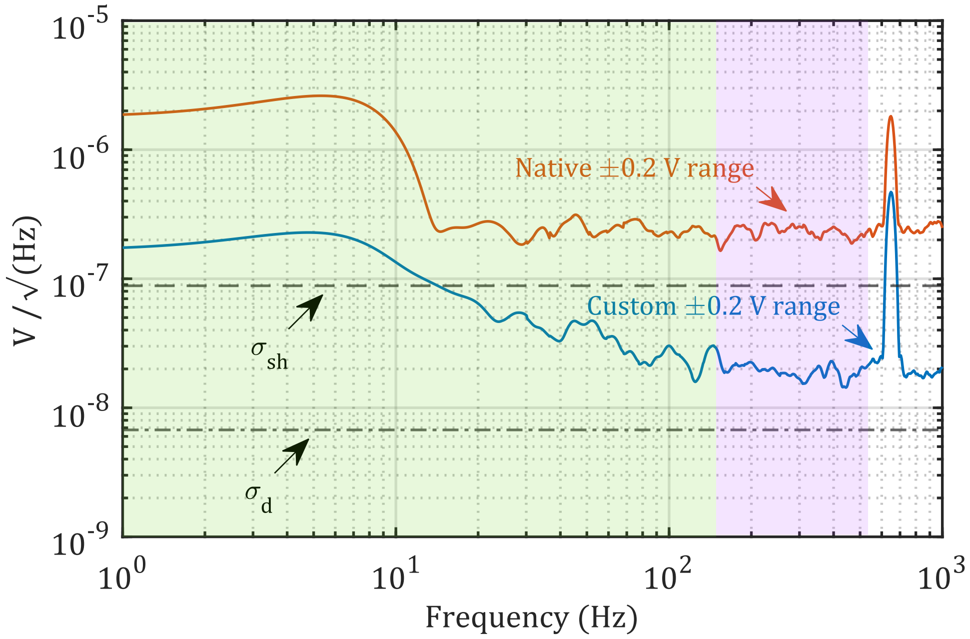

Figure 3.7 – NSD Comparison of stock DAQ ± 0.2 V range and ± 0.2 V range obtained with a custom pre-amplifier. The stock system is presented in red and modified in blue. Photon shot noise σ_{sh} and dark current shot noise σ_{d} added for clarity. The green shaded region presents the magnetometer bandwidth of interest and the purple shaded region presents the modulation frequency range. The signal at 650 Hz is present within the DAQ analogue input itself and is of unknown origin. The NSD was obtained using a logarithmic frequency axis power spectral density (LPSD) [87] algorithm made out of 2048 fast Fourier transform (FFT) points using a Hann window with the amplitude scaling correction applied.

the high frequencies from aliasing the analogue input of the DAQ (625 KSPs). The pre-amplifier gain was verified separately by sweeping its bandwidth with a signal from a function generator and observing the result on an oscilloscope. As the OPA2211 features two amplifiers, the second amplifier was used to duplicate the pre-amplifier for monitor photodetector application.

Another noise source that can still couple into the magnetometer signal is the intensity noise of the laser. Care was taken to minimise the noise by selecting a very low noise current source to drive the laser, however, it would still dominate the detected signal. A solution to this was to include another photodetector (monitor) that is configured in the exact same way as the signal photodetector, sampling the signal before the vapour cell as seen in Fig. 3.1. The signals from both detectors are simultaneously sampled and subtracted in software. This way the intensity noise of the laser can be cancelled. This however comes at a cost of increasing the amplifier noise by 3 dB, as the uncorrelated noise sources (photon shot noise, dark current noise, thermal noise) will be doubled [88]. The addition of uncorrelated noise brings the magnetometer's estimated sensitivity to $\approx 24.7\ \mathrm{fT}/\sqrt{\mathrm{Hz}}$ based on converter electrical noise. The impact of laser intensity noise is presented in Fig. 3.8.

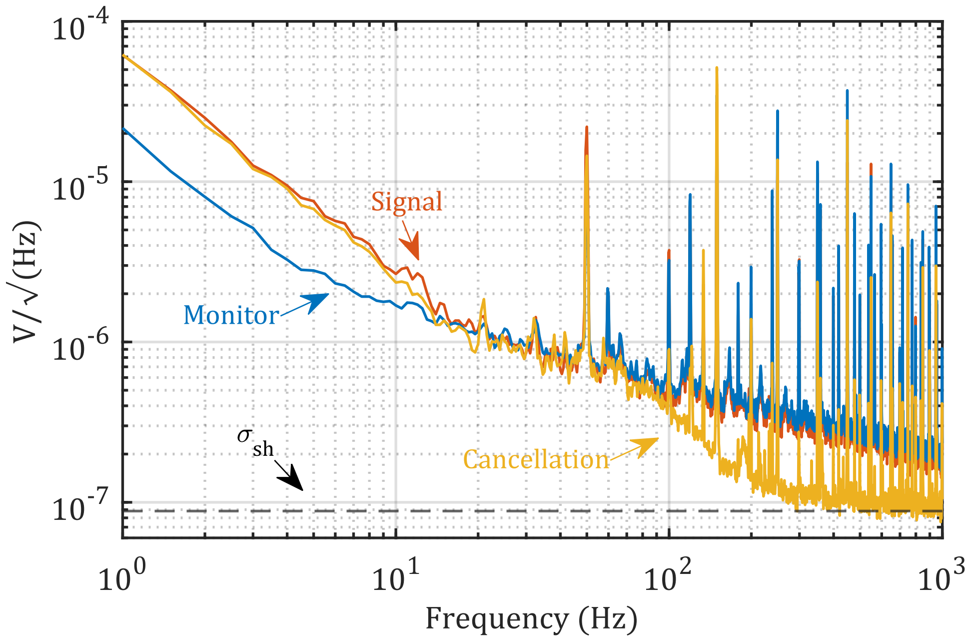

Figure 3.8 – Intensity noise cancellation. The laser was set to output 10 mW and was 60 GHz detuned from resonance to evaluate only electrical and intensity noise without coupling in the magnetic signal. A signal photodetector in red, a monitor photodetector in blue and a subtracted signal of both in gold. Photon shot noise σ_{sh} added for clarity. The monitor cancellation brings the signal sensitivity close to the photon shot noise limit at the modulation frequency. The noise cancellation becomes effective only after 80 Hz. The exact reason behind the intensity noise being uncorrelated at lower frequencies is unknown but is expected to be the combination of low-frequency air-conditioner induced vibration, electrical interference, and the mismatch between channels.

3.4 Magnetometer Performance

The lab-based magnetometer's best sensitivity was found at a cell temperature of 150 °C, with an input optical power of 10 mW split between monitor photodetector and signal photodetector through the cell. The laser frequency was 4 GHz red detuned from resonance ($F = 2 \rightarrow F' = 1$). The f_{mod} was set to 321 Hz with an amplitude, A_{mod} of 25 nT. The sensitivity of the magnetometer is presented in Fig. 3.9.

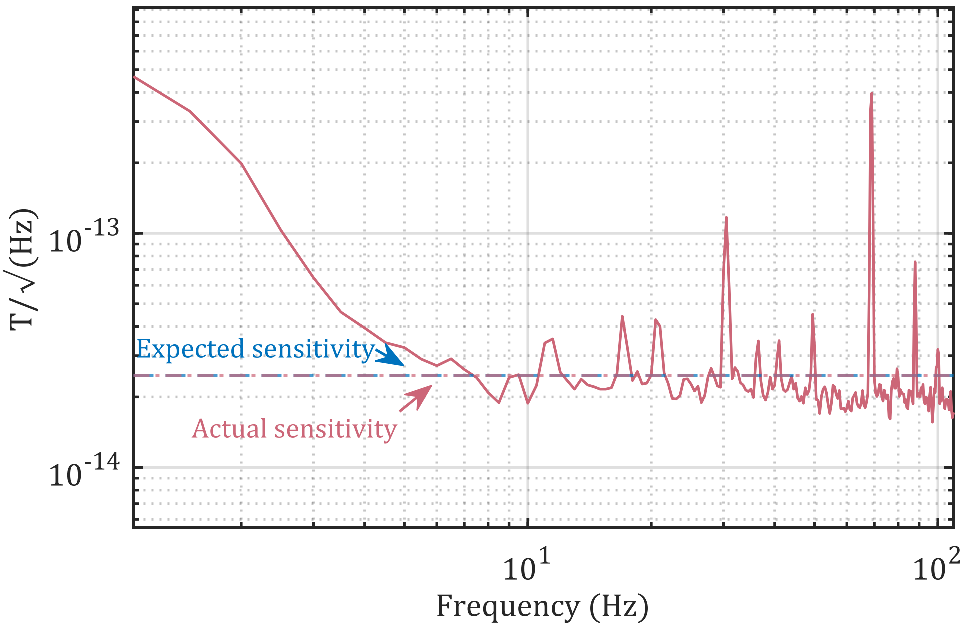

Figure 3.9 – Rb SERF Magnetometer Sensitivity. The magnetometer noise is presented in red, the expected magnetometer sensitivity is presented with a dashed line, actual sensitivity is presented with a dashed-dotted line. Magnetometer achieves a sensitivity of $\approx$ 24.7 fT/$\sqrt{\text{Hz}}$ (estimated around 10 Hz, $\pm$ 2 Hz) tapering to $\approx$ 18.5 fT/$\sqrt{\text{Hz}}$ (estimated around 60 Hz, $\pm$ 5 Hz). The resulting sensitivity matches the expected sensitivity of 24.7 fT/$\sqrt{\text{Hz}}$.

The magnetometer sensitivity was found to match the expected sensitivity (spot noise at 10 Hz). It was also observed that the noise floor begins to taper after 50 Hz. This effect is believed to be caused by the roll-off of the thermal noise contribution from the mu-metal shield (reduction of 16 - 10 fT/$\sqrt{\text{Hz}}$, after 40 Hz)

[83].

To confirm that the dominant noise source is magnetic, it was decided to repeat the optical noise test like the one seen in Fig. 3.8. This time, however, the laser was detuned to its operational detuning of 4 GHz to be magnetically sensitive. The results of this test can be seen in Fig. 3.10. The magnetic noise lifts the overall noise floor above the photon shot noise limit and reveals that the limiting noise source is magnetic in nature.

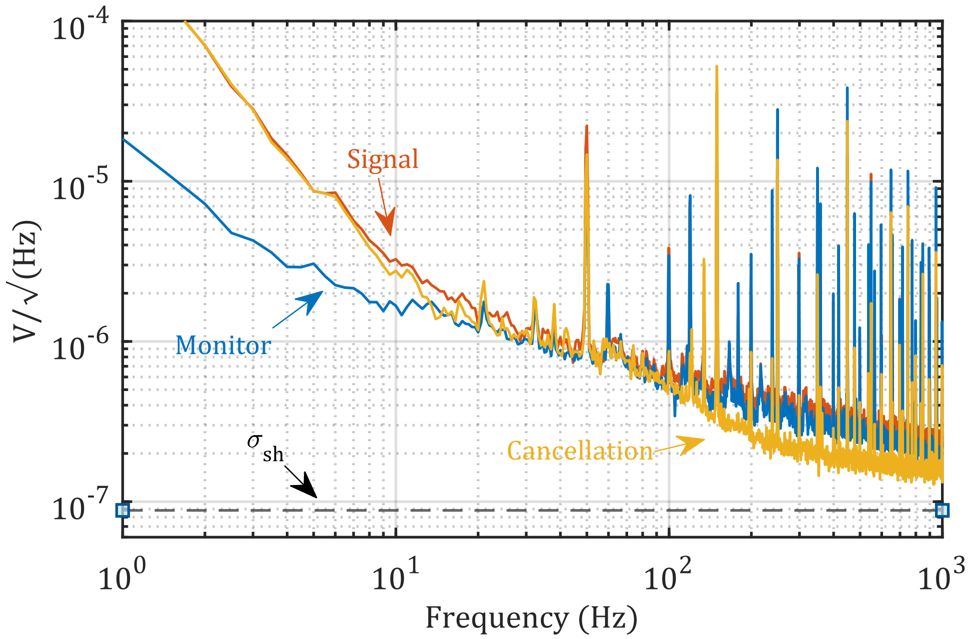

Figure 3.10 – Optical noise at the magnetometer operational detuning (4 GHz). The resulting photodetector cancellation signal is above the photon shot noise σ_{sh}. This implies that the noise perceived here is magnetic in nature.

3.5 Portable SERF Experiment overview

As it was already covered at the start of this chapter, the main motivation behind the development of a Cs-based SERF magnetometer is its lower temperature regime operation in comparison to other alkali species used. This stems from the fact that Cs has the highest density of all alkali metals and largest spin-exchange cross-section, covered previously in Tab. 3.1. The disadvantage is that caesium has the highest spin-destruction cross-section, limiting the maximum magnetometer sensitivity.

Because the Cs atoms do not need to be heated to the same level as other species in order to reach SERF regime, this approach presents an attractive solution for systems that require low SWaP requirements. This technique is of particular interest to medical applications such as magnetocardiography (MCG) or MEG, where an array of magnetometers are utilised and required to be skin safe.

The main intention of the Cs-based SERF magnetometer was that the system could be taken out of the lab environment and taken to field trials. Thus the main objective was to reduce the SWaP of the Rb SERF magnetometer presented in Section 3.1. The experimental setup of the portable sensor within a magnetic shield is presented in Fig. 3.11.

This setup is functionally identical to the one described in Fig. 3.1 in Section 3.1. The main difference being that all of the optical components have been housed inside a custom, 3D-printed sensor package, which can then be positioned with a 5-layer mu-metal shield for testing. This sensor package was designed by Rachel Dawson, who is another laboratory member involved in the SERF magnetometry project covered in this thesis.

The sensor package measures $50 \times 25 \times 25$ mm^3 and is presented in Fig. 3.12. The sensor head is based around a microfabricated silicon glass cell containing ^{133}Cs vapour and is filled with 211 torr of nitrogen, acting as a buffer gas. The cell features an active area of 6×6 mm^2 with 3 mm optical depth. These cells were designed at Strathclyde and manufactured by Kelvin Nanotechnology. Microfabricated vapour cells enable mass production of quantum sensors such as quantum clocks or magnetometers, reducing SWaP and offering a good alternative to otherwise expensive glass-blown cells [15, 89, 90]. The cell used in this experiment is presented in Fig. 3.13.

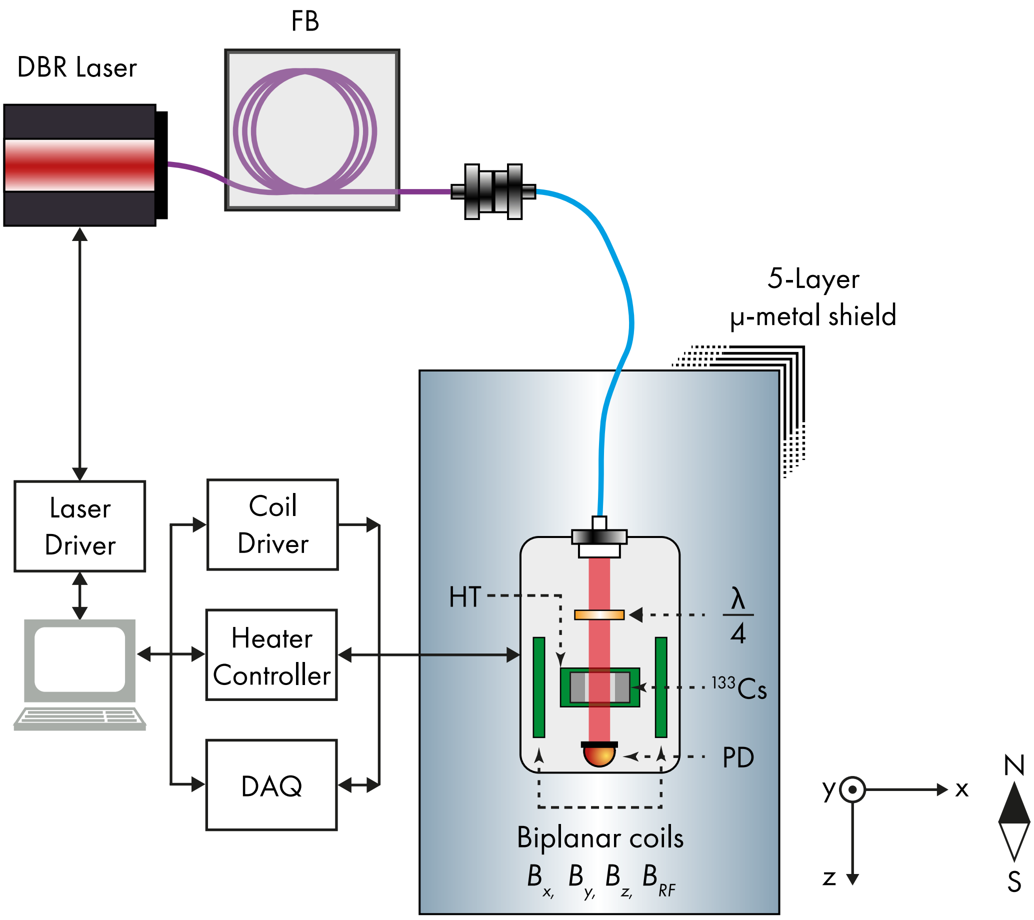

FIGURE 3.11 – Diagram presenting experimental setup of the Cs SERF portable magnetometer. DBR laser: distributed Bragg reflector laser. FB: fiber box. $\lambda/4$ quarter-wave plate. HT: cell heater. ^{133}Cs: caesium 133 MEMS vapour cell. PD: photodiode. DAQ: data acquisition system. This figure also shows the 5-layer magnetic shield.

The ellipticity of light incident on the cell is controlled with a small quarter-wave plate fitted into a custom 3D-printed rotation mount, enabling optimisation of circular polarisation in situ. The rotation mount is presented in Fig. 3.14.

Cell heating is achieved with non-magnetic and low inductance 8 Ω resistor (PCNM series) [91]. These resistors were used instead of the custom resistors covered in Section 3.1 because of the smaller size of the cell that would reduce the custom heater resistance to unacceptable levels for driving electronics.

The mu-metal shield used in this experiment also features field nulling coils like the ones used in the Rb SERF magnetometer. However, as the sensor is to be

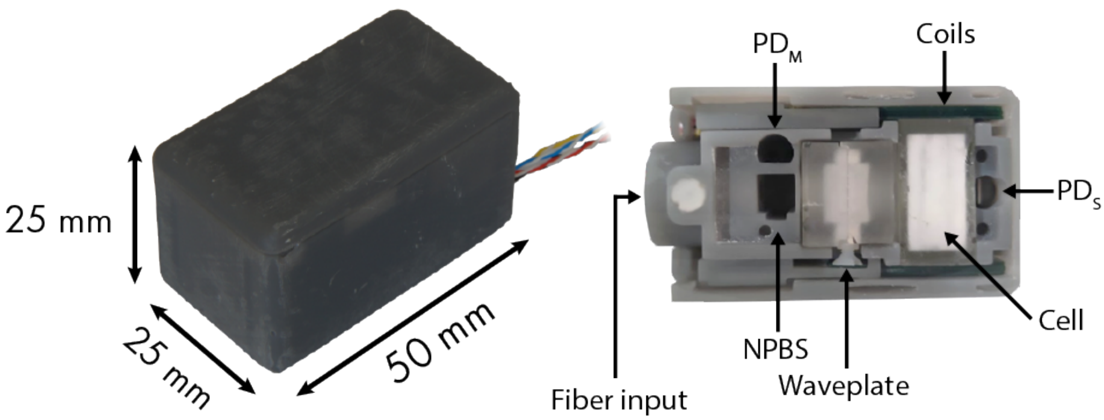

FIGURE 3.12 – Photographs of the portable SERF sensor package. The photograph on the left shows the assembled sensor package including its dimensions. The photograph on the right shows the insides of the sensor head without photodiodes or Cs cell populated. The sensor head features a space for an non-polarising beam splitter (NPBS) and an additional photodiode (PD_M) to be used for cancellation of intensity noise. It was however not utilised for the experiment.

deployed in an magnetically shielded rooms (MSRs), it needs its own nulling and RF coils. The sensor package features bi-planar coils manufactured on two-layer PCBs designed with "bfieldtools" open-source magnetic field modelling software [92, 93]. As bi-planar coils can be manufactured on PCBs they exhibit high repeatability and tight manufacturing tolerance, enabling mass production of sensors. The bi-planar coil assembly is presented in Fig. 3.15. The bi-planar coils feature $\approx$ 10 times lower field to current ratio in comparison to the field nulling coils present in the ^{87}Rb SERF in Section 3.1. For this reason, they were driven with a higher output current version of the coil driver set to provide up to $\pm$ 100 mA of current.

The whole package is insulated with SuperWool® material to make the sensor skin safe. This is the same material that was used for insulating the Rb SERF magnetometer. The sensor head features a non-magnetic fiber collimator (Schäfter Kirchhoff 60FC-4-M12-10-Ti), to interface the laser light tuned to

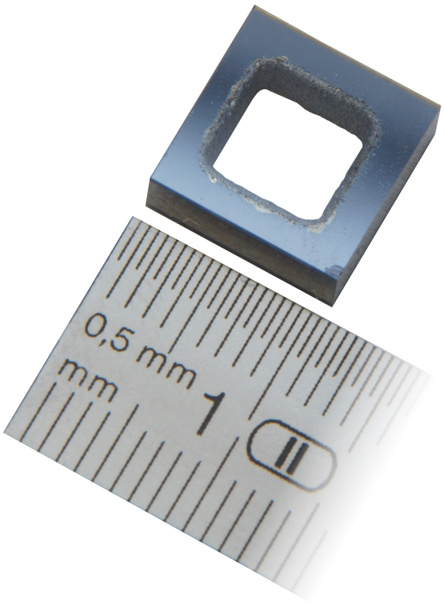

Figure 3.13 – Photograph of Cs MEMS cell used in the portable SERF magnetometer. The cell active area measures $6 \times 6 \times 3$ mm^3 and is filled with 211 torr of nitrogen buffer gas.

$F = 4 \rightarrow F' = 3$ of the D_1 line of ^{133}Cs, into the sensor head.

The laser light is provided by a fiber-coupled DBR laser, similar to the one used in Section 3.1, except centred at 895 nm and featuring maximum output power of 12 mW [94]. It is driven by the same type of laser driver as Rb SERF magnetometer, however with a model capable of providing 200 mA of current instead of 100 mA, due to the lower slope efficiency of the laser.

The level of transmission through the cell is detected with a photodiode (SFH 205 FA) [95], which features the same dimension of the active area as the photodiodes used in photodetectors in Section 3.1. The only difference is that it is packaged in a through hole technology rather than surface mount. The diode also features a visible light blocking filter. Filtering wavelengths below 800 nm preventing stray light coupling into the sensor.

The photodiode does not feature a transimpedance amplifier (TIA) directly inside the sensor head, to limit the amount of magnetic components in the package. The photodiode is instead amplified remotely, outside of the magnetic shield with the

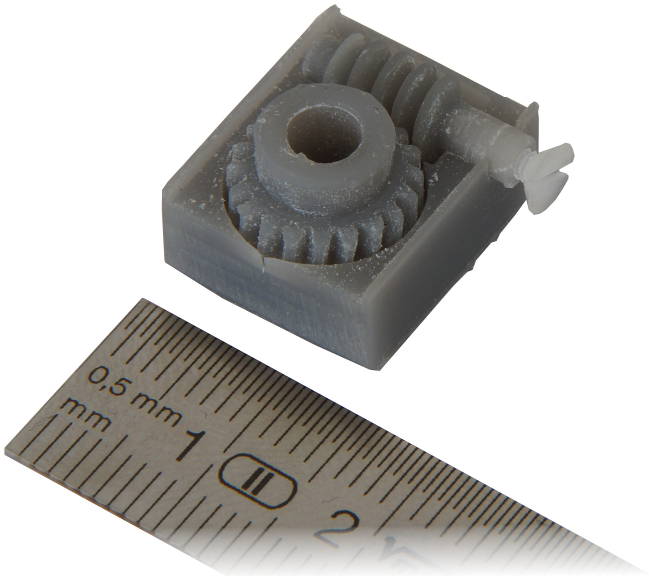

Figure 3.14 – Photograph of partially assembled waveplate rotation mount. Rotation mount allows for control of the degree of ellipticity of the light incident on the cell.

exact same architecture used for the custom photodetectors used in lab-based SERF magnetometer. This TIA is, however, moved to a different PCB form factor. The TIA is interfaced with the photodiode through a shielded twisted pair cable of the type previously used to deliver the power to the photodetectors in the Rb experiment. The cable is configured so that the outer shield is used as a guard for the high impedance connections, to limit the effect of stray leakage current [96]. A 16-bit DAQ system (National Instruments NI USB-6366) is used for both digitisation of photodetector signal and for providing modulation current to the B_{RF} coil.

The optimal operation point for the magnetometer was estimated using parameter scans where optical power, detuning, temperature and modulation parameters are scanned creating a landscape where sensitivity and demodulated line gradient are used as cost functions [82]. The optimisation process revealed that the relatively high optical power of > 5 mW is favoured for the best sensitivity.

The portable magnetometer achieved a sensitivity of 90 fT/$\sqrt{\mathrm{Hz}}$ [82]. This

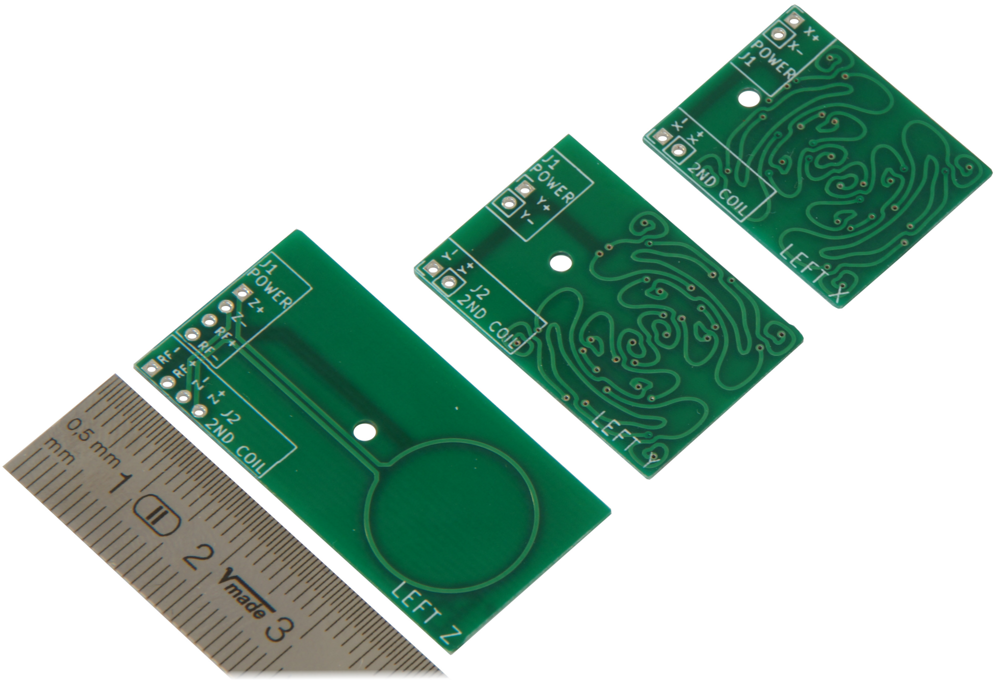

FIGURE 3.15 – Photograph of a single side of bi-planar coils used in the experiment to generate B_x, B_y. The B_z and B_{RF} coils use a simple Helmholtz arrangement for applying modulating field.

sensitivity is believed to be improved once the cell buffer gas pressure is optimised. It has been seen that at higher buffer gas pressures sensitivity is improved, as spin destruction through wall collisions is minimised. This is an ongoing process. The sensitivity is also believed to be partially limited by the intensity noise of the DBR laser.

Further detail about the performance of the portable magnetometer described here, is provided in Rachel Dawson's thesis.

3.6 Synopsis

This chapter focused on the development of lab-based SERF magnetometer using ^{87}Rb as its alkali specie and a portable SERF magnetometer that utilises ^{133}Cs as its alkali medium. Through specially designed custom instrumentation the lab experiment achieved an ultimate sensitivity of ≈ 24.7 fT/$\sqrt{\mathrm{Hz}}$ (estimated around

10 Hz, ± 2 Hz) tapering to $\approx$ 18.5 fT/$\sqrt{\text{Hz}}$ (estimated around 60 Hz, ± 5 Hz). The lab-based magnetometer sensitivity is limited by the noise from the coil driver and partially by the mu-metal shield. It is believed that by re-configuring the coil driver output current and bandwidth, higher sensitivity could be achieved. The next dominant source of noise is the thermal noise in the mu-metal shield used to attenuate the background geomagnetic field. It is believed that by moving to a mu-metal shield with a ferrite inner layer, the sensitivity could be further improved. As it stands, the experiment could be used for investigating low magnetic field applications, such as looking at NMR in various liquid samples.

The design knowledge obtained from work on the lab-based experiment was used for the development of the portable magnetometer. The portable magnetometer achieved a sensitivity of 90 fT/$\sqrt{\text{Hz}}$. This result is believed to be partially limited by the intensity noise of the DBR laser, as well as the suboptimal level of buffer gas in the cell leading to an increase in spin destruction through wall collisions.

Chapter 4

Coil Driver

This chapter focuses on the development and testing of ultra-low noise, highly stable, multichannel current sources that are used for driving field nulling coils in magnetometry applications. With a particular focus on Rb and Cs SERF magnetometer setups covered in Chapter 3.

The work covered here is based on a publication published in Review of Scientific Instruments: "Ultra-low noise, bi-polar, programmable current sources" Review of Scientific Instruments 94, 014701 (2023), 10.1063/5.0002964.

4.1 Motivation

Precise current control is a vital tool in many scientific applications. Examples include: driving laser diodes [97], characterisation of semiconductor devices [98], high impedance tomography and spectroscopy [99], and magnetic field manipulation [100–102]. Each of these applications differs in requirements, but all of them benefit from stability, low noise, and accuracy. This is in particular true for the SERF magnetometry application.

Static magnetic field coils are used for either nulling external magnetic fields, such as Earth's magnetic field, presenting a bias field in a direction of interest, or for testing magnetometers by providing accurate and stable magnetic fields [103].

The SERF magnetometers covered in this thesis operate in close to zero field environments between $\pm$ 25 nT to 500 nT, depending on the desired bandwidth or sensitivity. These fields are much lower than the typical geomagnetic field of 50 μT. As such, Earth's magnetic field needs to be suppressed. The primary geomagnetic background field can be reduced with the use of mu-metal shielding that is internally degaussed [22], or by placement in MSRs. There is, however, some magnetic residue that remains, which needs to be reduced further by means of active compensation. This active compensation must be stable and feature a low noise contribution over the bandwidth of the magnetometer so as not to limit the sensitivity of the device.

The SERF magnetometers have high resolution (in the order of fT [14]) and narrow 1/f noise corner frequency, which makes them ideally suited for applications such as MEG. Low-frequency magnetic noise performance is crucial, as the signals produced by the brain reside in the 0.1 - 40 Hz range, with most sensors for these applications operating between 0.1 - 150 Hz [104]. It is important that the 1/f noise contribution from peripheral electronics is as narrow as possible and that the overall wideband noise performance is not a limiting factor for the magnetometer [60]. The SERF sensors for MEG operate in a MSR with a typical residual field compensation requirement of 50 nT [31]. The magnetic signals arising from the brain have a typical magnitude of 10 - 100 fT [105]. Combining the highest field present, and the lowest signal to be detected gives us a dynamic range in the sub ppm order. In MEG applications, compensation magnetic fields are small, typically requiring currents in the order of 1-10s of mA in the compensating coils. To achieve the sub ppm requirement, the current noise performance needs to be in the range of sub nA/$\sqrt{\text{Hz}}$ across the bandwidth of interest.

Total field sensors, such as ones used for geosurveying, operate in the Earth's magnetic field which has a typical value of 50 μT [101]. These sensors are not as sensitive as zero-field sensors but are able to operate over a much larger range of magnetic fields. The sensitivity of a typical total field OPM is on the order of < 1 pT/$\sqrt{\text{Hz}}$ [106]. The dynamic range of this sensor operating in the background magnetic field of Earth would thus be < 20 ppb. The typical currents required for compensating fields in the total field sensor are in the order of 10 - 100s of mA due to the increased field required to compensate the earth's field. To satisfy the sub ppm requirement, current noise performance in the range of nA/$\sqrt{\text{Hz}}$ is required. In these applications, bandwidth is usually small ($<$ 100 Hz), as the current provided is used for the generation of static fields.

4.2 Requirements

For the Rb SERF magnetometer covered in Chapter 3, it was expected that resonances would be narrow, on the order of < 25 nT (FWHM) and that the residual field present in the shield would be < 1 nT (assuming an average Earth's magnetic field of 50 μT with a shielding factor of 1×10^6 plus magnetic residue from the degaussing process).

Taking the field to current ratio of the shield coils of B_z and B_y which is $\approx$ 67 nT/mA and B_x is $\approx$ 122 nT/mA presents a full-scale output current requirement of at least $\pm$ 1 mA. It was however found that for the optimisation process (scans through different detuning frequencies, cell temperatures and optical powers) that the resonance widths range is broad (25 nT - 500 nT). For this reason, the coil driver current range was extended to $\pm$ 10 mA in order to support resonance widths in that range. This version of the device is the low current source (LCS) and is used for low field generation applications such as SERF.

As the current source will be used for automated scans, the device must feature software control of the independent outputs. To maintain a high dynamic range and have the ability to provide enough sample points for resolving very narrow resonances the device needs to feature high bit resolution. When performing a zero field scan $\approx$ 250 points are used over the full current range, which is later fitted to a Lorentizian or Gaussian lineshape. Additional resolution is required to better match the zero crossing derived from the fit, as well as account for different resonance widths encountered in the scans. For this reason, it was decided that each point from the scan could be further divided into an additional 64 steps. The minimum digital to analogue converter (DAC) bit resolution is given in Eq. 4.1

$$DAC_{\mathrm{R}} = log_2(S_{\mathrm{N}} \times S_{\mathrm{R}}) \ , \tag{4.1}$$

Where the number of steps in a scan, $S_{\mathrm{N}} = 250$, and additional step resolution $S_{\mathrm{R}} = 64$, bring the required bit resolution of the DAC, DAC_{R} to $\approx$ 14-bit.

To enable rapid scans of the field in order to find the zero field operational point, it was decided that the bandwidth of the current sources should be at least 100 Hz. The selected bandwidth ensures that scans can be taken quickly with enough steps to resolve the GSHE resonance curves while at the same limiting broadband noise contribution.

It was also decided for the design to be flexible and feature a version that supports higher current output $<$ 250 mA but maintains the same dynamic noise performance. This version is used for other magnetometry experiments that require generation of higher magnetic fields for testing. It is also used for low field generation applications that feature coils with low field-to-current ratio geometry. This version of the device is known as the high current source (HCS).

4.3 System design

The simplified architecture of the current driver is shown in Fig. 4.1. The design can be broken into four sections: the external interface; digital control (Fig. 4.1a); signal conditioning (Fig. 4.1b); and output driving (Fig. 4.1c). The LCS and HCS only differ in how they implement the driving stage.

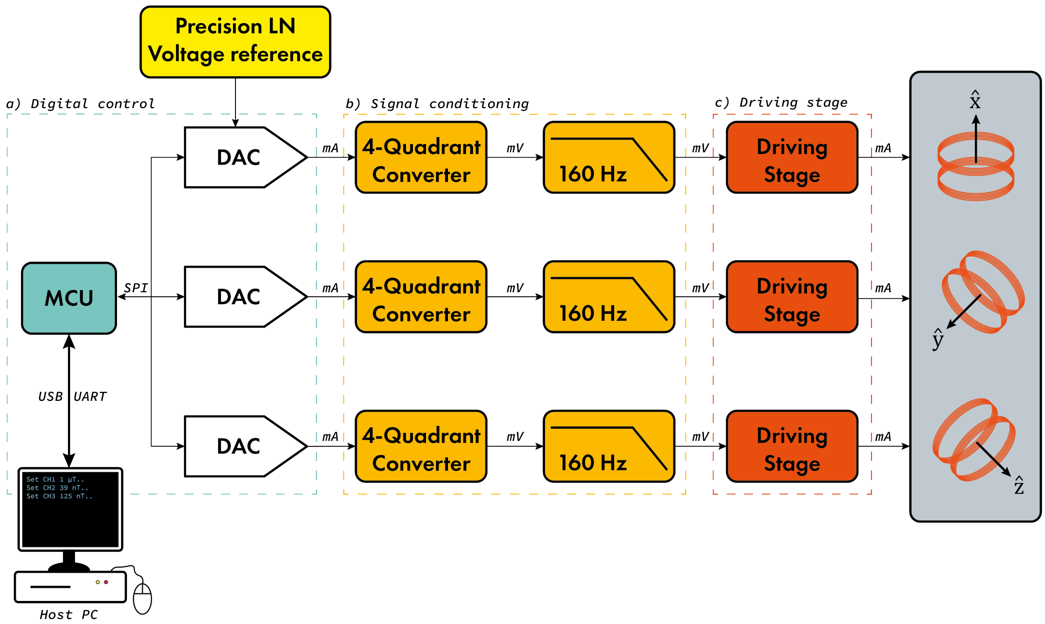

FIGURE 4.1 – Simplified architecture of the coil driver system. The design is split into three sections: (a) digital control, (b) signal conditioning, (c) and driving stage. The design is realised on a four-layer PCB with the signal conditioning and driving stages protected by EMI/RFI shielding. The design files, such as the schematic, board layout and bill of materials are available on GitHub [107]

4.3.1 INTERFACE

The device can be powered from either a lab bench power supply ± 10 - 16 V or an equivalent battery source. The incoming power is regulated with a complementary pair of TPS7A4700 [108] and TPS7A33 [109] (Texas Instruments) low-dropout regulators (LDOs). These feature ultra-low noise and high power supply rejection ratio over the bandwidth of interest ensuring low noise operation without having to rely on expensive power supplies to achieve the best performance.

Each channel output is fed into a corresponding BNC connector and a single RJ45 interfacing coils to the driver. RJ45 connectors are widely used in our group, as they offer an inexpensive source of shielded twisted pairs.

4.3.2 Digital control

The current source is controlled by the ATmega4809 [110] (Microchip) present on an Arduino Nano Every board. The Arduino ecosystem was chosen for its accessibility and ease of programming for those unfamiliar with programming embedded systems. Basic firmware was written to cover general use cases. The device receives commands through a universal serial bus (USB) serial connection and controls the appropriate DAC to set the output current for each channel.

The output current can be described by the transfer function in Eq. 4.2, where $I_{\max}$ is the highest uni-polar current that the source can provide, $FSC_{\max}$ is the full-scale count value of the DAC (16-bit = 65535), and CC is the current count value of the DAC that has been set by the user.

$$I_o = \frac{2 \times I_{\max}}{FSC_{\max}} \times (CC - \frac{FSC_{\max}}{2}) \; . \tag{4.2}$$

For example, in the basic firmware provided, sending the command "*<!chan 2 45547>*" would set an LCS configured for $I_{\max} = 10$ mA to output $+$ 3.9 mA on channel 2.

The Arduino platform makes it easy to customise the firmware for specific use cases, such as arbitrary waveform generation or triggered outputs.

The primary signal used to control the current source is generated by a DAC. As the foundational signal, it is important to minimise noise at the DAC output as it will be amplified by the later conditioning stages. For this design the 16-bit DAC, DAC8814 [111] (Texas Instruments) was selected. This is a four-channel, current multiplying DAC. The current multiplying architecture was chosen as it features excellent linearity, fast settling, and low glitch energy and allows for the output to be conditioned externally [112]. This approach allows for a higher level of customisation of the conditioning stage, which can be tailored to the user application. By changing the transimpedance amplifier in the conditioning stage, the designer can select amplifiers that favour precision, low noise or high speed. For example, the device can be optimised for low frequency applications (such as sweeping the static field in a SERF magnetometer) or for high frequency applications (such as oscillating test fields for RF magnetometers).

The noise performance of the DAC8814 is highly dependent on the noise of its voltage reference. Voltage references are often the noise-defining component in analogue systems, due to shot noise present in the Zener diodes that make up the reference [113]. For this reason, the DAC8814 is driven by a 2.5 V precision reference LTC6655LN [114] (Analog Devices). This voltage reference features an output filter that drastically reduces the impact of 1/f noise as well as wideband noise.

4.3.3 Signal Conditioning

The output of the DAC8814 is a uni-polar current. The conversion to bipolar output is done using a 4-quadrant converter circuit. The converter is composed of a transimpedance amplifier followed by an inverting summing amplifier that combines the voltage reference with the output of the transimpedance amplifier in a 1:2 ratio. This converts the uni-polar output to a bi-polar one. It is based around an OPA2210 [115] (Texas Instruments) which is a very low 1/f noise part with excellent DC performance.

The final signal conditioning stage is a noise suppression filter that can be optimised to the desired application. For example, the reference implementation for a MEG SERF sensor (described in Chapter 3) implements a low-pass filter (LPF) with a cutoff frequency of 160 Hz to match the expected MEG signal bandwidth, and bandwidth of the magnetometer [116]. This filter is implemented as a 2nd-order Butterworth LPF in the Sallen-Key configuration. The Sallen-Key configuration was selected as it allows for inherently higher gain accuracy and stability in comparison to the multiple feedback architecture, which requires component matching for unity gain application. The unity-gain Sallen-Key configuration instead relies on the operational-amplifier (op-amp) parameters rather than the tolerance and stability of the passive components that form the filter [117].

The signal conditioning stage and driving stages are shielded with an electromagnetic interference (EMI) shield on the PCB to minimise EMI as well as radio frequency interference (RFI) induced noise on the output current.

4.3.4 Driving stages

Customisation of the digital control and signal conditioning stages requires only a change in component values. The need to provide a variety of maximum output currents requires different circuits entirely, and hence multiple different designs are necessary. Their configuration depends on the maximum current that is required and the relative noise performance that is to be achieved. Two driving stages tailored to specific applications were designed: a LCS design targeted at SERF applications and a HCS design targeted at total-field applications.

4.3.4.1 Low Current Source (LCS)

The LCS is used for generating small currents not exceeding 50 mA, which are used in our SERF system for small bias field (0.5 μT) cancellation through the use of Helmholtz coils. This configuration aims to provide high impedance over the frequency range of interest as well as stability. The driving stage is based around a Howland current pump (HCP) [118]. This circuit can be realised with a single amplifier and four equal value, precision resistors. The choice of amplifier and resistors is crucial to ensure the performance of the device [119]. The standard HCP architecture from Ref. [119] was used for the design.

The HCP was implemented using an OPA2210. This is the same part used in the signal conditioning stage, which helps reduce the bill of materials size. The key features that make it suitable for the HCP are its architecture and the driving stage, which can source and sink up to 60 mA. It features a very low offset of 5 μV and ultra-low noise contribution in both input voltage and current. Its architecture is based around bipolar transistors, thus its 1/f noise is much smaller than that of complementary metal–oxide–semiconductor (CMOS) amplifiers [120], resulting in lower overall noise in the bandwidth of interest (DC - 160 Hz). The device was also selected based on its very high common-mode rejection ratio, which is in excess of 132 dB. This is crucial for HCPs to maintain their high impedance across a wide frequency range. This allows their use in applications requiring the generation of AC magnetic fields in excess of 10s of kHz [119], such as generating test fields for coils for RF magnetometers. To meet the requirement for well matched resistors, thin-film resistors with a tolerance of 0.1 % and a temperature coefficient of 25 ppm/K were selected. Such resistors offer a good balance between performance and cost. The combined use of low temperature coefficient resistors as well as low drift active components help to maintain good stability against temperature.

The maximum practical current that the LCS can be configured to provide is $\approx$ 50 mA. After this point, the resistors forming the HCP begin to heat-up unevenly. The resulting decrease in CMMR degrades the noise floor and accuracy of the driver. The minimum practical current that the device can be configured to provide a full range is $\approx$ 25 μA. In this configuration, the amplifier is still capable of resolving 16-bits of resolution provided by the control circuitry. Values smaller than this would be consumed by the input bias current which would lead to non-monotonicity of the output. It is important to note that at these currents, connections to the coils may become an issue as stray current pickup can become a significant source of error.

4.3.4.2 High Current Source (HCD)

Many applications, such as those with constrained coil geometries, require a higher peak current than the LCS is capable of providing. Components and circuits that can provide higher peak currents usually have a non-linear trade off in their noise performance.

The HCP output stage is unable to provide such output currents without losing efficiency, and potentially accuracy due to the self-heating of the control stage. The "improved" HCP stage could be implemented as the efficiency is much greater, however, it also requires an op-amp that can deliver 250 mA to the load. Amplifiers like these exist but they do not match the noise performance of the likes of precision amplifiers such as the OPA2210. Another disadvantage is the fact that the drive circuitry is thermally coupled to the control loop. This in turn negatively affects the accuracy as the components begin to heat up.

The solution was to utilise the existing amplifier (that was previously used as a HCP) and turn it into the control driver for a class AB amplifier stage, which delivers the final output current. The circuit is presented in Fig. 4.2.

The amplifier is implemented using a complementary pair of NPN/PNP (2SC5566/2SA2013) [121] transistors (Q_1, Q_2). These transistors offer good power dissipation of up to 3.5 W, high current gain and low saturation voltage, meaning that they can be driven more easily from lower voltages. The complementary pair is controlled by the OPA2210. By putting the complementary pair in the feedback loop of the OPA2210, high accuracy can be maintained while increasing the output current capability. The pair is not matched hence multi-turn trim-pots (VR_1, VR_2) are used for adjustment of the bias current for each arm.

The thermal run-away condition, common in class AB stages [122], is mitigated with the use of a small heat-sink that thermally bonds the complementary pair and the series bias diodes (D_1, D_2), keeping them at the same temperature. To

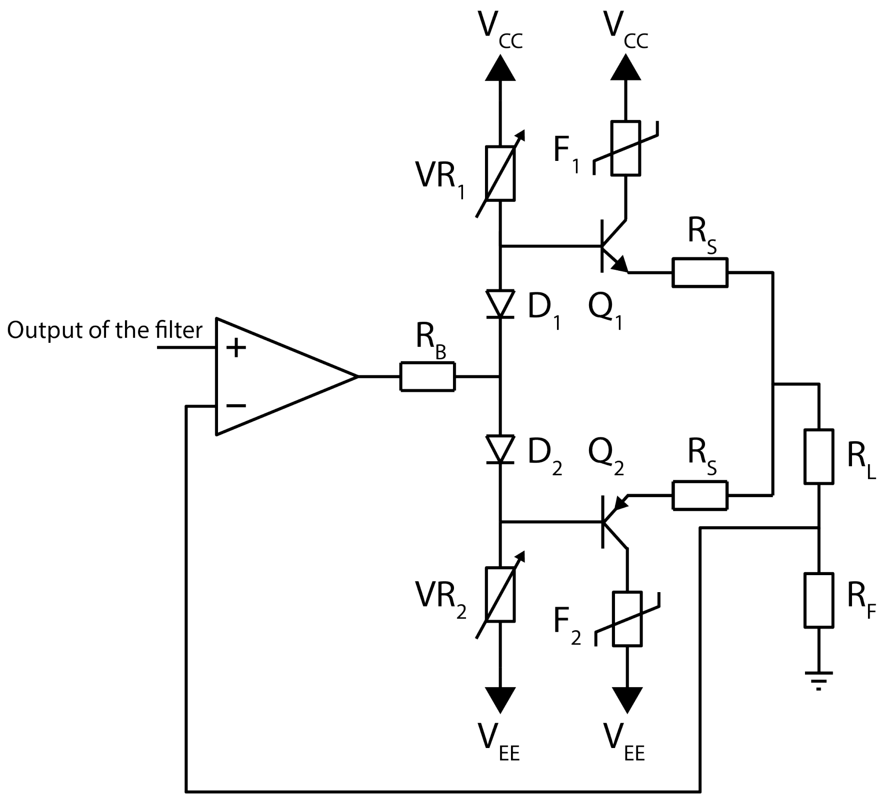

Figure 4.2 – Simplified schematic of a single output channel of the HCS. The design uses a class AB stage driven by an OPA2210 op-amp. Complete schematics and design files can be found on GitHub [107].

further improve thermal run-away resistance, the design is equipped with polyfuses at its collectors (F_1, F_2) and small 0.47 Ω series resistors (R_S) from each emitter in the path of the load. This configuration allows for high current generation while maintaining the high accuracy and noise performance found in the preceding stages. The class AB stage is also thermally decoupled from the OPA2210 as it is placed further away, minimising temperature effects on the control circuitry. The feedback resistor R_F, which determines the output current, is capable of dissipating 3 W and features a temperature coefficient of 20 ppm/K and a value of 10 Ω (for 250 mA output). Although the resistor will never dissipate more than 625 mW (for the 250 mA version) the extra clearance allows it to remain at a cooler temperature, which minimises temperature effects on accuracy. By using a single feedback resistor, the maximum output current can be easily changed by swapping a single component. Note that the output is not directly referenced to ground but rather "floats" on top of the feedback resistor R_F. This prevents the output from being probed with a single-ended probe that is referenced to ground. The maximum practical current that can be set on the HCS is $\approx$ 250 mA, which is limited by the transistor thermal performance. Higher currents can be achieved by the use of polyfuses with higher rated current and replacement of the output stage transistors. The minimum practical current that the device can be configured to is $\approx$ 50 mA. The device can be configured to output lower full-scale currents, however at that point it would be more beneficial to use the LCS which features lower noise and better accuracy.

4.4 Device testing

The LCS and HCS were tested to measure their performance in three key areas: noise, stability and accuracy. For each test, measurements were taken in a temperature-controlled lab, maintaining a constant 21 °C. All of the instruments were left on for at least an hour before any measurements were taken to reach thermal equilibrium and to ensure the best accuracy and stability.

4.4.1 Noise test

The noise spectrum of the current sources was measured to assess both the noise shape and levels. Measurement of noise in low noise devices always presents a challenge, and this is especially true for accurate 1/f noise measurements. High amplification is required for the noise signature to be visible on the measurement equipment. The expected noise floor of the current source was on the order of pA. Across the load of each device, this translated to needing to measure voltages on the order of nV. In order to reduce the dynamic range requirement of the measurement to a practical level, an AC high pass filter with a cutoff frequency close to DC (0.01 - 0.1 Hz) was also required. Typically, this measurement arrangement is formed by combining a high-resolution oscilloscope with a high-gain pre-amplifier. A PicoScope 4262 [123] (Pico Technology) was used as the measurement device. It features 16-bits of vertical resolution and an internal pre-amplifier allowing for measurements at 2 mV per division in a 5 MHz bandwidth. To reach the desired measurement range, the pre-amplifier required a gain in excess of 10000. It also required 1/f noise to be lower than the device under test. I have developed our own pre-amplifier to meet these requirements. Details on the pre-amplifier design and performance can be found in Section 4.5. The test setup for noise measurement is presented in Fig. 4.3.

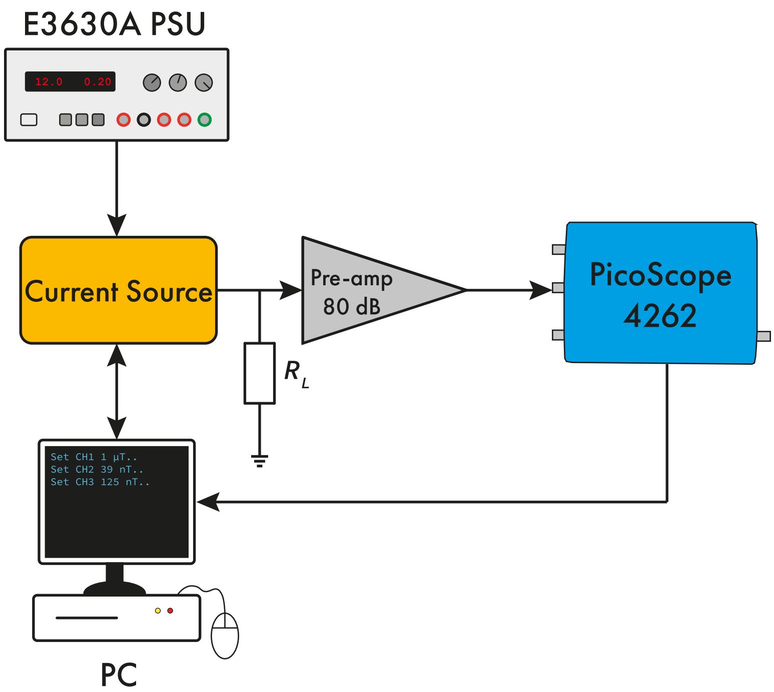

FIGURE 4.3 – Block diagram of the test setup used for noise measurement. The current driver was powered up from a ± 12 V PSU (E3630A). The current driver was connected to the laptop through a galvanically-isolated USB for communication. The outputs of the LCS were 300 Ω terminated with 0.1 % tolerant, low-temperature-coefficient resistors. For the HCS no termination was used as the current sense resistor acts as a load. The signal was further amplified by the oscilloscope and captured.

The current driver was powered from a Keysight E3630A [124] series power supply and controlled through a laptop. The device was connected through an external USB isolator to avoid any potential ground loops that could upset the measurement. For LCS measurements, the output was terminated using a 0.1 % 300 Ω terminator to convert the current into a voltage that can be amplified by the custom pre-amplifier. For the HCS the voltage across the R_{F} resistor is used as the input to the pre-amplifier, with R_{L} replaced by a 1 Ω 50 W dummy load. Measuring across R_{F} instead of R_{L} removes the need to use a device capable of measuring a floating voltage. In both cases, the amplified signal was then captured by the oscilloscope.

Due to how the pre-amplifier is constructed, the input capacitor takes around 5 - 10 minutes to achieve the desired level of low leakage for the reading to stabilise around zero. The oscilloscope was set to DC coupling for each test as the internal AC coupling effectively blocks frequencies below 10 Hz, making it unusable for these tests.

To confirm that the noise floor of the measurement system was below the noise floor of the device under test, the pre-amplifier input was terminated with a 300 Ω terminator. One hundred seconds of data were captured, at 10 kS/s to ensure that there were enough samples to capture the low-frequency components present in the signal.

After verifying the measurement system, a LCS device was tested. The LCS was populated to have a maximum output current of 10 mA and set to output the maximum 10 mA on one channel. After the signal was captured, the channel was reset back to 0 mA and the process was repeated for the remaining channels. The noise density of a single channel is presented in Fig. 4.4. Key results for all channels are presented in Table 4.1.

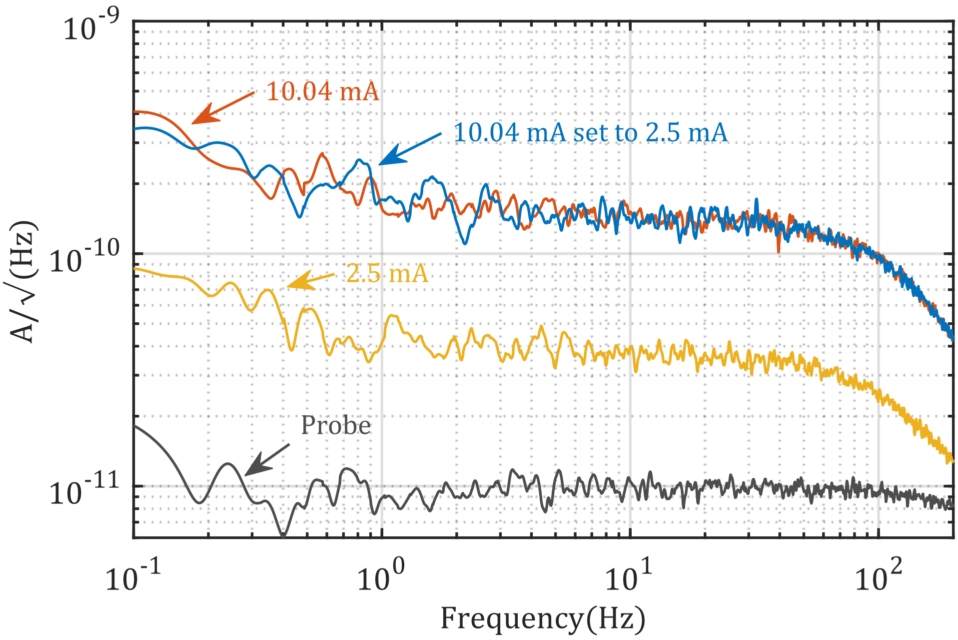

Figure 4.4 – NSD results in a bandwidth of 0.1 - 200 Hz for the LCS. 10 mA configuration (red), 2.5 mA configuration (gold), 10 mA configuration set to output 2.5 mA (blue) and noise floor of the setup terminated with a 300 Ω resistor (black). Channel 3 is the only one shown to improve readability. Other channel results are presented in Table 4.1. The NSD was obtained using a LPSD algorithm [87] made out of 2048 FFT points using a Hann window with amplitude scaling correction applied.

Table 4.1 – Noise performance summary of different configurations of the current source. $\mathcal{R}$ indicates noise relative to range at a frequency band of ± 5 Hz, centered at 10 Hz.

Configuration	**CH1**	**CH2**	**CH3**
(LCS) 10 mA	151 pA/$\sqrt{\text{Hz}}$	147 pA/$\sqrt{\text{Hz}}$	146 pA/$\sqrt{\text{Hz}}$
(LCS) 2.5 mA	38 pA/$\sqrt{\text{Hz}}$	38 pA/$\sqrt{\text{Hz}}$	38 pA/$\sqrt{\text{Hz}}$
(HCS) 250 mA	4.1 nA/$\sqrt{\text{Hz}}$	4.1 nA/$\sqrt{\text{Hz}}$	4.1 nA/$\sqrt{\text{Hz}}$
(LCS) $\mathcal{R}$ 10 mA	15 ppb/$\sqrt{\text{Hz}}$	15 ppb/$\sqrt{\text{Hz}}$	15 ppb/$\sqrt{\text{Hz}}$
(LCS) $\mathcal{R}$ 2.5 mA	15 ppb/$\sqrt{\text{Hz}}$	15 ppb/$\sqrt{\text{Hz}}$	15 ppb/$\sqrt{\text{Hz}}$
(HCS) $\mathcal{R}$ 250 mA	16 ppb/$\sqrt{\text{Hz}}$	17 ppb/$\sqrt{\text{Hz}}$	17 ppb/$\sqrt{\text{Hz}}$

It can be seen that the signal is not limited by the noise floor of the measurement setup and that the 1/f noise effectively vanishes after 1 Hz, leaving only wideband noise. The average noise floor was calculated at 10 ± 5 Hz, as it is in the flat band between the 1/f noise and the high-frequency roll-off of the device.

To achieve the lowest possible noise it is important to configure the maximum output of each current driver to the lowest possible limit required by the application. To demonstrate this, the previous test was repeated using the same LCS but with the current set to 1/4 full-scale (2.5 mA). The result is shown in Fig. 4.4 (gold). The trace overlaps the full-scale output trace, showing there is no improvement in absolute noise performance by programmatically reducing the output current.

To test the scalability of the device, a second LCS was built with the maximum output current set to 2.5 mA. This was achieved by swapping four resistors and a capacitor in the driving stage of each channel. The noise test was re-run and the results are presented in Fig. 4.4 (gold) and Table 4.1. Compared to the 10 mA LCS, a 4x reduction in maximum current resulted in an approximately 4x reduction in wideband noise. This result shows that the ppb relative scaling has been maintained, however, it is expected that for lower output configurations Johnson noise and other noise sources present in the design would start to dominate and would no longer scale with the maximum current output. The optimum peak output current can be selected on a per-device basis based on a balance between absolute noise performance, relative noise performance and minimum step size.

The noise test was performed on an HCS that was configured to provide 250 mA full-scale current. The results of this are presented in Fig. 4.5 and Table 4.1. Compared to the 10 mA LCS, a 25 times increase in maximum current results in only a minor degradation of relative noise performance.

The noise testing methodology was verified externally using an independent OPM to measure the magnetic noise contribution when the current sources were used to drive the static field coils.

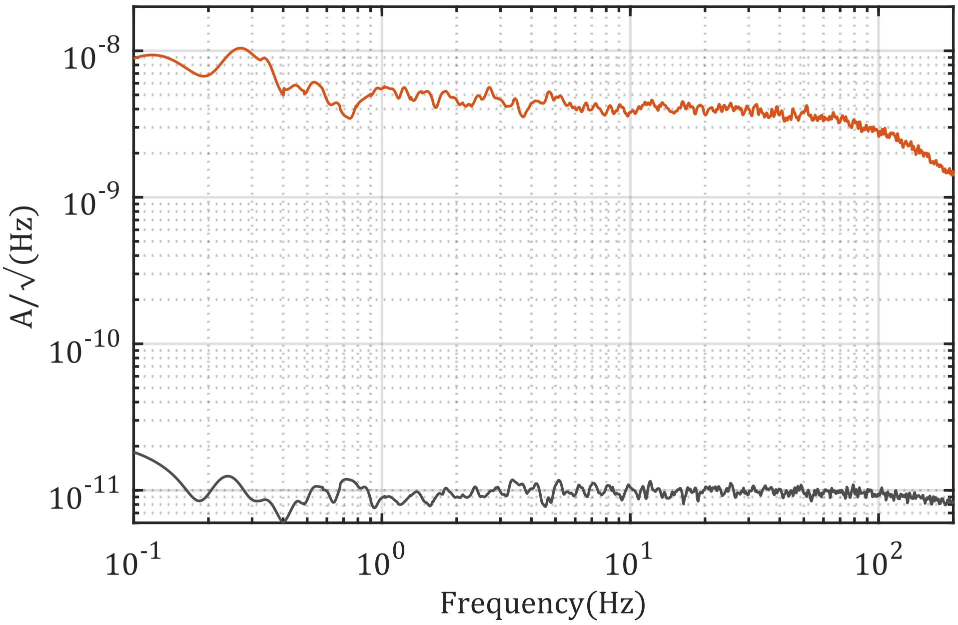

FIGURE 4.5 – NSD results in a bandwidth of 0.1 - 200 Hz for the HCS. 250 mA configuration (red) and noise floor of the setup terminated with 300 Ω resistor (black). Channel 3 is the only one shown to improve readability. Other channel results are presented in Table 4.1. The NSD was obtained using LPSD algorithm [87] made out of 2048 FFT points using Hann window with amplitude scaling correction applied.

4.4.2 Stability test

For the long term stability test, the oscilloscope and pre-amplifier were replaced with a Keysight B2901A [125] precision source measure unit (SMU). The current was measured directly without the use of terminators or dummy loads as the SMU effectively becomes the load. The SMU was expected to have a smaller impact on stability in comparison to the pre-amplifier and oscilloscope making it ideally suited for low cadence long term testing. This feature however prevents it from being used for the bandwidth of interest for noise measurements, as its sampling rate of 10 Hz is insufficient. The test setup for stability measurement is presented in Fig. 4.6.

The stability test was first performed on the LCS configured to provide a full-scale

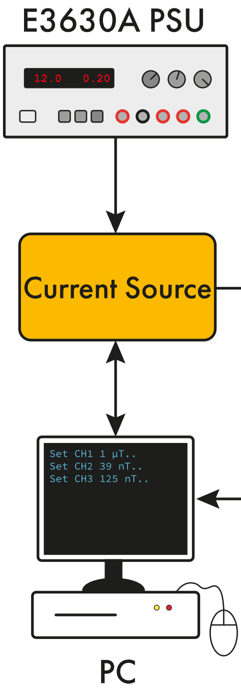

Figure 4.6 – Block diagram of the test setup used for stability and accuracy measurements. The setup is almost identical to the "noise measurement setup" in Fig. 4.3 except that the SMU is directly used as the load, instead of using a pre-amplifier and an oscilloscope.

current of 10 mA. The device was set to provide about 10 % of its full-scale output (1.004 mA), and monitored for 24 hours. The reason for choosing this output was to maximise the resolution of the SMU which changes its range and loses a digit after 1.1 mA. As shown before in the noise testing section, setting a smaller current without re-configuring the device does not impact its noise performance. The device was set to take 345600 measurements at a sampling frequency of 4 Hz. This frequency was selected to ensure that the SMU analogue to digital converter had enough time to fully settle. This test was repeated for the HCS configured to provide up to 250 mA and set to output 30 % of its range. Both 1 mA and 100 mA test ranges of the SMU were also tested by shorting the input of the device, to get an estimate of the stability of the measurement system itself.

The stability was estimated using the overlapping Allan deviation [126, 127], which is often used to characterise instrumentation stability [128, 129]. The result was later normalised by dividing by the measurement range as seen in Fig. 4.7.

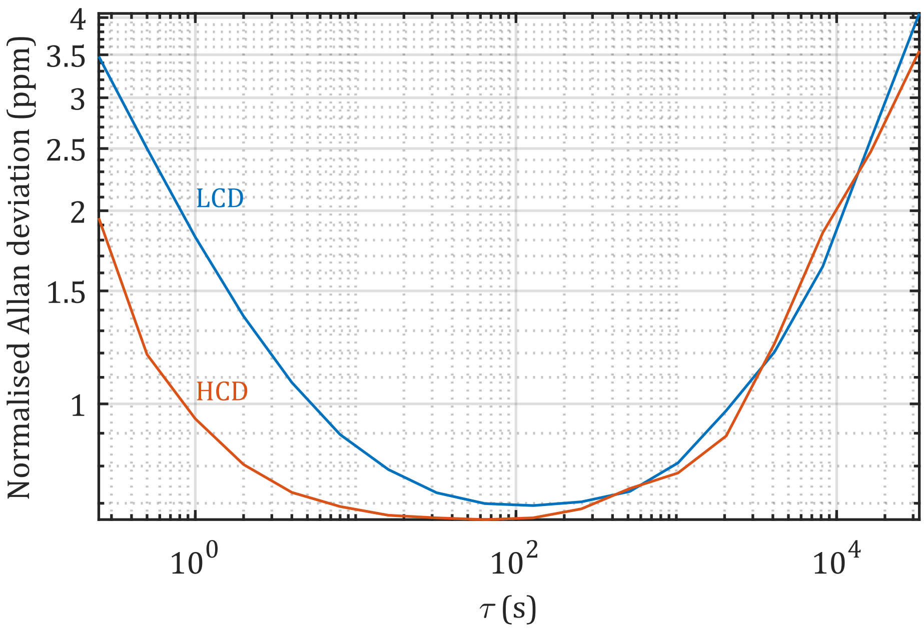

FIGURE 4.7 – Allan Deviation of both devices, LCS set to 10 % and HCS set to 30 % of their full-scale output for 24 hours. LCS (blue) and HCS (red). The first point of the graph shows the ppm stability performance that matches well with the data obtained using the pre-amp and oscilloscope. The improvements from averaging are most notable after around 100 seconds. The device exhibits a long term low frequency drift, but even after 24 hours, it does not drift far enough to compromise its performance.

It can be seen that both devices perform similarly and achieve their best performance after around 100 seconds of averaging, followed by a long term low frequency drift. It is important to note that the ppm stability performance achieved at the start is maintained for at least a working day. The shorted SMU produced better stability for both ranges, indicating that the measurement system was not the limiting factor. It is expected that the long term drift could be mitigated by using components with lower temperature coefficients and zero-drift amplifiers, however doing so could potentially compromise the wideband performance of the device. It is important to state that the long term stability was not a driving requirement, as most of our applications only require a relatively short term stability (less than one hour).

4.4.3 Accuracy test

A scheme was devised to test the current driver accuracy that used the same test setup as the stability testing outlined in Fig. 4.6. The current source was programmed to go through its 16-bit range in 32 counts steps. This step size was sufficient to show any gain error without the need to test every possible DAC value. The SMU needs at least 200 ms to fully settle making a sweep through a full range possible but impracticable, as it would take approximately 3.5 hours per channel. Sweeping through a single channel with a step size of 32 (for a total of 2048 steps) takes approximately 7 minutes, totalling 21 minutes for all of the channels.

The data was then compared to the theoretical accuracy given by Eq. 4.2 and the difference was converted into DAC counts. The results are shown in Fig. 4.8.

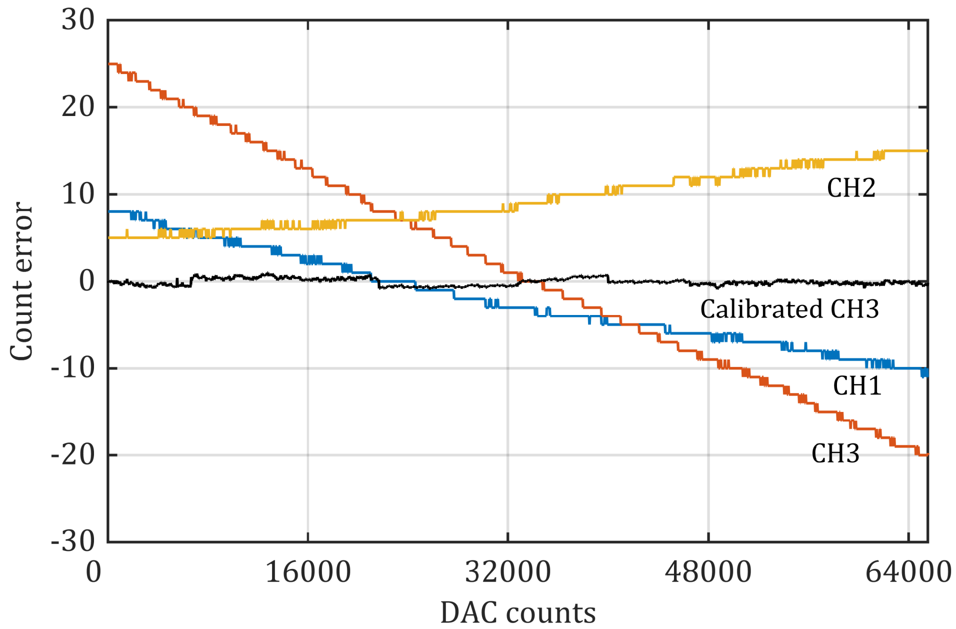

Figure 4.8 – Device count accuracy results. All channels were calibrated but channel 3 is presented for clarity. The result of calibration shows a maximum error of $\pm$ 1 least significant bit (LSB).

The results show that the main source of error is the gain error (demonstrated by the non-zero gradient of the line) followed by the offset error. A look-up table (LUT) based compensation method was implemented on the Arduino. The LUT was populated using the error count derived from the calibration routine, with one correction value for each 32 count block. Testing showed that the calibration routine increased the accuracy to within $\pm$ 1 LSB ($\pm$ 15.3 ppm), as shown for channel 3 in Fig. 4.8. It is important to note that the baseline accuracy exhibited at worst a $\pm$ 25 count error with no alteration to the circuit. This result is notable when considering that no matching of components was performed. This shows that the device can be used without an explicit need for calibration, as the percentage error is less than 0.04 % which is negligible for our application. Note that 2048 steps were not actually needed to resolve the gain error and that potentially the data could be compressed into bigger chunks which would speed up the calibration process.

4.4.4 Comparison to other devices

The reconfigurable nature of the LCS and HCS makes it hard to perform a direct comparison to other current sources. The comparison has been split between two categories of devices: those available as COTS and those only presented in the literature. The open source designs of the LCS and HCS means that they fall at the boundary between these two categories.

The LCS and HCS perform well in comparison to COTS low noise laboratory current sources. The most comparable example is the Twinleaf CSB [130] current source, which features 10 ppb noise at 10 mA at 1 Hz and about 1 ppb at 10 Hz. This device is however limited in terms of bandwidth, operating only up to a couple of Hz. Comparable performance could be achieved on the LCS by reconfiguring its filters to have a similar low frequency cut-off. Comparisons can also be made to more standard lab instruments such as the Keithley 6220 [131] (100 ppm noise at 2 mA in a 0.1 - 10 Hz bandwidth) or the Keysight B2962B [132] (10 ppm noise at 10 mA in a 0.1 - 10 Hz bandwidth). Both of these devices are noisier, limited to a maximum of two output channels (making them unsuitable for triaxial coil control) and are significantly more expensive.

Other current sources, with better noise performance or stability, are present in the literature but are not available commercially or are impractical to reproduce in a standard lab. The closest comparison is the junction-gate field-effect transistor (JFET) based current source by Scandurra et al [133]. Although it has superior noise performance (3 ppb/$\sqrt{\text{Hz}}$ at 1.8 mA at 1 Hz) the design is difficult to manufacture as it requires hand matching of components or the use of expensive and low availability parts. It also has a lower maximum output current and is only capable of a single DC output that requires tens of minutes to settle. Another example is the externally referenced current source by Fan et al [129]. Although the device features higher stability (1 ppb in 1000 seconds) but also slightly higher noise (36 ppb/$\sqrt{\text{Hz}}$ at 0.1 Hz), it has a single fixed DC output and the external reference is a Josephson voltage standard which requires cryogenic cooling.

4.5 High gain pre-amplifier design

The pre-amplifier was based on a design developed for measuring the noise contribution of an LTC6655 reference [134]. It was modified and modernised to replace the high gain stage that contained difficult to procure components, such as thermally-lagged JFET pairs and wet tantalum capacitors.

The simplified architecture of the pre-amplifier is presented in Fig. 4.9.

The design is centred around ADA4523-1 [135] (Analog Devices) chopper amplifiers, which form the gain stage. These exhibit very low noise at low frequencies. This is achieved by heterodyning 1/f noise on top of a chopping frequency of 330 kHz, which is located away from the 0.1 to 160 Hz bandwidth of interest. The signal first goes through an optional buffer that presents the load with a high

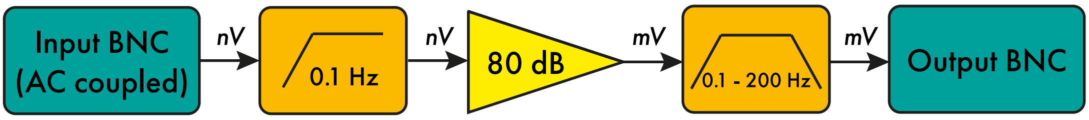

Figure 4.9 – Simplified architecture of the pre-amplifier. The input signal is buffered and stripped of its DC component with a 0.1 Hz HPF. It is then followed by an 80 dB gain block that is further filtered by a 0.1 - 200 Hz bandpass filter. The resulting signal is available on the output BNC for connection to an oscilloscope.

impedance input. The DC component is then removed using a hand-selected, sub 10 nA leakage current electrolytic capacitor to provide a HPF at 0.1 Hz. The HPF stage is very important, as one cannot rely on the oscilloscope AC-coupled input because of its high cut-off frequency ($>$ 10 Hz) which would obscure the 1/f noise contribution that needs to be measured. The gain stage consists of four ADA4523-1 amplifiers connected in parallel to reduce the voltage noise by a factor of 2 and provide a gain of 10000 (80 dB). The signal is later conditioned by a second-order Sallen-Key LPF with a Bessel response to reduce ringing at the output [136]. The final stage is a passive HPF to further improve the 0.1 Hz response. The device is interfaced with BNC connectors on each side and powered by two 6LR61 batteries. It provides a gain of 80 dB in a bandwidth of 0.1 - 200 Hz. Fig. 4.10 shows its bandwidth normalised to 0 dB. The pre-amplifier design is open source and available on GitHub [137].

4.6 Synopsis

This chapter described the design procedure and testing of two ultra-low noise current drivers. The LCS is capable of producing currents up to $\approx \pm$ 50 mA and the HCS is capable of providing $\approx \pm$ 250 mA. The devices complement each other by overlapping the gap between current ranges, allowing them to be used in a variety of applications. Both devices offer digital control of current on three independent axis with 16-bit resolution. They feature a common digital/signal

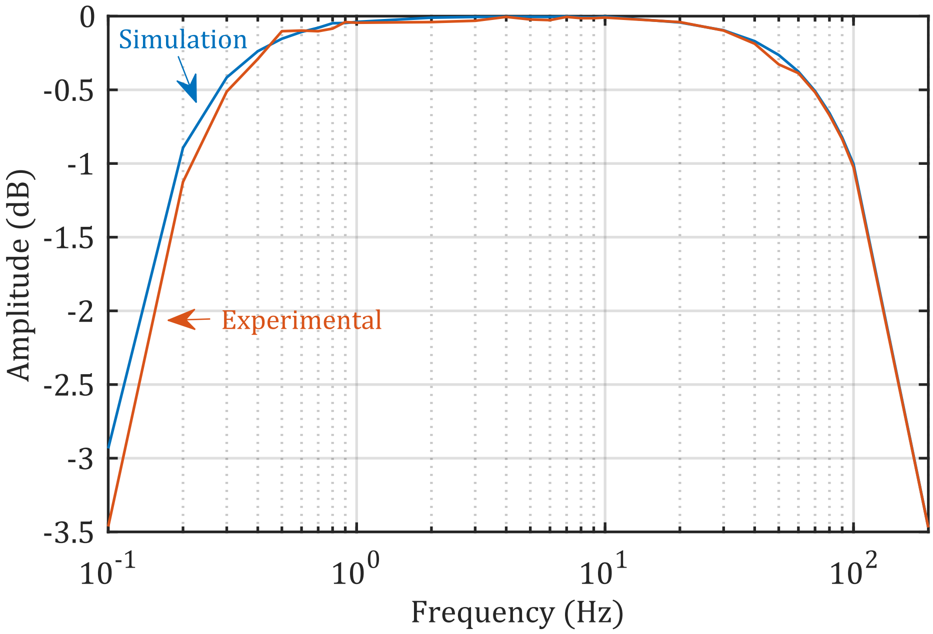

FIGURE 4.10 – Experimental (red) and simulated (blue), normalised (80 dB) pre-amplifier frequency response (0.1 - 200 Hz). The frequency response exhibits 50 mdB flatness. The simulated results match well with the experimental ones. The biggest difference being the corner frequency at the low end which is different due to the inherent tolerance of the electrolytic input capacitor. This however does not impact the overall bandwidth of the pre-amplifier.

conditioning chain allowing for user customisation in terms of bandwidth, noise or stability. This was demonstrated by changing the maximum output current capability which allowed the device to change its maximum output current while maintaining the dynamic range. When used to drive coils, having a selection of devices to choose from helps match the driver with a given coil geometry. An Arduino based firmware makes the device control extendable to non-expert users and allows users to extend the functionality to their particular application such as generation of arbitrary waveforms. In addition, both devices are fully open source, with documentation and design files being readily available on GitHub [107].

Noise tests showed that a 10 mA LCS achieved 146 pA/$\sqrt{\text{Hz}}$ at 10 Hz, demonstrating a relative noise of 15 ppb/$\sqrt{\text{Hz}}$. A 250 mA HCS achieved 4.1 nA/$\sqrt{\text{Hz}}$ at 10 Hz, demonstrating a relative noise of 16 ppb/$\sqrt{\text{Hz}}$. Both devices feature a narrow 1/f region with a corner frequency of approximately 1 Hz, making them well suited for precision magnetic field generation in OPMs.

The stability of both devices was found to be in the ppm range. Due to the fact that the only difference between LCS and HCS is their output stage, the stability performance is very similar. This performance is more than enough for coil control in most OPM applications which primarily rely on short term stability.

Accuracy tests showed that the device does not have to be calibrated to achieve satisfactory performance, presenting an out of the box solution. For applications demanding very high accuracy it was shown that calibration is possible, unlocking the full potential of the device with monotonic accuracy of $\pm$ 1 LSB over its full range.

Both LCS and HCS devices are now widely utilised as high performance current sources in the magnetometry group for all experiments including SERF experiments, RF magnetometers and FID magnetometers.

Chapter 5

Optoelectronics

This chapter focuses on the development and testing of optoelectronics designed for the SERF experiments covered in Chapter 3. This includes custom low-noise amplified photodetectors, that specifically target SERF bandwidth of interest. It also includes a custom laser driver used to drive VCSELs which offers lower relative intensity noise (RIN) than the DBR laser source currently used in the portable SERF experiment.

5.1 Photodetector design

This section covers the development and testing of the custom photodetectors used for the SERF magnetometers covered in Chapter 3.

5.1.1 Design requirement

Photodetection plays a paramount role in any optical experiment where light is to be monitored. This is no different for the SERF experiments conducted in this thesis. The only difference being, specific requirements that are unique to SERF magnetometers.

Photodetectors can be classified into two different categories: un-amplified and amplified. Un-amplified (otherwise known as biased photodetectors) are simple photodiodes configured in a reverse bias configuration typically provided by a battery. Reverse bias is used to decrease the capacitance of the diode allowing it to be used for high-speed applications in a range of 10 MHz to 5 GHz. It also provides a linear photo-current response with incident light intensity. The current-voltage curve of a photodiode operated in different modes is presented in Fig. 5.1. In the work described in this thesis, the photovoltaic mode was not used due to its non-linearity and low dynamic range.

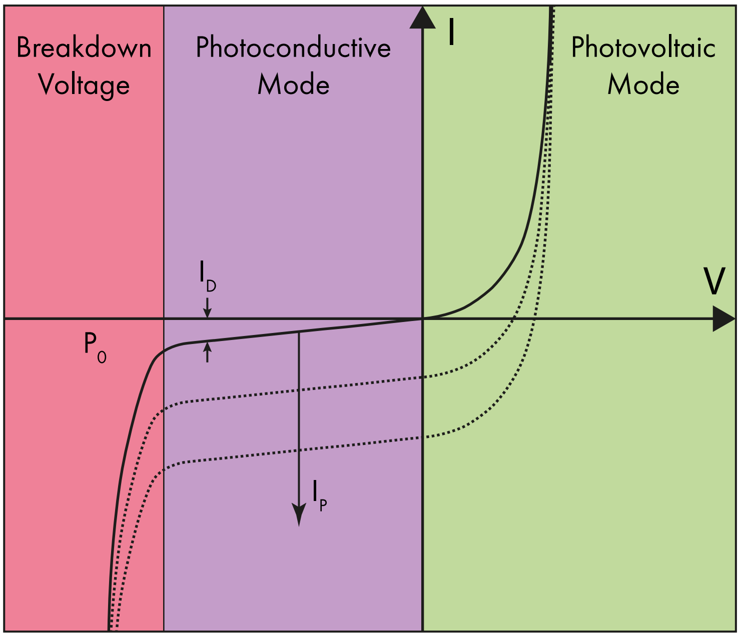

FIGURE 5.1 – Diagram presenting IV curve of a typical photodiode.

One of the downsides of using photoconductive mode is the introduction of dark current. A dark current is a form of a leakage current present when no light is incident on the photodiode. It increases as a function of reverse bias voltage. Dark current has a white noise characteristic and is similar in nature to shot noise [138]. It is given as noise spectral density and is presented in Eq. 5.1 where q is the charge of the electron, and I_d is the dark current.

$$\sigma_\mathrm{d} = \sqrt{2qI_\mathrm{d}}\ . \tag{5.1}$$

In the high-sensitivity application dark current needs to be taken into account as it will directly affect the sensitivity of the device.

The other form of detectors mentioned previously are the amplified photodetectors, which are self-contained biased photodetectors that also feature a TIA. This form of a detector is of interest to us, as it ensures that the low current signal $\approx$ nA to μA is amplified as close to the photodiode as possible, to prevent distortion caused by external leakage currents. Having a built-in TIA also offers convenience, presenting a sampling system with an easy to read voltage signal. This is especially true if the gain can be adjusted to suit the experiment's needs.

The photodetector for SERF application does not require high bandwidth, as found in typical photodetectors. The SERF magnetometer bandwidth is determined by the gyromagnetic ratio of the alkali species used and its relaxation time [21, 139] and is typically quite small in the order of 10 - 500 Hz [13] where no additional modulation bandwidth enhancing techniques are used, which would enable operation up to 10 kHz [140]. The expected bandwidth of the magnetometers described here would not exceed 300 Hz for Rb and 1000 Hz for Cs experiments. Although the bandwidth needed is small, it is crucial that the noise contribution over that bandwidth is as small as possible.

Typical photodetector amplifiers offer very low input bias currents so as to not obscure the signal. These devices typically use CMOS architectures providing typical bias currents in the range of fA - nA. The wideband noise contribution is typically low making it ideally suited for high-speed ($>$ 1 MHz) applications. These devices however are more affected by the flicker noise (1/f noise) which compromises their low-frequency noise, below $\approx$ 1 kHz [120]. Due to this reason, commercial photodetectors are not optimal for this task as they typically target a different bandwidth of interest. Because of this, it was decided that a custom photodetector would be designed specifically for SERF magnetometers, that would target its operational bandwidth as a low-noise region.

The photodetector to be designed should also be ideally small and have the ability to accept standard-size optics. The size here is not crucial, however, having a similar form factor to commercially available detectors is desired to prevent bulky designs from occupying optical table real estate. Having the ability to accept optics is also important as it eases the alignment process and increases the versatility of the device.

5.1.2 Design

The first step in the design of the photodetector was to figure out the form factor used. It was decided to house the layout on a stacked 1″ diameter circular PCB. Using circular PCBs allows for mounting the whole device in a standard lens mount that can be fitted into cage mounts. This also allows for the active area of the photodetector to be concentric on the optics preventing miss alignment. A photograph of completed photodetectors fitted into lens mounts is provided in Fig. 5.2.

Figure 5.2 – Photograph of the photodetector fitted in a lens mount. The picture on the left shows the front side of the photodetector featuring TIA, gain switching and BPW 34 photodiode. The picture in the middle shows the back of the photodetector featuring the power supply board and signal output SMA. The right picture shows the photodetector fitted with a focusing lens.

The main component of the photodetector is its photodiode. The photodiode has to feature a good response in the wavelength of interest (795 nm | 895 nm), offering a sufficient active area for ease of alignment while at the same time not increasing its dark current. The photodiode selected was BPW 34 S [141]. It is a surface-mounted silicon PIN photodiode with a square radiant sensitive area with 2.65 mm side. PIN photodiodes feature an intrinsic region which increases the quantum efficiency of the detector and by that, spectral sensitivity [138, 142]. It features a responsivity of 0.6 A/W at a wavelength of 795 nm. The photodiode was selected to be in a surface mount package as it helps to reduce the footprint size and is a better fit for the circular PCB. The device also features very low noise-equivalent-power (NEP) of 41 fW/$\sqrt{\text{Hz}}$. NEP is a figure of merit for the photodetectors that defines the minimum optical power required to equalise signal-to-noise ratio (SNR) [138].

As the photodetector needs to target low frequencies (DC - 300 Hz) it was decided to base the amplifier on a field-effect transistor (FET) input architecture. FET architectures can simultaneously provide low input bias current, as well as narrow 1/f noise. The amplifier that was selected to act as a TIA was ADA4625 [143]. ADA4625 op-amp offers very low voltage noise of 3.3 nV after 100 Hz (5.5 nV at 10 Hz) and 4.5 fA of current noise at the same frequency. In transimpedance applications, where the source features high resistance (such as a photodiode), the input current noise must be as small as possible, as it will directly contribute to the output noise. The device also features low voltage noise of 150 nV RMS in its 1/f frequency band (0.1 to 10 Hz), providing a flatter noise contribution in the magnetometer bandwidth of interest.

The basic TIA architecture for photodiodes is presented in Fig. 5.3. For the design of the custom photodetector, it was decided that the circuit will feature selectable gain control with three settings. This was done so that the photodetector operation can be tuned during the optimisation of the magnetometer which involves changing laser light power and density of the atomic vapour through heating the cell. A schematic diagram of the completed photodetector architecture is presented in Fig. 5.4.

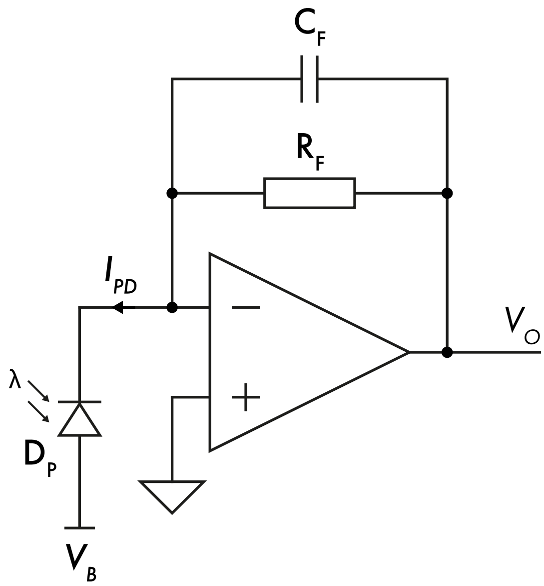

FIGURE 5.3 – Diagram presenting typical TIA configuration used for biased photodiodes. The photodiode D_P is reverse biased by negative supply voltage V_B, so it operates in the photoconductance mode. Photocurrent I_PD is amplified by the amplifier in transimpedance configuration as a product of feedback resistor R_F as $-R_\mathrm{F} I_\mathrm{PD} = V_\mathrm{O}$. Capacitor C_F is used to compensate for the zero generated by the capacitance of the photodiode D_P, as well as setting the bandwidth of the detector circuit. The roll-off frequency is defined as $f_\mathrm{c} = 1/(2\pi R_\mathrm{F} C_\mathrm{F})$.

The design is centred around ADA4625 op-amp (U_1), configured in the transimpedance configuration described in Fig. 5.3. The photodetector features a selection of three gain settings defined by R_x and C_x pairs where x is the number of pairs corresponding to a gain setting. A double-throw triple pole switch (CL-SB-23B-02T) was used to change between different amplifier gains. A dual throw switch allows for a Kelvin configuration to be utilised, removing the resistance switch as a source of gain error, as well as fully isolating switching stages [144]. The on resistance of mechanical switches is typically small so the resistance gain penalty would have been negligible. The switch was primarily selected for its size, as the single slide switch mechanism is smaller than individual switches that would simply not fit on the board. As one of the switches would remain otherwise unused it was decided to connect it in a Kelvin configuration.

Initially, the device was configured to provide gains of 10, 20 and 40.2 kV/A, featuring a -3 dB bandwidth of 8 kHz ($<$ 80 mdB attenuation to 1 kHz) on all ranges. After the magnetometer optimisation process, it was found that higher laser powers are preferred and the programmable gains were changed to 2, 5 and 10 kV/A with the same bandwidth. The resistors used for gain setting each featured a tolerance of 0.1 % and a low-temperature coefficient of 25 ppm/°C to ensure gain accuracy.

It was also decided to include control of the photodiode reverse bias voltage V_{B} for optimisation of the dark current and linear operating region. The control of V_{B} was achieved through the use of a miniature, single turn 10 kΩ trimming-potentiometer (TC33 series) RV_1.

An optional resistor capacitor (RC) LPF was included at the output of the amplifier, to increase the filter response and aid the compensation capacitor. LPF components footprints have been provided on the PCB, but are not normally populated and the resistor R_4 is bridged with a solder link or 0 Ω resistor. This functionality was not used in this experiment.

As the design aims for low-noise operation, its power delivery requires consideration. The device requires a split rail supply of minimum ± 10.1 V to be able to operate over the full dynamic range of the NI PCIe-6353, which features a ± 10 V range. The power could have been simply provided from a low-noise power supply unit set to the required voltage. However, it was decided to provide voltage regulation on the device, which would make it compatible with more generic power supplies and supplies already used for powering photodetectors. For the voltage regulators LT3042 [145] and LT3093 [146] complementary pair LDO regulators were selected. These regulators feature extremely low noise contribution of 0.8 μV and ultrahigh power supply rejection ratio (PSRR) of 110 dB in the bandwidth of interest which

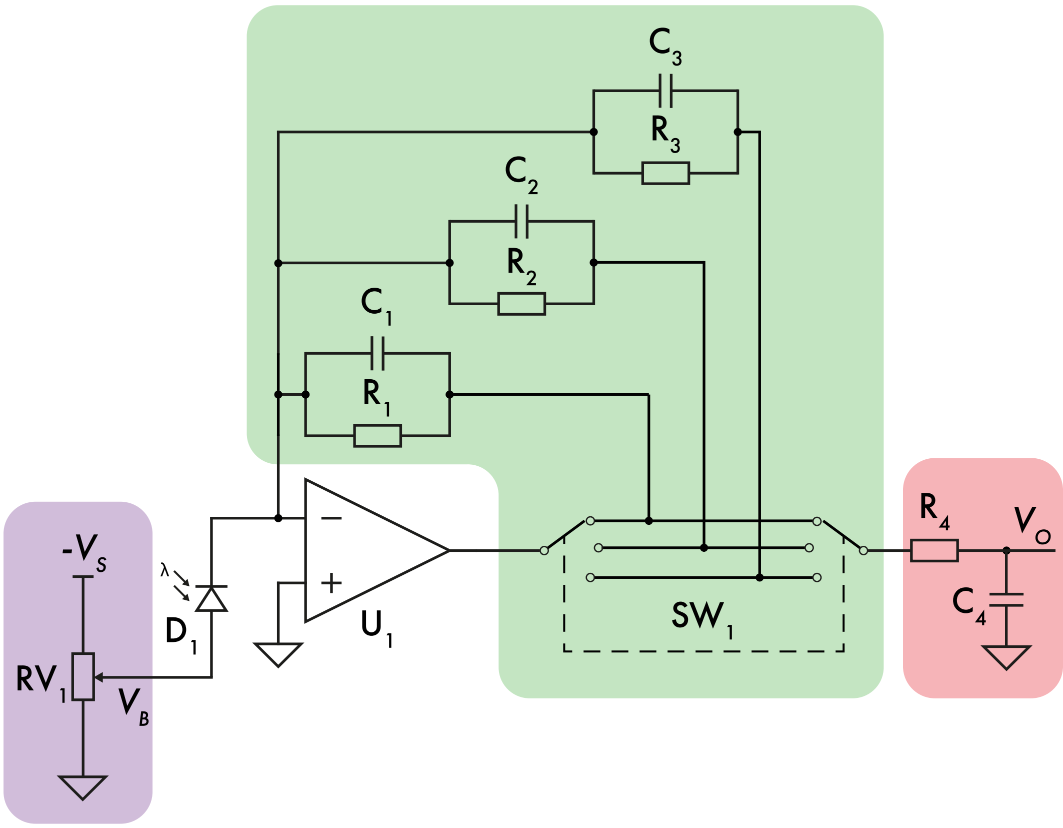

Figure 5.4 – Schematic diagram of the custom photodetector with different sections of the circuit highlighted. Voltage bias adjustment in purple, gain selection in green and optional LPF in red.

drops to 80 dB at 1 MHz. The ability to maintain PSRR at such high frequencies allows it to be used with lower quality power supplies, such as switched-mode power supplies. The regulators were set to provide ± 11 V to ensure that the full dynamic range of the DAQ system can be utilised.

The design was split into two, 1″, circular boards. The front board houses the photodetector circuitry presented in Fig. 5.4 while the other board houses the power supply regulation circuitry. The boards are interconnected through 1 mm pitch headers and receptacles allowing for quick replacement of the modules, or swapping photodiodes used. The boards are also secured with two M2 brass spacers that maintain the alignment between boards. Photographs of unpopulated PCBs, as well as the photodetector assembly, can be seen in Fig. 5.5.

The power is supplied through a keyed connector featuring a 2 mm pitch (Molex

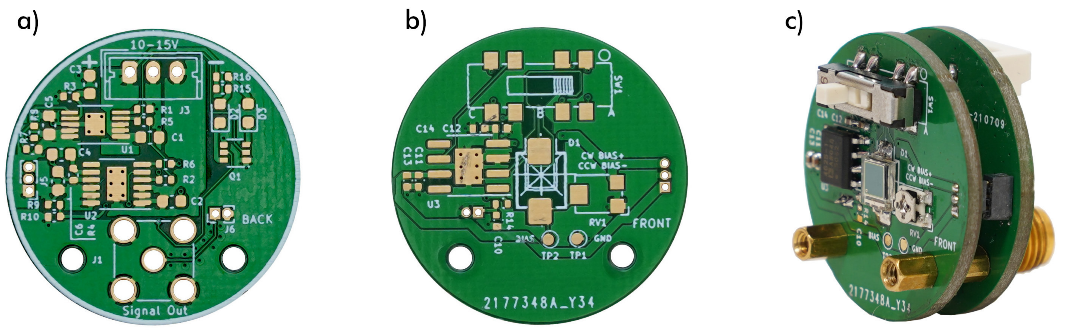

FIGURE 5.5 – Photograph of the photodetector PCBs and assembled photodetector module. Picture (a) shows the power supply PCB, picture (b) shows the photodetector PCB accepting BPW 34 photodiodes, and picture (c) shows the photodetector assembly.

53253-0370). Custom cables made out of shielded twisted pair (VD 268-100-000) were used to carry power to the detector from the power supply. Each board was built with 0402 and 0603 size passive components in order to fit everything on the board.

Photodetector PCBs were also made to house a range of different photodiodes (SFH 2700, SFH 2400 and BP 104) each offering different sizes of the active area, to tailor diode capacitance and NEP performance to the application of interest. Because the design is split into a photodetector PCB and a power regulation PCB, the photodetector board can feature different gain and bandwidth settings as well as different photodiodes, which are user replaceable. These photodetectors are used in other magnetometry experiments in our group, due to their versatility in bandwidth and gain selection and ability to accept different photodiodes. The portable SERF magnetometer described in Chapter 3, utilises the TIA architecture presented in Fig. 5.3. This TIA was placed outside of the magnetometer sensor head to limit the magnetic contribution, with only the photodiode being present inside.

5.1.3 Testing

After the device was assembled it was important to gauge its noise contribution and noise shape. A typical rule of thumb for detection systems in optical experiments is that the detector should feature about an order of magnitude lower noise than the sampling DAQ system.

To measure the noise of the detector a similar setup to the coil driver noise measurement was used. The setup is presented in Fig. 5.6. The oscilloscope was set to sample at a rate of 100 kS/s for 100 seconds in order to accurately estimate the low frequency (0.1 Hz) component.

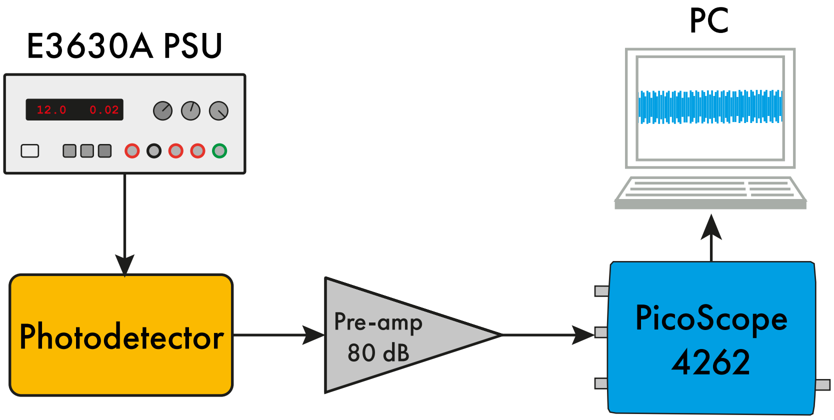

Figure 5.6 – Diagram of photodetector test setup. The photodetector is powered by a low noise power supply (Keysight E3630A), which provides ± 12 V to the detector. The output from the photodetector is pre-amplified with a custom voltage probe featuring a high gain of 10000 (80 dB) in the bandwidth of 0.1 - 200 Hz. The pre-amplified signal is then digitised by a 16-bit vertical resolution oscilloscope (PicoScope 4262).

Photodiodes feature three different input current noise mechanisms which are, thermal noise (σ_{th}), photon shot noise (σ_{sh}) and dark current noise (σ_{d}). Thermal noise is a product of the shunt resistance of the diode and is given in Eq. 5.2, where R_{sh} is the shunt resistance. The value of input referred thermal noise is small for amplified photodetectors, as the shunt resistance is typically large (in the order of GΩs). The BPW 34 photodetector features a typical R_{sh} of 5 GΩ at a reverse bias voltage of 10. This yields a typical noise current of only $\approx$ 1.8 fA/$\sqrt{\text{Hz}}$ at room temperature.

$$\sigma_{\mathrm{th}} = \sqrt{\frac{4k_B T}{R_{\mathrm{sh}}}} \ . \tag{5.2}$$

Another noise mechanism is the photon shot noise, which is based on the number of photons being incident on the photodetector. This noise originates from the fact that the incident photons are not synchronised in reaching the detector. This presents a statistical distribution of the number of incident photons on the detector. This process is described in Eq. 5.3 where I_{p} is the photocurrent, which is the result of a product of incident optical power P_{o} and photodiode responsivity $\mathcal{R}$. It is important to note that a Gaussian distribution has been used to estimate the photon shot noise, however, the Poisson distribution provides a better statistical approximation for very low optical powers [138]. Gaussian distribution was used as it provides a simpler noise analysis and is valid for typical optical powers used in the experiment. The photon shot noise estimation is performed in Section 3.3. In an ideal scenario, the magnetometer sensitivity should be photon shot noise limited.

$$\sigma_{\mathrm{sh}} = \sqrt{2qI_{\mathrm{p}}} \ . \tag{5.3}$$

The previously mentioned dark current is present in all photodiodes that are operating in photoconductive mode. It manifests as a form of a leakage current and offsets the output signal of the detector and features the same noise mechanism as the photon shot noise as seen in Eq. 5.1. This noise is dependent on temperature and the bias voltage applied to the photodiode. The dark current of BPW 34 diode at room temperature and 10 V reverse bias voltage equal to 2 nA and yield a typical noise of ≈ 25.3 fA/$\sqrt{\mathrm{Hz}}$.

These noise sources all add in quadrature to produce total photodiode input current noise i_{npd} given as $i_{\text{npd}} = \sqrt{\sigma_{\text{th}}^2 + \sigma_{\text{sh}}^2 + \sigma_{\text{d}}^2}$. The amplifier input current i_{na} noise also adds to the noise perceived at the input where the total input noise current is given as $i_{\text{ni}} = \sqrt{i_{\text{npd}}^2 + i_{\text{na}}^2}$

The transimpedance amplifier is used to amplify input current and output it as voltage. The total voltage output noise of the TIA is a quadrature sum of a product of transimpedance gain with the input noise current $e_{\text{nTIA}} = i_{\text{ni}} R_{\text{F}}$, Johnson noise of the feedback resistor $e_{\text{th}} = \sqrt{4k_B R_{\text{F}}}$ and finally the input spot noise of the amplifier e_{na}. The total output voltage noise is thus $e_{no} = \sqrt{e_{\text{nTIA}}^2 + e_{\text{th}}^2 + e_{\text{na}}^2}$.

The photodetector was configured to provide three transimpedance gains of 5, 10, and 150 kV/A with a bandwidth of 8 kHz. The gains of 5 and 10 kV/A represent typical gains used in the Rb, lab-based experiment, while 150 kV/A gain was used as a form of a stress test for looking at the low optical power operation of the device.

The noise density of the photodetector at different gains and 10 V bias is presented in Fig. 5.7. The noise performance and shape present a good match with the calculation.

The calculated values for total noise are in close agreement with the experimental results as seen in Tab. 5.1.

Table 5.1 – Comparison of calculation and experimental NSD results of the photodetector at different transimpedance gains, evaluated at 100 Hz where the amplifier noise response flattens.

Gain (kV/A)	**NSD Calculation (100 Hz)**	**NSD Experimental (100 Hz)**
5	9.7 nV/$\sqrt{\text{Hz}}$	9.8 nV/$\sqrt{\text{Hz}}$
10	13.2 nV/$\sqrt{\text{Hz}}$	13.4 nV/$\sqrt{\text{Hz}}$
150	49.6 nV/$\sqrt{\text{Hz}}$	51.2 nV/$\sqrt{\text{Hz}}$

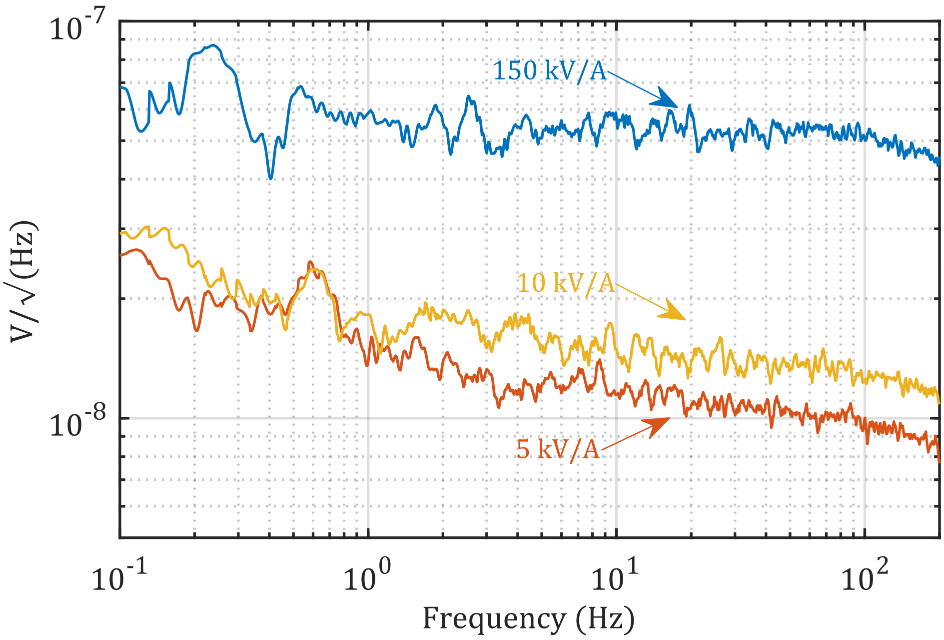

FIGURE 5.7 – NSD results of the photodetector at different gains with 10 V reverse bias voltage. Gain of 5 kV/A (red), 10 kV/A (gold) and 150 kV/A (blue). The NSD was obtained using a LPSD [87] algorithm made out of 1024 FFT points using a Hann window with the amplitude scaling correction applied.

The spot noise at 100 Hz is valid for the remaining bandwidth of the magnetometer after 100 Hz as the location of the zero $\mathcal{Z}$ is present at a much higher frequency ($\approx$ 30 kHz for a gain of 150 kV/A and $\approx$ 912 kHz at gain of 5 kV/A) than the bandwidth of the photodetector. The frequency of the $\mathcal{Z}$ is obtained from $f_{\mathcal{Z}} = 1/(2\pi R_{\mathrm{F}} C_{\mathrm{in}})$ where C_{in} is the total input capacitance (sum of photodiode capacitance and amplifier input capacitance).

The impact of the dark current was tested by fixing the gain and setting the reverse bias voltage to 0 V, 5 V and 10 V respectively. No difference in the output voltage noise was found, as even for a gain of 150 kV/A the contribution is only 3.8 nV/$\sqrt{\text{Hz}}$ (by taking only the dark current noise and multiplying it by the transimpedance gain) of additional output voltage noise between V_{B} = -10 V and V_{B} = 0 V. The NSDs at different reverse bias voltages are presented in Fig. 5.8.

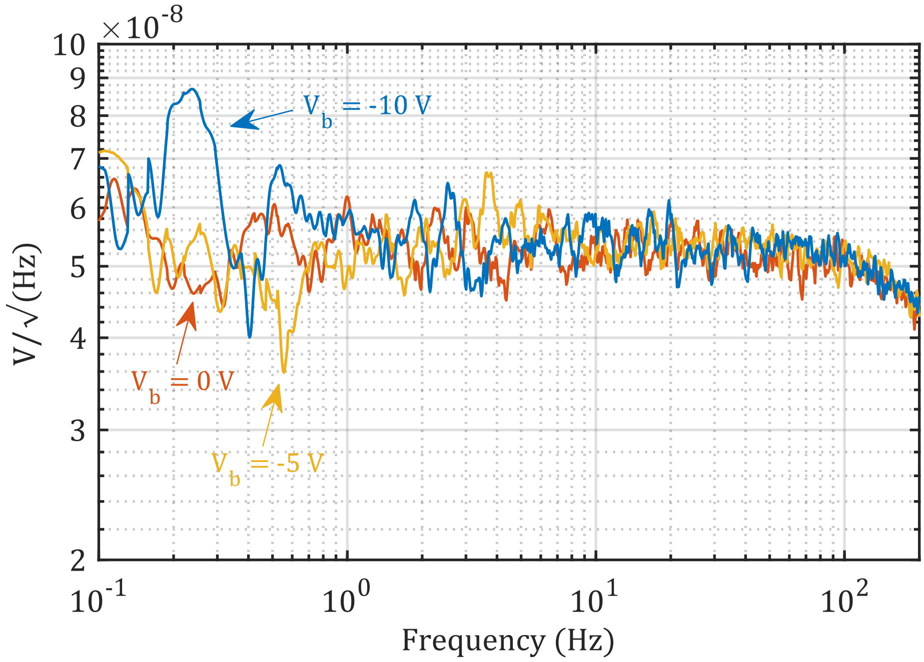

Figure 5.8 – NSD results of the photodetector at a fixed gain of 150 kV/A with 10 V, 5 V and 0 V reverse bias voltages. V_B = 0 (red), V_B = -5 (gold) and V_B = -10 (blue). The NSD was obtained using a LPSD [87] algorithm made out of 1024 FFT points using a Hann window with the amplitude scaling correction applied.

5.2 VCSEL Driver design

One of the main aspects of portable systems is the minimisation of SWaP. One way to achieve this in the case of a portable magnetometer, is to replace the currently used DBR laser source with the VCSEL. VCSELs are characterised by their exceptionally low threshold current and high efficiency. In addition, these devices can be manufactured to have a single transverse mode and produce narrow enough linewidth to resolve the hyperfine structure of the D_1 line of Cs atoms and maintain stable linear polarisation. All of this can be achieved at lower cost and volume than DBR fiber based systems, making VCSELs potentially attractive in replacement of DBR lasers for portable magnetometer systems. Commercial devices based around this laser technology have been successfully used in biomedical applications [31, 147]. An annotated photograph of a VCSEL diode used in this project is presented in Fig. 5.9.

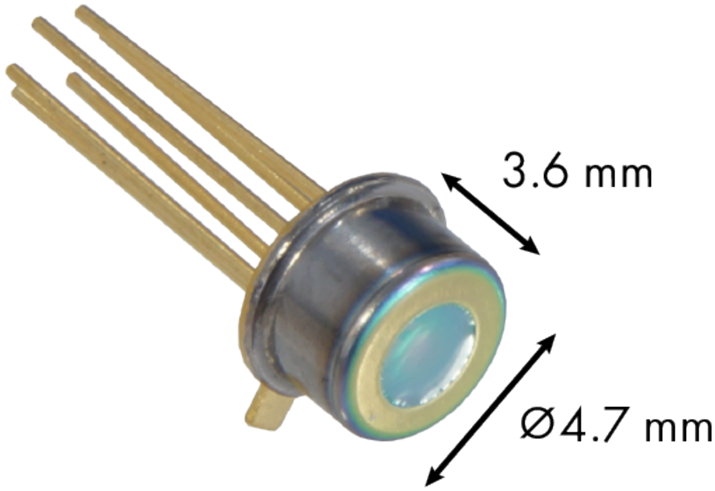

Figure 5.9 – Photograph of 895 nm VCSEL (Vixar) in a TO-46 package with an integrated thermistor and TEC. Dimensions added for the metal can housing the VCSEL.

5.2.1 Design requirements

The VCSELs used for atomic magnetometry requires a stable, low noise current source to limit the intensity noise induced into the experiment. For SERF magnetometers this implies very low current noise, on the order of pA/$\sqrt{\text{Hz}}$ with as narrow 1/f contribution as possible so as to not limit sensor sensitivity. As VCSELs have very small threshold currents (on the order of 100s of μA), their optical power slope efficiency is high in comparison to DBR devices making them particularly sensitive to current changes. The VCSELs maximum power output is achieved at modest currents, on the order of few mA, which is related to the cavity size. The cavity size in turn affects the frequency tuning rate with respect to the input current. The VCSEL devices have a typical current tuning of 0.5 nm/mA [148], comparing that to the DBR laser that is currently used in the experiment [94] yields only 0.002 nm/mA which corresponds to about 250 times lower tuning coefficient than the VCSEL. A higher frequency tuning coefficient presents not only a requirement for low noise but also high stability and low drift of the driver.

Another important factor is the temperature control of the VCSEL, which affects the length of the cavity in turn changes lasing frequency. For the VCSEL this temperature tuning coefficient has a typical value of 0.06 nm/K. For buffer gas broadened cell the temperature of the VCSEL has to be stable to at least 10 mK so that it interacts with the correct hyperfine transition and does not leave resonance when the measurements are taking place [149]. VCSEL temperature can be controlled with a dedicated mount with a TEC and a thermistor to form a feedback loop. This approach is however too bulky and magnetic for integration into portable system sensor heads. For this reason, VCSELs often have an integrated thermistor and a TEC. This approach allows for reduced SWaP in the overall system as well as reduces time constant related to thermally stabilising the device. One of the challenges with VCSELs is that they are often operated at higher temperatures (40 - 90 °C) in comparison to DBR lasers which are made to be tuned between 15 - 35 °C. The higher operating temperature presents a problem for stable operation as the thermistors used in these devices have a non-linear relation between resistance and temperature. The relationship approaches an asymptote at temperatures higher than 40 °C as seen in Fig. 5.10. A 1 mK change at 25 °C corresponds to a change of 444 mΩ. The same change at 65 °C will correspond to a change of only 72 mΩ, over 6 times lower response for the same change in temperature. The move to higher temperature requires increased precision and a lower noise floor on the temperature feedback loop.

As the experiments would typically be run over minutes to an hour, long term stability is not crucial. However, the ability to maintain stability is targeted as it presents a solution that does not require laser locking for our system. In the instance that locking would be used, less corrective action would be required to maintain stability. Fewer and smaller servo operations thus translated to less servo noise injected into the system.

Typically the operational frequency of the laser used for magnetometry is not

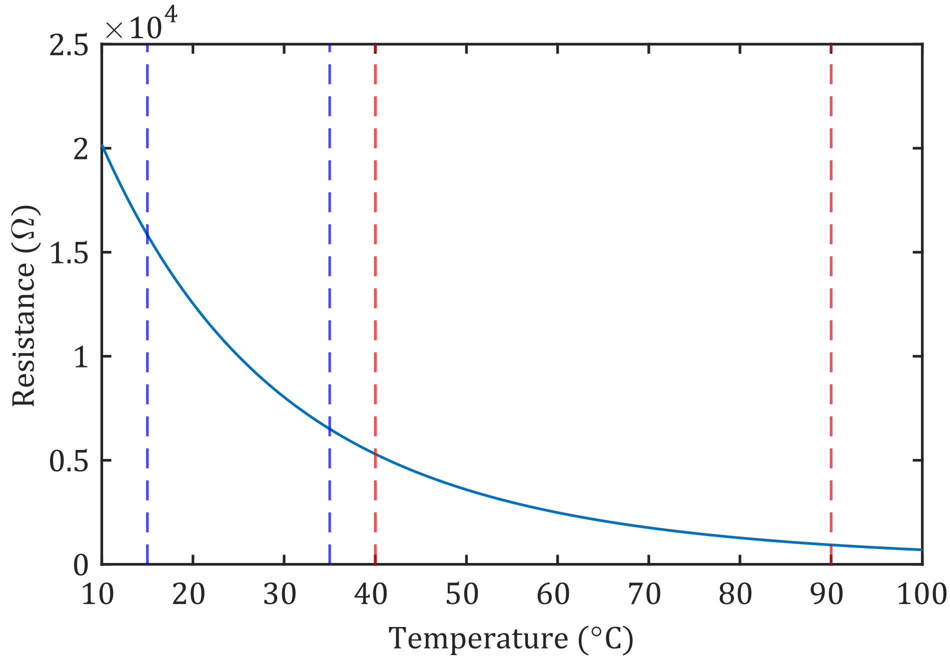

Figure 5.10 – Thermistor ($\beta = 3973$) response against temperature. Blue lines represent the typical DBR tuning range while red lines represent the VCSEL tuning range.

a single value, requiring detuning from resonance. In the case of the Cs setup discussed previously the resonant frequency is $F = 4 \longrightarrow F' = 3$ transition on the Cs D_1 line. For optimisation of the magnetometer, this value is detuned as far as ± 30 GHz which translates to about ± 1.33 °C. This presents a requirement for an ability to change VCSEL frequency by means of current or temperature change during the device operation rather than finding resonant frequency on a device basis and leaving it static. This presents a requirement of software tunability, where the laser frequency can be detuned using the scanning technique described earlier in Section 3.1. The software control additionally allows for locking the laser to a particular transition if such a need would emerge.

Maintaining the low SWaP is important for the portable magnetometer system (sensor head and control electronics). For this reason, the laser driver should ideally be no larger than the coil driver described in the earlier Chapter 4. Reducing the SWaP of the system allows for better portability and aids use in biomedical applications, where the whole system can be easily transported from the lab to, for example, an MSR.

Currently, most of the laser driver systems that can be purchased are lab-based instrumentation that do not target the low current and exceptional low noise required by the VCSELs. There are some original equipment manufacturer (OEM) "portable" solutions but they do not meet the performance requirements outlined here. This thus presents a need for a custom solution targeting high-performance VCSEL applications, such as optically pumped magnetometry.

5.2.2 System design

The simplified system diagram is presented in Fig. 5.11. The design comprises three main sections: interface and digital control, TEC temperature controller, and a laser current source. Each of these systems can be broken down into its own subsystems such as analogue signal conditioning, voltage reference, analogue to digital converter (ADC) and DAC data converters.

5.2.2.1 Current source

The constant current source is one of the main aspects of the VCSEL driver. From the requirements gathered, it is not only supposed to feature ultra-low noise but also a high level of stability. Initially, it was thought that a design based around LT3092 (Analog Devices) [150] current source would be sufficient. A simplified schematic, showing LT3092 architecture is presented in Fig. 5.12. LT3092 is an integrated circuit that uses an internal current source that acts as a reference, followed by an error amplifier driving a Sziklai pair. The current is programmed with two resistors; one determines the voltage presented to the non-inverting input of the error amplifier while the error signal is obtained from the voltage dropped over the feedback resistor. This integrated circuit (IC) can source up to 200 mA of current and features good voltage compliance due to its use of a Sziklai

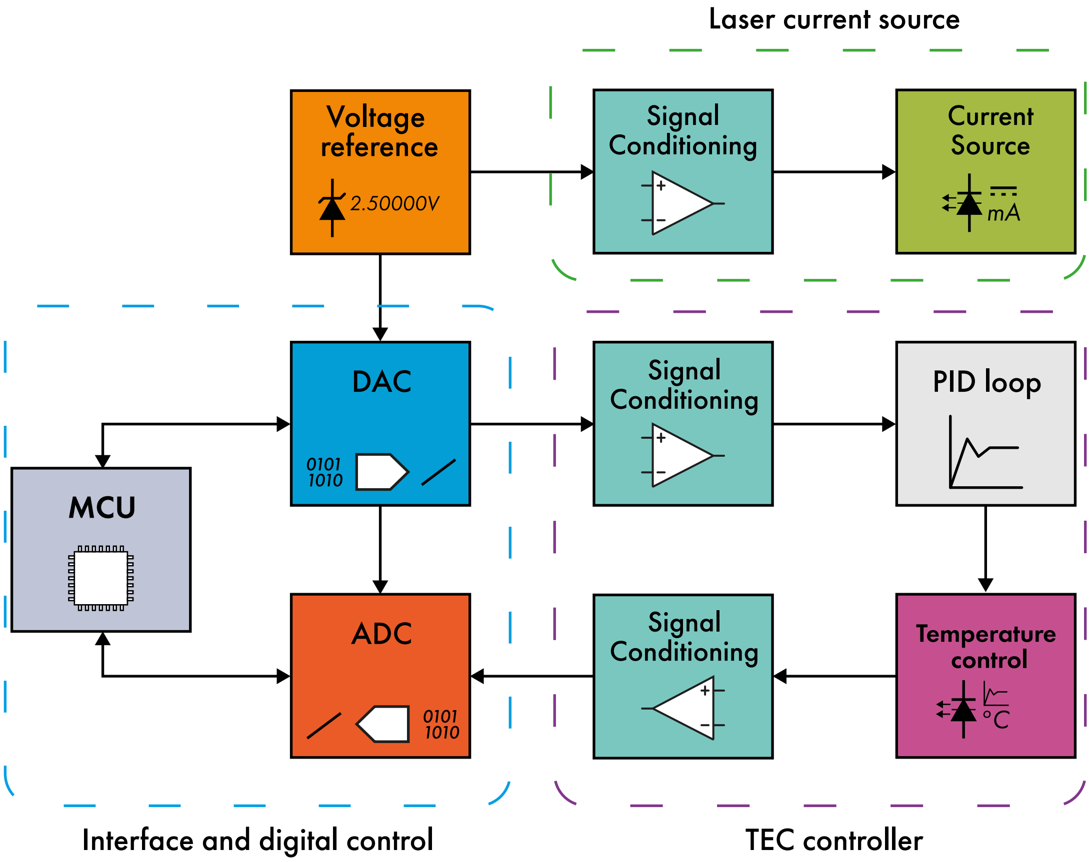

FIGURE 5.11 – Simplified VCSEL driver system diagram. The design can be split into three main sections. Digital control, TEC temperature controller; and constant current source. The last two are split into subsections covering analogue signal conditioning, voltage reference and ADC/DAC chains.

pair as a driving stage. There is however a problem with the noise of the circuit. The datasheet does not present output noise but rather the noise of the internal current reference which is very low 2.7 pA/$\sqrt{\text{Hz}}$ from 10 Hz. However, the output noise of the device was found to be $\approx$ 800 pA/$\sqrt{\text{Hz}}$ while delivering 2 mA. This result was obtained by shunting the set resistor with a capacitor to lower its noise contribution. The noise origin is most likely related to the error amplifier and to a lesser extent the driving stage. The performance of the LT3092 was good enough for general use, however considering the output noise performance of the coil driver covered previously in Chapter 4, which is not only a much more complex device but also requires a bi-polar operation, its noise performance was found to be $\approx$ 60 pA/$\sqrt{\text{Hz}}$ at 10 Hz, about 10 times less than a non-adjustable current

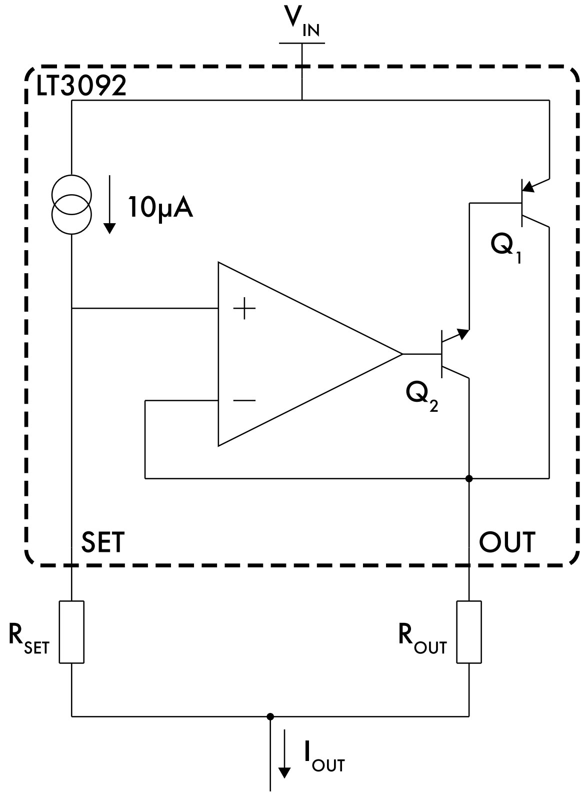

Figure 5.12 – LT3092 internal simplified schematic (inside dashed line) and mandatory, external components R_{SET} and R_{OUT}.

source proposed. An obvious solution would be to use the previously designed coil driver and use it to drive the VCSELs, but the requirements that both designs target are different. The VCSELs will be operated at a single current and if the operational current would need to be changed, it can be done by swapping passive components. The noise performance of the VCSEL driver should be in the ballpark of the coil driver and ideally offer lower noise to limit the impact of the intensity noise of the laser.

The custom low noise current sources designed in Chapter 4, could have been used to drive VCSELs, but it was decided that the VCSEL driver combining both temperature control and current control would have been a better fit for other magnetometry applications (portable total field sensors) which do not require field nulling capability. By combining current and temperature control into a single device, these applications benefit from reduced SWaP. Additionally, it was believed that a fixed current source would present lower noise and greater stability than the coil drivers. The LCS architecture was thus revisited in pursuit of lower noise.

The VCSELs used in this project have all been Vixar VCSELs which have an integrated TEC and thermistor. This presents one other requirement which is that the current source needs to be cathode grounded. This stems from the fact that one side of the thermistor is tied to the cathode of the laser diode, which either requires differential sensing or grounding the cathode. Cathode-grounded laser current sources are more difficult to design, as any form of sense has to happen before the diode. LT3092 current source is one such source which can drive grounded loads. Another architecture that can do that is the previously discussed Howland current pump that was used to make the coil driver.

This current source comprises a voltage reference, four resistors and an operational amplifier. Traditional HCP works very well in an application that does not require much compliance voltage, such as a coil driver that drives a relatively low resistance load. VCSELs used in the experiment, have a typical forward voltage drop of ≤ 2.5 V which becomes problematic for HCP circuits which pay a penalty of having a compliance voltage ≤ 50 % of the supply voltage. In this instance, improved Howland current pump (IHCP) works better as the current is controlled with a single resistor while the rest set the compliance voltage. This approach allows tailoring the compliance voltage while increasing efficiency. The penalty paid here is the increased output noise, however, it can be dealt with by filtering at the cost of the response speed.

An IHCP similarly to a HCP is made out of four closely matched resistors around its inverting and non-inverting inputs. The main difference stems from the output node between the two circuits with HCP having its output node V_x present at the non-inverting input to the amplifier as seen in Fig. 5.13 a) while IHCP uses the R_5, present on the output of the amplifier. The resistor moves the device output node

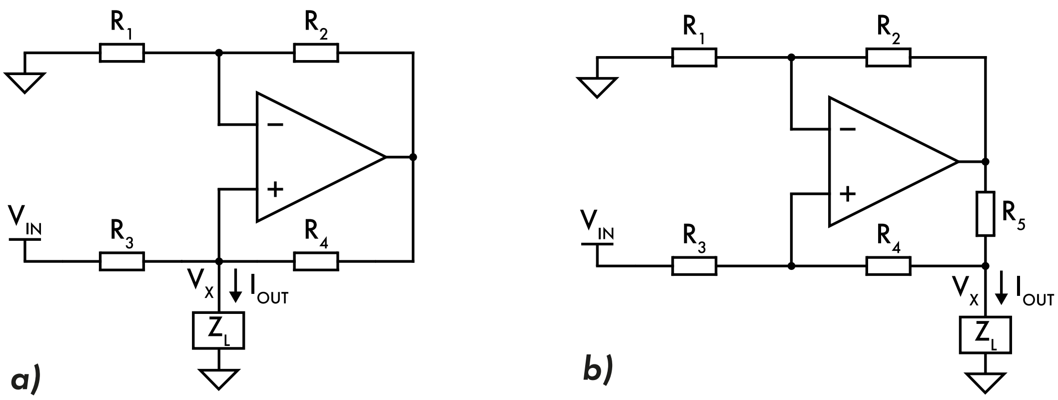

Figure 5.13 – Schematic of the "standard" Howland current pump and "improved" Howland current pump with a single amplifier. The "standard" version presented in a), is made out of four well matched resistors that form a ratio such that $R_1/R_2 = R_3/R_4$ to obtain maximum common-mode rejection ratio (CMRR). The output current is derived at the non-inverting node of the amplifier, V_x. The "improved" version based on a single amplifier is presented in b), and is almost identical to a); however, the output current is derived after the resistor R_5. An output error is introduced due to the finite resistance of the feedback resistors R_3 and R_4 introducing extra current summed at the output node V_x.

V_x after that resistor as seen in Fig. 5.13 b). It can be seen that at V_x feedback current going to the $R_3 + R_4$ resistors will be combined with the current flowing through the R_5 shunt resistor affecting the output current. This can be mitigated by using high value resistors that form the R_1, R_2, R_3, R_4 combo. This however would drastically increase the thermal noise present in the device. A simpler and more common solution is presented in Fig. 5.14. Here, a buffer amplifier is inserted after R_5, which prevents feedback current on $R_3 + R_4$ from affecting the R_5 shunt. This approach comes at the cost of increased noise due to the use of the second amplifier. The selection process of the amplifiers to form the IHCP was based on a multitude of parameters with the most important aspect of the IHCP being its noise performance and offset voltage drift temperature coefficient. After that, other parameters were considered such as maximum output current, bias current, CMRR, PSRR, power supply range, common-mode voltage range and availability.

The noise performance of the amplifier directly impacts the output noise of the

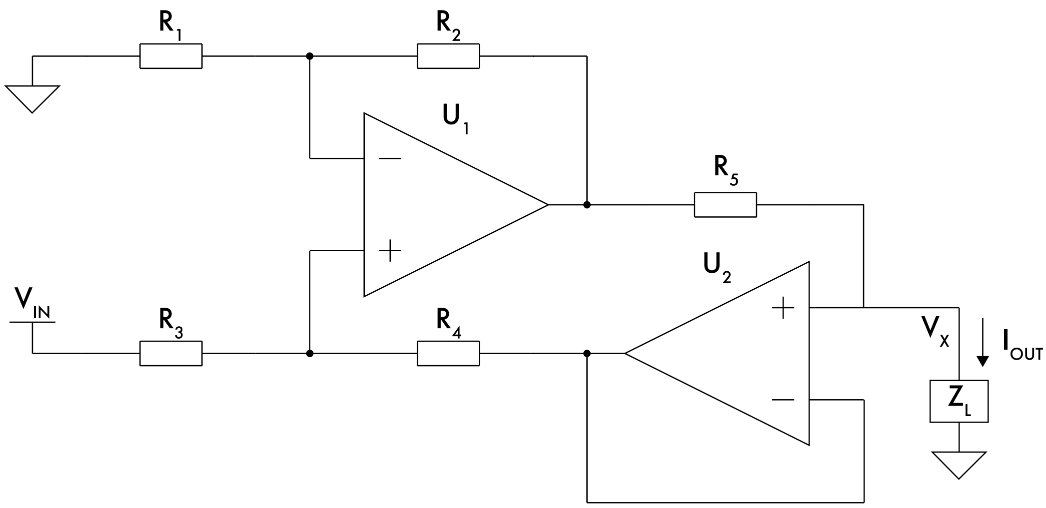

FIGURE 5.14 – Schematic of the "improved" Howland current pump based around two amplifiers. The current source works identically to the single amplifier configuration but the output error is minimised due to U_2 being introduced as a buffer to provide the output node V_x with high impedance, without needing to increase the resistance of R_3 and R_4.

IHCP and thus requires both input voltage noise and input current noise to be as small as possible. Another aspect of the noise is its 1/f corner frequency. If a part has a very low spot noise at frequencies $\geq$ 100 kHz (as many CMOS devices do) but its 1/f corner frequency is close to the reported spot noise frequency, its low frequency 1 - 100 Hz is most likely a couple of orders of magnitude higher [120]. It is thus important to select an architecture in which, 1/f is as small as possible to minimise coupling excess noise into the magnetometer bandwidth of interest 0.1 - 200 Hz.

Offset voltage drift is the next important aspect, as a large temperature coefficient can cause excess current drift that will in effect alter laser frequency. Three different amplifiers were considered: OPA2182 (Texas Instruments), OPA2210 (Texas Instruments) and ADA4099 (Analog devices). The OPA2210 was considered first as it was the amplifier that is used with the coil driver circuit. It features exceptional noise performance of 2.25 nV/$\sqrt{\text{Hz}}$ at 100 Hz with 1/f corner frequency at 10 Hz and very low drift of 0.1 μV/°C. OPA2182 was the second pick being a chopper based amplifier, it features practically zero drift with temperature

(0.003 μV/°C) and very low noise of 5.7 nV/$\sqrt{\text{Hz}}$ at 100 Hz.

The final pick was ADA4099 which features low voltage noise of 7 nV/$\sqrt{\text{Hz}}$ at 100 Hz, extremely narrow 1/f noise corner frequency of 6 Hz and very low drift of 0.1 μV/°C. The amplifier that was ultimately picked was the ADA4099. Despite being inferior to OPA2210 and OPA2182 in terms of noise and drift, it was a part that was available and in addition, featured shutdown capability, allowing for VCSEL to be switched on or off at will.

The current source was designed with an ADR4525D (Analog Devices) 2.5 V voltage reference and a set of ADA4099-2 (Analog Devices) amplifiers that serve as the IHCP. ADR4525D is a series voltage source. Series voltage sources feature typically lower noise and higher initial accuracy and benefit from lower power consumption than shunt voltage references such as buried Zener [151]. Buried Zener references however feature better drift performance than their series counterparts [152]. ADR4525D was selected because of its very low 0.1 - 10 Hz noise contribution of 1.25 μV and a typical noise spectral density of 45 nV/$\sqrt{\text{Hz}}$. Because the ADR4525 is a series voltage reference, its power consumption is low at 700 μA quiescent current draw and its voltage supply headroom is only 100 - 300 mV above the output. This means that it can be easily powered from 3.3 V supplies commonly present on microcontroller boards.

This version of the voltage reference is housed in a hermetically sealed ceramic package (denoted by the letter "D"). Packaging references into ceramic rather than plastic has a couple of unique advantages such as resistance to humidity and atmospheric pressure induced voltage drift. The ADR4525D exhibits a typical temperature coefficient of 0.8 ppm/°C as well as 1 ppm power cycle hysteresis. Keeping power cycle hysteresis low is important for devices that are not operated 24 hours, 7 days a week, such as portable instruments. Another advantage of ceramic packaged voltage references is their faster settling to the long-term drift "random walk" phase, which occurs in 100s of hours rather than 1000s. The initial accuracy of 0.02 % allows for operation without calibration to be possible and any potential calibration simpler.

The main disadvantage of ceramic packages is their cost and availability. However, since this reference will be used for other parts of the design (ADC, DAC, temperature control and biasing for the thermistor), it was decided to select the highest grade of voltage reference available. Initially, the same voltage reference present in the coil driver (LTC6655-LN) was considered due to its lower noise contribution but was ultimately rejected based on its higher drift and parts availability.

The signal from the reference is conditioned with an RC LPF (-3 dB at $\approx$ 16 Hz) to minimise the reference noise contribution. It is then followed by ADA4099-2 operational amplifier, which forms a buffer to the high impedance presented by the RC LPF so that it does not load the IHCP stage that follows.

As resistor matching affects the CMRR and ultimately output current present, it was important to select appropriate parts. For resistors $R_1 - R_4$ the 1 kΩ resistors with very low tolerance of 0.05 % and very low temperature coefficient of 5 ppm/°C were selected. The shunt resistor R_5 is a 714 Ω resistor with the same characteristics as $R_1 - R_4$ resistors. The transfer function of the current source is presented in Eq. 5.4

$$I_{\mathrm{OUT}} = \frac{\left(\dfrac{V_{\mathrm{IN}} \times R_2}{R_1}\right)}{R_5}\ , \tag{5.4}$$

where V_{IN} is the voltage of the voltage reference (2.5 V). This yields the output current of $\approx$ 3.5 mA. The circuit also features an additional capacitor present between R_3 and R_4 forming the second order of the LPF present before the first buffer. These capacitors were selected to be of polymer tantalum type that does not suffer from a piezoelectric effect like the class 2 multi-layer ceramic capacitor (MLCC) [153]. Immunity to piezoelectric effect is an important parameter when considering low noise applications as mechanical vibration would otherwise couple onto the output signal. This is especially important for portable sensors operating in environments prone to experiencing vibration. One such example is total field magnetometers mounted on a drone or towed behind an aeroplane for geosurveying.

5.2.2.2 Temperature controller

The second part of the VCSEL driver is its ability to precisely control the VCSEL temperature. From the requirements section, the temperature has to be controlled to at least 10 mK ($\approx$ 225 MHz) stability and ideally closer to 1 mK ($\approx$ 22.5 MHz). The challenge here is the operation at elevated temperature $\geq$ 25 °C, where the internal thermistor is operated in an asymptotic region increasing the noise and precision requirements of the driving electronic.
A typical temperature controller is based on an error amplifier that compares the desired temperature to the measured one. The error amplifier attempts to minimise the error signal and thus make the measured temperature match the desired temperature by driving some form of an actuator such as a heater or a cooling device. In this instance, the temperature can be monitored with the use of the VCSEL integrated thermistor and later by digitising the result with an ADC. The desired temperature or set point could be derived with a DAC while a form of an adjustable bridge amplifier is used to excite the integrated TEC. The error amplifier in this case could be a microcontroller that controls the control loop. However, instead of building the whole system from scratch some of the parts can be replaced with an integrated TEC controller. TEC controllers typically come in two types, digital and analogue. Digital control requires an ADC to measure the temperature of the thermistor and use a DAC to control the power amplifier driving current through the TEC and ultimately control the temperature of the VCSEL. The microcontroller is responsible for forming a feedback loop between the two. Often, a form of a proportional-integral-derivative (PID) controller is

used due to its ability to accurately control the process while at the same time maintaining good response speed.

PID controllers consist of three control terms. The proportional term is used to set the overall gain of the system. It is represented as a difference between the setpoint and measured value which form an error signal. If used independently, it will introduce an offset error between the set point and the measured value itself. It can be thought of as a control mechanism for present-time events. The integrating term takes into account the past values of the error signal. This term combined with the proportional term allows for the removal of the offset error caused by the proportional term. If the integration term value is too large, it will cause overshoot and can lead to instability, if the term is too small the response of the system can become sluggish. The integrating term represents a control mechanism taking into account past events. The last term is the derivative one. It is used to monitor the rate of change of the error signal. It is used in "anticipation" of a sudden change that the system can quickly react to and compensate for. For example, in the VCSEL temperature controller, it could be a gust of wind momentarily cooling the device. The derivative term would then try to counteract that. The derivative term can be thought of as a control mechanism for "anticipating" future events. The derivative term is often not used, as excess values can lead to noise being treated as a fast-changing signal which would lead to instability. The PID terms need to be tuned on a case-by-case process to achieve desired results.

The main advantage of digital controllers is their ease of tuning PID parameters, as all of the tuning happens in software. The disadvantage is the requirement for high precision and fast response of the ADC and DAC combo meaning that the control response is only as good as the data converters and TEC controller. In addition, digital PID control can be quite computationally intensive on the microcontroller. The alternative to that is the analogue controller, which utilises analogue electronics to form a PID loop. This approach does not require an ADC to be part of its feedback loop with only the DAC being used to present a set point. Another advantage is its inherent higher performance due to a direct actuation by the analogue electronics without data conversion having to take place. The microcontroller itself is also no longer responsible for the PID control, freeing resources for other tasks. The main disadvantage is the increased complexity of tuning the PID as it is done with passive components instead of digital variables. These components require soldering of physical components, a process that is both labour intensive and slow. It was decided to utilise the analogue PID controller, with digital setpoint control to enable digital frequency detuning control of the laser.

For the TEC controller, it was decided that the MAX1978 (Maxim Integrated) TEC controller would be used. This device features most of the necessary components to create a temperature controller. This includes a high efficiency fully bipolar power stage for controlling the TEC with an ability to source and sink up to 3 A of current with no dead zones or non-linearities at low driving currents. It also features integrated high precision chopper stabilised amplifiers, a precision integrator and a high gain error amplifier to form the PID loop allowing the design to achieve 1 mK ($\approx$ 22.5 MHz) temperature stability. The device also features TEC driving voltage and current limits which can be tailored to a particular VCSEL.

The parts that still needed to be added to complete the temperature controller were: the thermistor sensing mechanism, digital set point control with the use of a DAC and other external components used for programming the device voltage and current limits as well as the PID loop. It was also decided that the PID loop would be supplemented with an external, high precision temperature monitor with a temperature resolution below 1 mK over the operational temperature range of the VCSEL to allow for accurate monitoring of the VCSEL temperature. The first part was the design of the thermistor sensing mechanism together with monitoring capability.

The VCSEL uses a 10 kΩ negative temperature coefficient (NTC) thermistor as its temperature reading mechanism. It has an operating range between 40 - 90 °C and is anticipated to be run at higher currents yielding lower temperature requirements of ≈ 42 - 70 °C. This thermistor has one side internally attached to the cathode of the VCSEL diode, which makes it cathode grounded. Cathode grounding the thermistor offers the manufacturing benefit of being able to use fewer external connections but at the same time limits the connection and driving option of both the VCSEL diode and the thermistor. The VCSEL requires a driver that is ground referenced so that the voltage across the thermistor be measured in a single-ended mode (ground referenced measurement). Alternatively, this measurement can be done differentially (floating reference measurement), however, this presents a requirement for the use of instrumentation amplifiers and complicates the signal chain. Typically thermistors are either configured with another resistor in series to form a voltage divider or are operated on their own with a constant current source as depicted in Fig. 5.15.

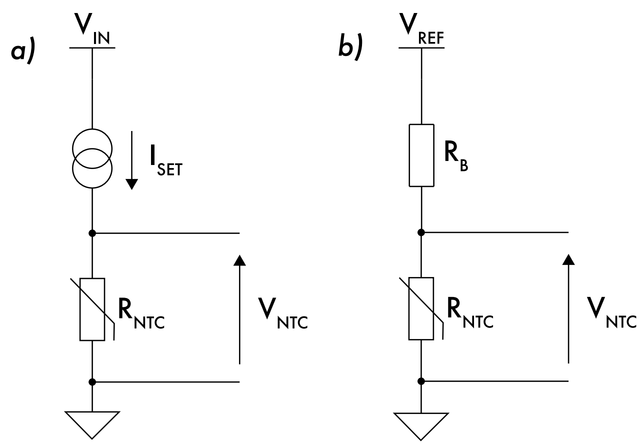

FIGURE 5.15 – Typical thermistor measurement configurations. a) Thermistor is excited with a constant current source where bias current I_{SET} flowing through the thermistor R_{NTC} directly produces voltage V_{NTC} that can be measured to obtain resistance of the thermistor as seen in Eq. 5.5. b) Thermistor forms a voltage divider network from a constant voltage source V_{REF} with a bias resistor R_{B}. The voltage across the thermistor can be measured to obtain its resistance as seen in Eq. 5.6.

$$R_{\text{NTC}} = \frac{V_{\text{NTC}}}{I_{\text{SET}}} \ . \tag{5.5}$$

$$R_{\text{NTC}} = \frac{\left(\dfrac{V_{\text{NTC}}}{V_{\text{REF}} - V_{\text{NTC}}}\right)}{R_{\text{B}}} \ . \tag{5.6}$$

The constant current source approach presents a couple of problems. The first one is a need for a circuit that will generate it, which needs to feature excellent stability and low noise, making the design more complex. The second one is the thermistor self heating effect, where the drive current has to be very small to minimise this effect. In addition, the use of a constant current presents some challenges with later forming a feedback loop to control the temperature of the VCSEL.

In a voltage divider configuration, a voltage reference can be utilised which is already part of the circuit. Additionally, if the same voltage reference is used for the ADC and DAC chain a ratiometric control loop is formed, which helps to eliminate drift associated with the reference. The self heating of the thermistor still occurs. However, its impact is reduced, as the power variation across different temperatures measured is more consistent in comparison to the constant current case.

The value of the resistor R_{B} needs to be optimised for three different parameters: output response, self heating, and availability as a precision component. By taking a geometric mean of the thermistor ranges used (42 - 70 °C), would yield a resistor value R_{B} of $\approx$ 2.935 kΩ. This value would maximise the sensitivity by producing a higher voltage drop but at the same time would let more current through the thermistor R_{NTC} increasing impact of self heating ($\approx$ 0.25 °C | 5.63 GHz). In addition, precision resistors are most often manufactured in common values such as 1 kΩ, 10 kΩ, 100 kΩ etc. which makes exotic values less likely to be available. To strike a balance, a 10 kΩ resistor with a low tolerance of 0.05 % and a very low temperature coefficient of 5 ppm/°C was selected to serve as the bias resistor R_{B}. As the temperature range of interest is 42 - 70 °C, with a 2.5 V reference and 10 kΩ bias resistor, the output voltage from the thermistor is in a range of $\approx$ 374 - 821 mV. If such a signal would go directly to an ADC that also uses 2.5 V reference its dynamic range would be largely unused. For this reason, the signal should be conditioned. The first step is to present a high impedance load to the thermistor so that it is not loaded. This is ideally done with a buffer that features a low bias current, which ultimately results in low offset voltage to faithfully reproduce the signal from the thermistor. The buffer architecture should ideally be chopper-stabilised so that the temperature coefficient can be minimised. The next step is to apply voltage offset and gain to the buffered thermistor response so that it can be translated into the ADC range. This can be achieved with an inverting level shifter configured op-amp. Using an inverting-level shifter is beneficial for two reasons. The first one is that it inverts the response from the thermistor so that increased temperature is indicated by the increase in voltage rather than the drop. The second, more important is that it allows for manipulation of the noise gain of the amplifier, meaning that by reducing bandwidth with a compensation capacitor the gain after the corner frequency can fall below 0 dB which in turn lowers the noise from signal conditioning. Appropriate amplifiers for both the buffer amplifier as well as the level shifter are available on the MAX1978 and were utilised for this application. The completed circuit is presented in Fig. 5.16.

The resulting signal from the inverting level shifter needs to go through an ADC so that it can be digitised and made available as a temperature | detuning frequency value. This ADC needs to feature enough resolution to be able to resolve < 1 mK (22.5 MHz) to allow for accurate tuning of the laser frequency.

A 1 mK step at 70 °C from the thermistor divider would correspond to ≈ 10.7 μV, by going through the level shifter this signal increases to ≈ 60 μV lowering the bit requirement of the ADC from $\approx$ 17.8-bit to $\approx$ 15.4-bit. A 16 bit ADC could

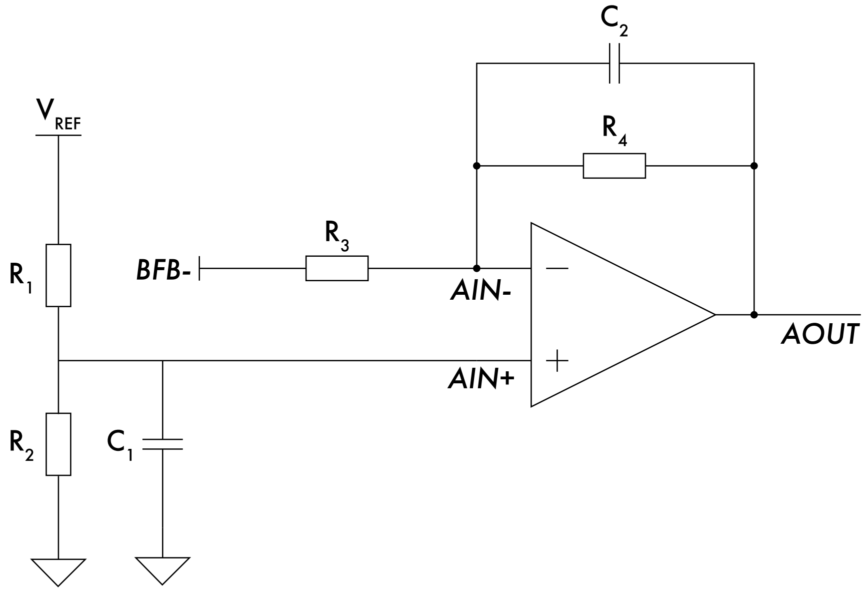

FIGURE 5.16 – Schematic diagram of the inverting level shifter used to condition the buffered thermistor output. All resistors have a tolerance of 0.1 % and feature a temperature coefficient of 10 ppm. Where R_1 and R_4 are 100 kΩ, R_2 is 37.5 kΩ, R_3 is 18 kΩ, C_1 is 470 nF, C_2 is 220 nF. The design uses one of the MAX1978 integrated chopper amplifiers to form the shifter. $BFB-$ is the buffered output of the thermistor divider.

be used to monitor the thermistor however, typically ADCs bit resolution stated in a datasheet refers to the maximum bits that the device can allocate but often the more important metric of "noise-free bits" is lower. In addition, inexpensive, $<$ 16-bit $\Delta\Sigma$ converters feature their own internal voltage reference that the designer has no access to. Because the reference is tied to a single part and cannot be accessed would mean that the measurement would no longer be ratiometric with respect to the reference used to drive the thermistor, leading to increased drift.

To provide some margin the converter should feature at least one more bit than it is required. In addition, the converter would be used in single-ended mode. This means that if a differential input ADC would be used in this configuration only half of its range is utilised, meaning that an additional bit is required. This brings the converter's total bit depth requirement to $\geq$ 18-bit. The converter ultimately selected for this task was MAX11210 (Maxim Integrated) which is a 24-bit $\Delta\Sigma$

ADC, featuring very low zero drift of 50 nV/°C, built-in 50/60 Hz filters, noise-free resolution (NFR) up to ≈ 21 at a sample rate of 0.833 samples per second (SPS) (50 Hz filter operation) with 0.21 μV_{RMS} of noise.

As the output of the pre-conditioning circuit features a 5 Hz bandwidth, the sample rate required is ≥ 10 SPS in order to prevent aliasing [154]. At the sample rates of 50 SPS, the NFR exceeds 18-bit (1.45 μV_{RMS} | 0.03 mK) making it ideally suited for thermistor temperature monitoring. For higher resolution measurements an optional software moving average filter was implemented that helps to reduce the impact of the noise from the signal chain components. The combined ADC and conditioning filter are thus capable of resolving the thermistor temperature down to ≤ 0.05 mK (in the range of 42 - 70 °C), translating to the laser frequency tuning resolution of 1.1 MHz.

MAX112XX series of devices feature pin-compatible converters with a resolution range of 16 - 24-bit in 2-bit increments. Initially, the 18-bit version of the device was considered (MAX11209) however the only one that was available at the time was the 24-bit version with the optional pre-amplifier that was not used. The pricing between different parts was similar hence why the 24-bit part was selected. In addition, the fact that each device is pin-compatible meant that in the future a different device from the same series can be used instead.

The next step was the design of the set point generation circuit. The overall precision and stability of the temperature controller are only as good as the set point signal. For this reason, care must be taken in the design and selection of components so as to not sacrifice signal integrity. The set point signal noise must be below the 1 mK step so that it can be successfully resolved.

Recalling the temperature monitoring circuit a 1 mK step at 70 °C is equivalent to ≈ 10.7 μV. Given that the same voltage reference should be used to drive the DAC so that all devices are ratiometric against one other gives us a voltage of 2.5 V. To achieve ≤ 10.7 μV step resolution provides a requirement for ≥ 17.8-bit resolution.

Unlike the ADCs, precision high bit resolution DACs are expensive for devices featuring higher resolution than 16-bit. However, the same approach can be utilised as in the case of the temperature monitor where a voltage level shifter is employed to maximise the dynamic range of the DAC. This time, however, the non-inverting level shifter was used as it could be assembled out of three resistors without modification to the voltage reference voltage. This approach requires fewer precision components and by that less error contribution from the temperature drift.

The programming temperature range was reduced by ≈ 1 °C compared to what the ADC measuring chain can read. This was done so that the temperature value can never be set outside of the measuring range.

With the level shifter, the minimum resolution required comes out to ≈ 15.4-bit. For the DAC, the DAC8830 (Texas Instruments) was selected. It is a 16-bit, precision DAC featuring low noise of 10 nV/$\sqrt{\text{Hz}}$, linearity down to 1 LSB and unbuffered output. The unbuffered output is normally undesired, as it means that the output impedance is dynamic depending on the current DAC code value. However, this means that by default it features a very low drift of $\pm$ 0.05 ppm°C. The external output buffer amplifier can be thus selected to maintain this performance. For the output buffer and the other two buffers present in the level shifter, an ADA4522-4 (Analog Devices) quad chopper stabilised amplifier was used. It features very low noise of 5.8 nV/$\sqrt{\text{Hz}}$ at frequencies higher than 1 Hz and a typical offset drift of 2.5 nV/°C. Its contribution should not impact the established DAC performance. In addition, it was important that the amplifier features rail-to-rail performance on its input and output or that the input sensing includes GND potential so that the full dynamic range of the DAC can be used. The summing junction of the level shifter also features a 470 nF film capacitor to limit the bandwidth and noise coming from the DAC and the reference. A schematic of the conditioning circuit is presented in 5.17.

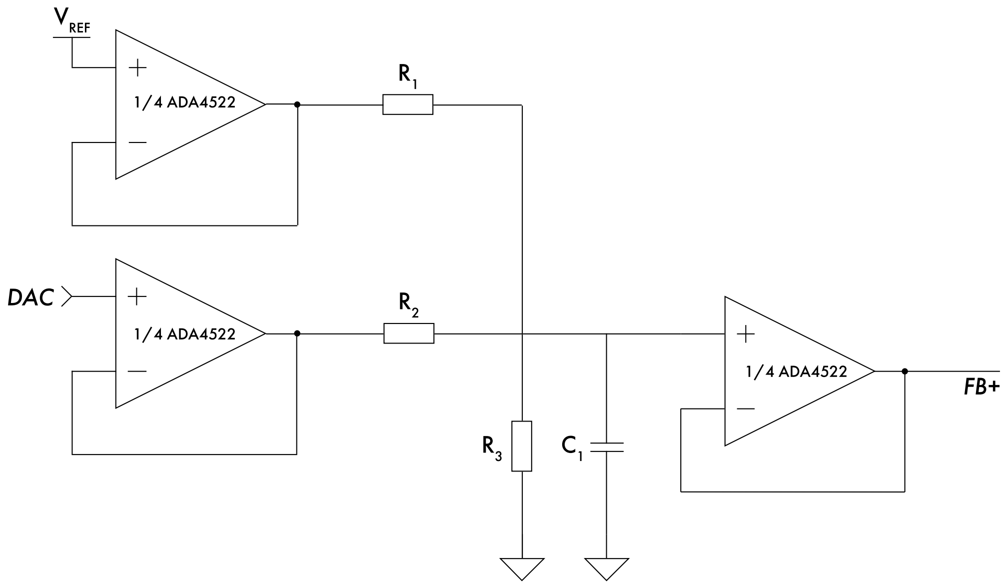

Figure 5.17 – Schematic diagram of the non-inverting level shifter used to condition the temperature setpoint. All resistors have a tolerance of 0.1 % and feature a temperature coefficient of 10 ppm. Values of R_1 and R_2 are 10 kΩ, R_3 is 2.26 kΩ, C_1 is a 470 nF film capacitor.

The last part is the selection of components for the PID loop. Unlike traditional tuning of PID controllers, where the design is iteratively tested using different values of P, I and D until the desired performance is achieved, a transfer function of the loop was selected as a tuning mechanism of choice. The compensation of it is achieved with a selection of passive components so that a stable, fast response is obtained.

Typical TEC can be modelled as a two-pole system, meaning that the second pole has the potential of creating an oscillatory component as its phase crosses 180° while the gain is positive thus fulfilling the Barkhausen criterion [155]. Simply using a LPF as a form of dominant pole compensation would be insufficient. This is because, in a typical butterfly package (used for DBR lasers), the first pole is positioned such that its crossover frequency is well below 100 mHz requiring large values of capacitance that would make the system response extremely sluggish. Instead, an integrator approach is used where the TEC poles are cancelled with zeros, with the aim of achieving sufficient phase margin so that the system is not oscillatory. It was expected that the VCSEL in a TO-46 package would feature its first pole at a higher frequency to the DBR in butterfly package. However, in order to improve the frequency response of the loop, an integrator approach was selected.

The first step was to find out the location of the two poles of the VCSELs built in TEC. To do this the feedback loop was broken so that the input of the MAX1978 control input pin, $CTLI$ could be connected to a function generator generating a sinewave with an appropriate DC offset. The thermistor response was monitored with one channel of the oscilloscope while the other one was used to monitor the signal generated from the generator. The setup is illustrated in Fig. 5.18

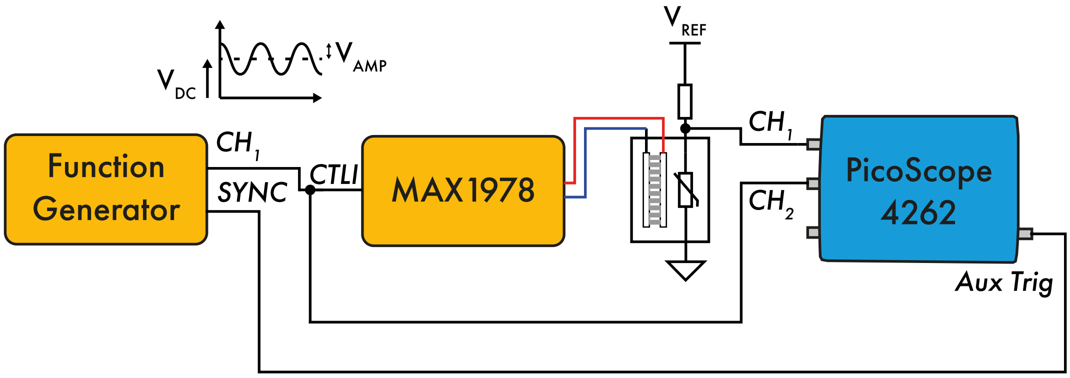

FIGURE 5.18 – VCSEL TEC response estimation test setup. A function generator (Agilent 33320) was used to drive the control input $CTLI$ of MAX1978 with a sinewave with an offset V_{OFF} of 1.5 V and an amplitude of V_{AMP} 50 mV and was swept from 1 mHz to 80 Hz in logarithmic increments. The MAX1978 controls the current through the TEC with the signal from $CTLI$ with transfer function presented in Eq. 5.7 where V_{CTLI} is the voltage applied to the $CTLI$ input, V_{REF2} is the internal reference of MAX1978 with a value off 1.5 V and R_{SENSE} is the 150 mΩ shunt resistor measuring current through the TEC. The thermistor response was measured on channel 1 of an oscilloscope (PicoScope 4262) and the V_{CTLI} was measured on channel 2 as a reference. The function generator triggers the oscilloscope at the start of each sinewave.

$$I_{\mathrm{TEC}} = \frac{V_{\mathrm{CTLI}} - V_{\mathrm{REF2}}}{10 \times R_{\mathrm{SENSE}}}\ , \tag{5.7}$$

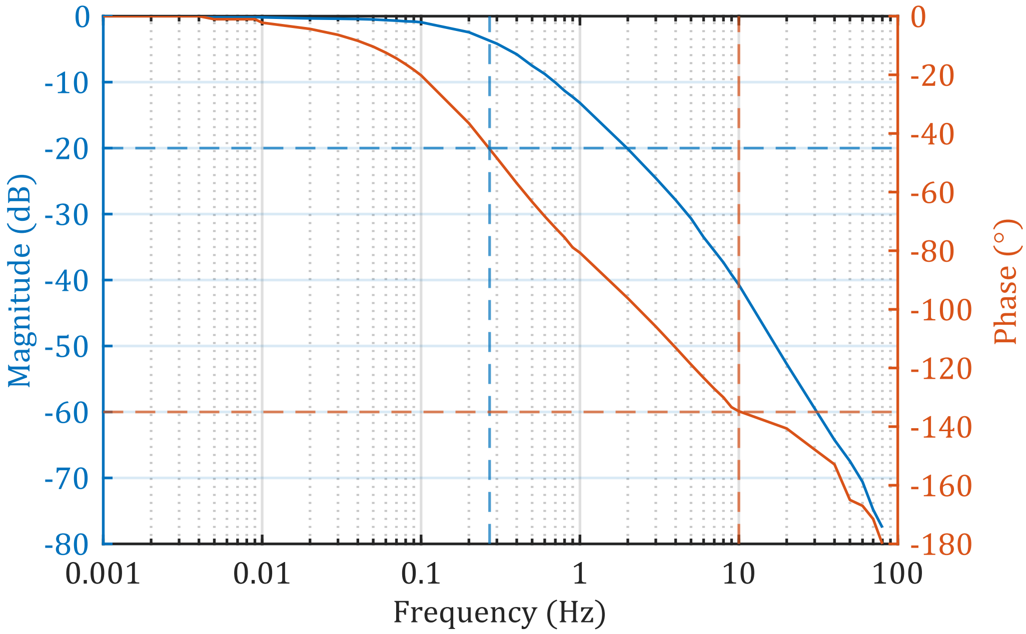

Figure 5.19 – VCSEL TEC response obtained from the test setup in Fig. 5.18. The magnitude response is presented in blue and the phase in red. Dashed lines show the location of poles at their crossover frequencies.

By sweeping the frequency of the input sine wave and monitoring the response, it is possible to obtain the magnitude and phase response of the TEC and estimate the location of the two poles. The response is presented in Fig. 5.19.

From the TEC response testing it was estimated that the first pole occurs at ≈ 250 mHz and the second at ≈ 10 Hz. This was estimated from the locations of $45°$ and $135°$ phase shifts in the frequency response. The poles are located at higher frequencies than typical butterfly-packaged telecoms lasers (which MAX1978 is designed to work with). This is due to the much lower thermal mass of the VCSEL and its integrated TEC. With the knowledge of the location of the poles, the PID loop components can be selected. The schematic of the internal integrator forming PID controller is seen in Fig. 5.20. The compensation process is based on the information provided in the MAX1978 datasheet [156]. The first step is the selection of R_3 and C_2 (that form an integrator) for maximum DC gain. This is done for accuracy reasons. This, however, comes at the cost of noise. The

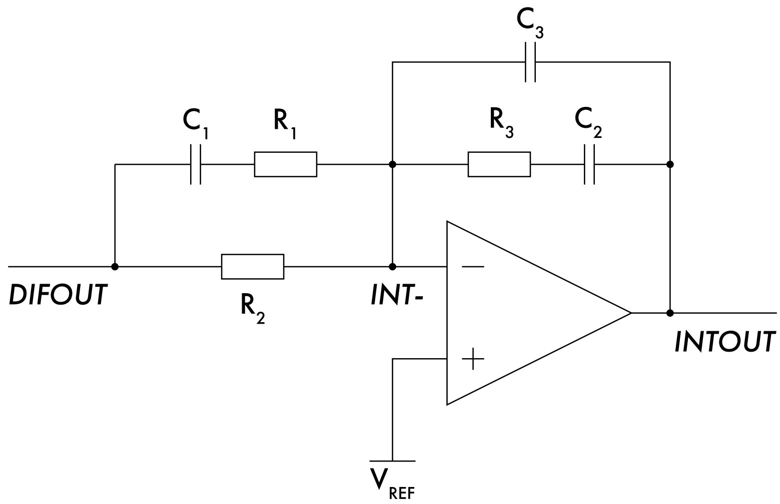

FIGURE 5.20 – Schematic diagram of the PID controller made out of internal amplifier present in MAX1978 TEC controller and external passive components.

datasheet recommends the use of low leakage capacitors such as film capacitors and resistors featuring low temperature coefficient. The recommendation was followed for the resistor, however, a tantalum polymer capacitor was used in place of a film capacitor. This was done as film capacitors would be physically too large for the expected capacitance values. Modern polymer tantalum capacitors are also much better than the standard tantalum capacitors exhibiting lower current leakage than standard ones while at the same time, they do not suffer from the piezoelectric effect that class 2 ceramic capacitor exhibit. The values of C_2 and R_3 are responsible for setting the first zero, $\mathcal{Z}_1$ (from Eq. 5.8) to compensate for the action of the first TEC pole, $\mathcal{P}_{\mathrm{TEC1}}$. It is recommended to set the $\mathcal{Z}_1$ to $\leq$ 8 times the frequency of $\mathcal{P}_{\mathrm{TEC1}}$. Going further can result in a phase falling below -135° which can cause a wrap-around situation of reaching -180° and cause instability. The value of C_2 was selected to be 10 μF and R_3 used to bring the $\mathcal{Z}_1$ to 2 Hz thus becoming $\approx$ 7.96 kΩ (8.2 kΩ selected).

$$\mathcal{Z}_1 = \frac{1}{2\pi \times R_3 \times C_2} \ . \tag{5.8}$$

The next step is the maximisation of the phase margin near $\mathcal{P}_{\mathrm{TEC2}}$, which is achieved by increasing the gain of the $\mathcal{P}_{\mathrm{TEC2}}$ crossover frequency (10 Hz) until it reaches 0 dB. From Fig. 5.19, the gain needs to be increased by $\approx$ 40 dB. The MAX1978 internal error amplifier features a gain of 50 ($\approx$ 34 dB) so the gain needs to be set to 6 dB at 10 Hz. The C_1 (from Eq. 5.9) and R_3 are setting the integrator gain (A) at the crossover frequency (f_c). Yielding C_1 to have a value of $\approx$ 3.24 μF (3.3 μF selected).

$$C_1 = \frac{A}{\frac{1}{C_2} + 2\pi \times R_3 \times f_c} \tag{5.9}$$

The TEC second pole, $\mathcal{P}_{\mathrm{TEC2}}$ is cancelled with a zero to provide a maximum phase margin. The datasheet recommends setting the second zero, $\mathcal{Z}_2$ to at least 1/5 the crossover frequency to ensure enough of phase margin, and to allow for variation in the location of $\mathcal{P}_{\mathrm{TEC2}}$. The $\mathcal{Z}_2$ is thus set to 2 Hz and R_2 is found with Eq. 5.10 to be $\approx$ 24.11 kΩ (24.3 kΩ selected).

$$\mathcal{Z}_2 = \frac{1}{2\pi \times R_2 \times C_1} \ . \tag{5.10}$$

To close the action of the $\mathcal{Z}_2$, a pole $\mathcal{P}_1$ is introduced to at least 5 times the crossover frequency following the same recommendation. $\mathcal{P}_1$ is set to 50 Hz and R_1 is found with Eq. 5.11 to be $\approx$ 965 Ω (1 kΩ selected).

$$\mathcal{P}_1 = \frac{1}{2\pi \times R_1 \times C_1} \ . \tag{5.11}$$

Finally, the $\mathcal{Z}_1$ is terminated by the roll-off frequency of the pole $\mathcal{P}_2$. It is recommended that the position of the $\mathcal{P}_2$ is double the frequency of $\mathcal{P}_1$, thus setting $\mathcal{P}_2$ to 100 Hz. This provides the last component value C_3 found with Eq. 5.12 to be $\approx$ 194.1 nF (220 nF selected).

$$\mathcal{P}_2 = \frac{1}{2\pi \times R_3 \times C_3} \ . \tag{5.12}$$

The final values for the PID controller presented in Fig. 5.20 are: $C_1 = 3.3$ μF, $C_2 = 10$ μF, $C_3 = 220$ nF, $R_1 = 1$ kΩ, $R_2 = 24.3$ kΩ, and $R_3 = 8.2$ kΩ. Resistors were selected to have a low temperature coefficient ≤ 25 ppm and capacitors are a mix of polymer tantalum capacitors for values ≥ 1 μF and for C_3 a class 1, C0G dielectric capacitor was selected. C0G dielectric capacitors feature a very low temperature coefficient ≤ 30 ppm and do not exhibit the piezoelectric effect [153]. The datasheet presents the above component values as a "good starting point" and that further optimisation is required on a case by case basis. The further optimisation process is covered in Section 5.2.3.2.

5.2.2.3 Digital control

The requirements previously outlined in Section 5.2.1 present a requirement of frequency tuning the laser to enable at least $\pm$ 30 GHz scanning range which is accomplished by temperature control of the VCSEL. Because the device will be subject to parametric scans outlined in Section 3.5 the driver requires the ability to be programmatically tuned. To enable this a microcontroller is required.

The VCSEL driver is controlled by the RP2040 (Raspberry Pi) microcontroller present on the Arduino Nano Connect board. As with the coil driver design, the Arduino ecosystem was selected for its accessibility and ease of use. The RP2040 was selected instead of ATmega4809 found on the coil driver system due to availability and its better performance than ATmega4809, as initially the VCSEL driver was supposed to be a part of a bigger system that would feature extra subsystems requiring extra performance.

Firmware for the device allows for communication with peripherals using serial universal asynchronous receiver-transmitter (UART) command interface. The ADC and DAC are controlled over a serial peripheral interface (SPI) bus, which allows for controlling the temperature of the VCSEL diode and by that, its frequency. Both the current source and the TEC controller can also be switched on or off with the use of the command interface implemented over the UART bus.

5.2.2.4 Power delivery

The device was designed with portability in mind. It is powered and controlled through an USB, with other voltage rails derived locally. The power tree diagram of the device is presented in Fig. 5.21.

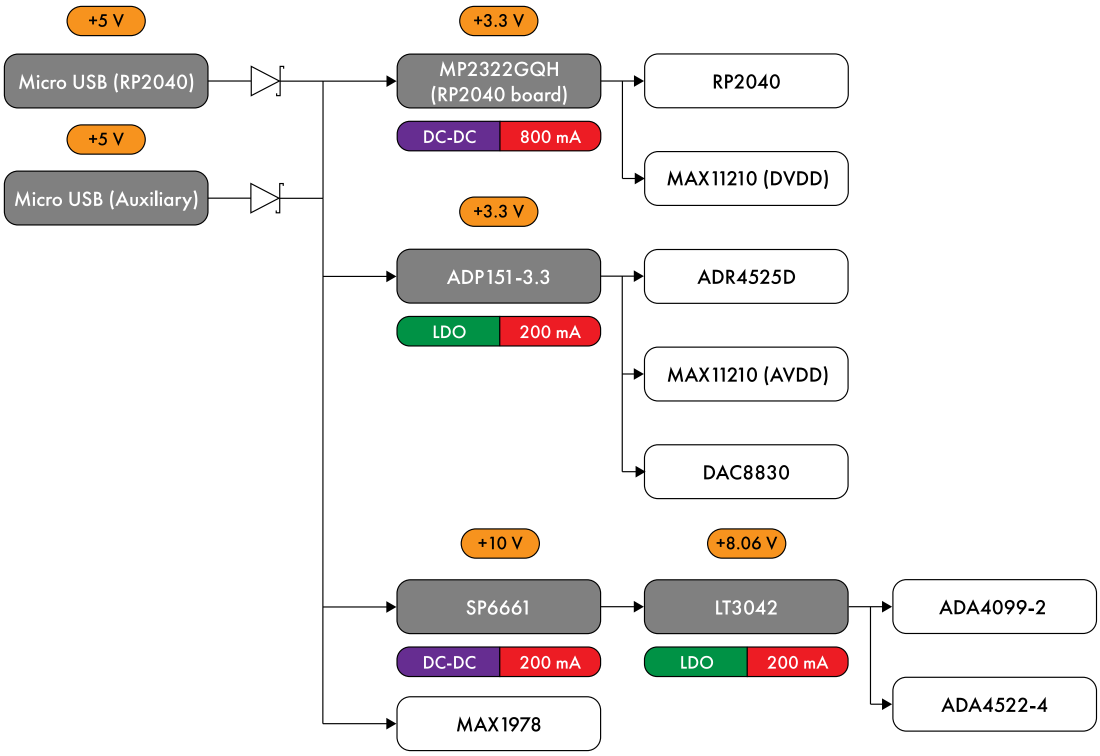

Figure 5.21 – Power tree of the VCSEL driver. The grey blocks are either power sources or regulators. The maximum output current is presented in red. The type of regulator is presented either in green or purple for LDO or DC-DC converters respectively. White blocks determine individual components. The voltage present on the line is shown in orange boxes.

To meet the compliance voltage requirement of ≤ 2.5 V for a range of VCSEL diodes 5 V rail after regulation would have been insufficient. Instead, the 5 V rail was doubled using a charge pump voltage multiplier which is later regulated to ≈ 8 V that is ultimately used to power the op-amps in the IHCP of the constant current source. This rail is also used for signal conditioning of the TEC controller temperature setpoint. To achieve voltage doubling an SP6661 (Maxlinear) charge pump was used.

SP6661 was selected as it is a type of "modern" charge pump that can operate at high frequency ($\approx$ 1 MHz) and output up to 200 mA of current. Higher frequency operation trades some of the efficiency of the charge pump ($\approx$ 3 % due to switching losses) but allows to use of a capacitor with lower capacitance and moves the voltage ripple caused by switching away from the operational frequency of the circuit components. Higher switching frequency also allows for easier filtering, as passive component values become smaller.

The input and output of the charge pump has been filtered with an inductor (L) capacitor (C) (LC) Π filters. The purpose of the input filter is not to filter the 5 V rail before reaching the SP6661 charge pump but rather to filter its switching noise from feeding back and modulating the input 5 V rail [157]. The filters were designed to attenuate the switching frequency ripple by 60 dB. The filter has been dampened with ferrite beads, that also attenuate the high frequency spikes from the operation of the charge pump.

The output of the charge pump is unregulated and would change with load changes as well as changes to the input voltage. This could cause excess noise at lower frequencies of the devices that it powers. For this reason an LT3042 (Analog Devices) LDO was selected. LT3042 features very high PSRR (118 dB at 100 Hz) which is maintained at much higher frequencies (79 dB at 1 MHz) than typical LDOs, this part also features very low noise (2 nV/$\sqrt{\text{Hz}}$ at 10 kHz) that is independent of the output voltage. These parameters make it an ideal choice for ultra low noise instrumentation and for DC-DC converter post regulation.

The device was programmed with an 80.6 kΩ thin film resistor with a temperature coefficient of 25 ppm and had a 10 μF X5R capacitor added in parallel to regulate the incoming 10 V from SP6661 into 8.06 V rail that will be used to drive op-amps used in the current source as well as signal conditioning for the TEC controller.

The combined post SP6661 filter attenuation and LT3042 PSRR result in overall ripple attenuation of ≈ 140 dB.

The VCSEL driver features two USB connectors, one present on the RP2040 microcontroller board and an external one that allows extra power to be delivered to the board. This extra USB is power muxed using a very low forward voltage drop Schottky diode that presents only 250 mV of voltage drop at 1.5 A. The extra USB is used for laser devices that would require higher TEC current (such as laser diode mounts) considering that the controller is capable of outputting up to 3 A to the TEC. The VCSEL driving application is designed for TO-46 package VCSELs and the TEC current is limited to 1 A. Higher current outputs would be used for VCSELs that do not feature on-board TECs. The temperature of these is controlled with a special mount, featuring a TEC.

5.2.3 Device testing

The device testing is split into two parts. One is concerned with the testing of the current source and the other with the TEC controller.

5.2.3.1 Current source testing

The current source was put through the same range of tests that were previously performed on the coil driver covered in Section 4.4. The first test that was performed was the noise floor test.

The setup for the test was almost identical to the noise testing setup presented in Fig. 4.3. The only thing that was changed was the load resistor value from 300 Ω to 1 kΩ to achieve higher measurement resolution. The results of this test are presented in Fig. 5.22.

The noise exhibited by the current source is very low, on the order of ≈ 91 pA/$\sqrt{\text{Hz}}$ at 1 Hz ≈ 40 pA/$\sqrt{\text{Hz}}$, at 10 Hz and ≈ 7 pA/$\sqrt{\text{Hz}}$ at 183 Hz which is the optimal modulation frequency used in the Cs SERF magnetometer. The ultra-low current

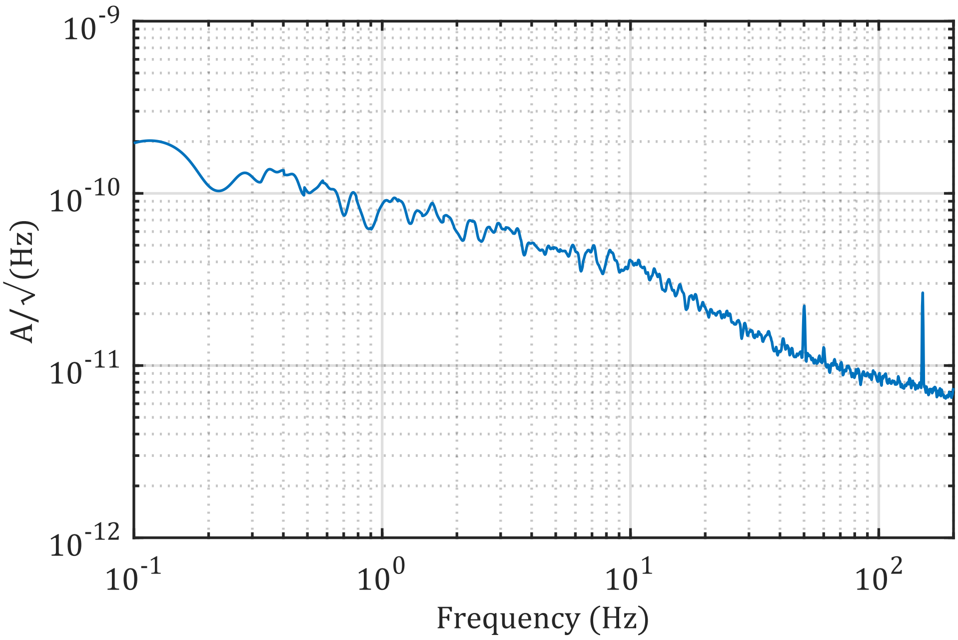

FIGURE 5.22 – NSD results in a bandwidth of 0.1 - 200 Hz for the VCSEL driver delivering 3.5 mA. The high gain probe has been terminated with a 1 kΩ 0.1 % resistor, R_{L}. The peaks at 50 Hz and 150 Hz are believed to be AC mains and its harmonics, picked up by the probe. The NSD was obtained using a LPSD algorithm [87] made out of 2048 FFT points using a Hann window with amplitude scaling correction applied.

noise contribution should translate well to the low intensity noise contribution of the laser, especially at the very low frequencies where it typically dominates.

The current noise contributes negligible laser frequency noise of ≈ 30 Hz/$\sqrt{\mathrm{Hz}}$ assuming ≈ 0.75 GHz/mA frequency shift for Cs found experimentally. Similar to the coil driver, the current source driving the VCSEL needs to be stable. The current source stability of the laser directly affects the frequency drift of the laser. It is thus important that the device is stable enough to not cause excess frequency drift, potentially away from the atomic transition of interest.

Using the test setup from Fig. 4.6 the current source was plugged into the SMU which this time was configured to require a compliance voltage of 2.2 V from the source which mimics the typical forward voltage of the VCSEL. The setup was left for 24 h to observe the current drift of the device. The results of this test have been plotted using overlapping Allan deviation and are presented in Fig. 5.23.

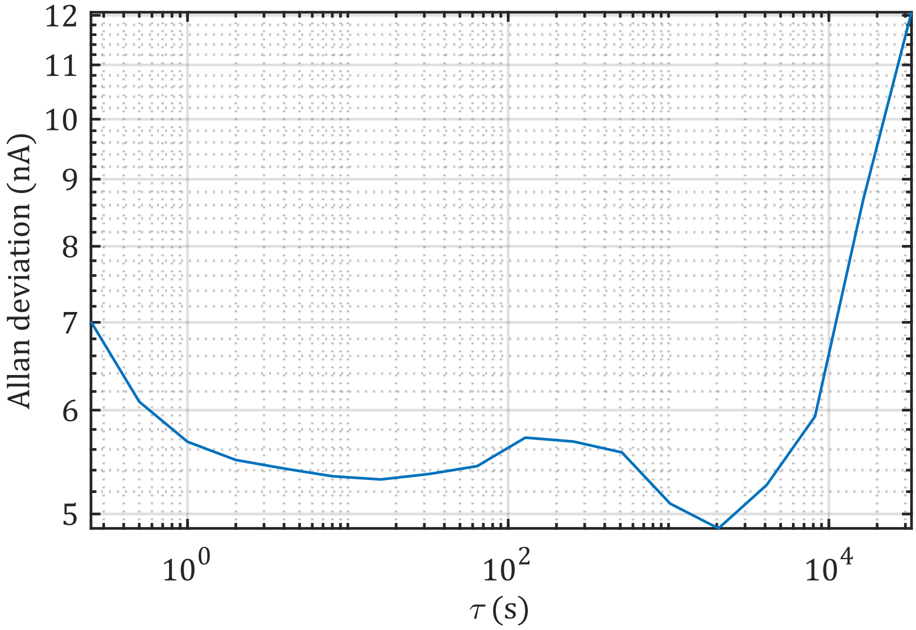

FIGURE 5.23 – Allan Deviation of VCSEL driver current source. The device features a higher drift than a coil driver which could be attributed to the use of amplifiers and a voltage reference that features higher drift. The device exhibits a long term low frequency drift, but even after 24 hours, it does not drift far enough to compromise its performance.

The resulting Allan deviation shows some drift on the nA scale which when converted to frequency does not exceed 2 MHz in 24 hours, which is negligible for our application.

5.2.3.2 Temperature controller testing

The temperature TEC controller is responsible for the precise keeping of the temperature of the VCSEL. For a typical frequency shift of $\approx$ 24.3 GHz/°C, it is thus expected that the dominant source of frequency noise and drift will come from the TEC controller.

To test the temperature controller noise, it was decided to test it optically with the use of a Cs reference cell. The test setup is presented in Fig. 5.24.

The collimated laser beam is first attenuated by the 0.5 neutral density (ND)

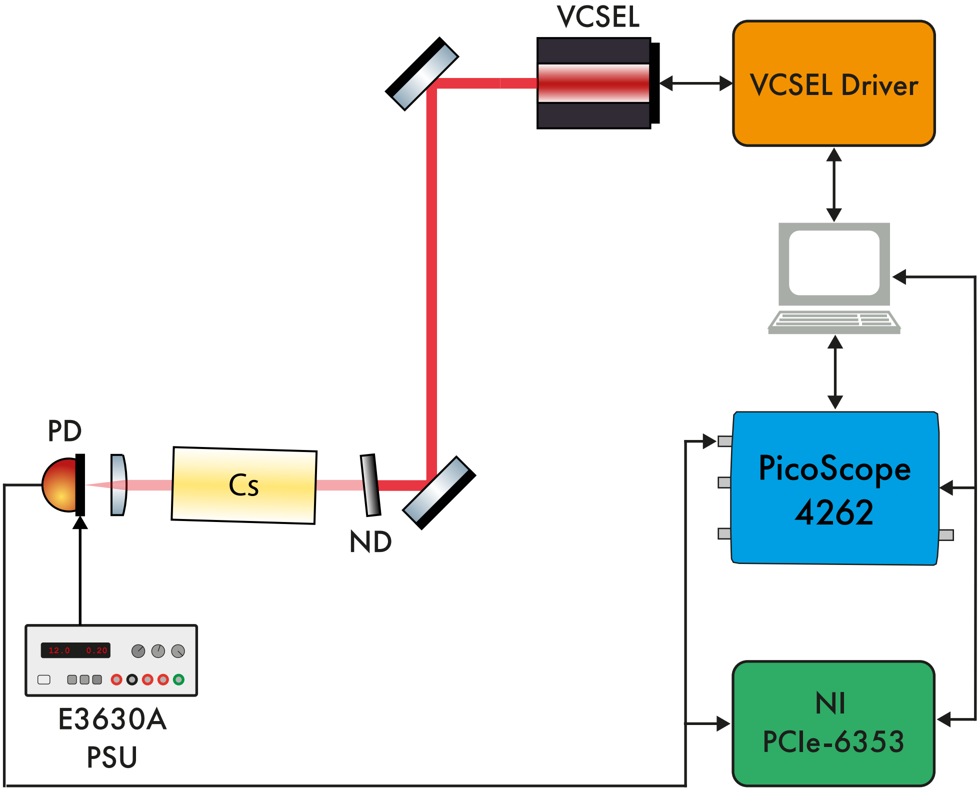

FIGURE 5.24 – Cs spectroscopy setup. The VCSEL temperature and current are driven by the VCSEL driver. ND: neutral density filter. Cs: Cs vapour reference cell PD: Photodetector from Section 5.1 with a gain selection of 10, 20, 40.2 kV/A, ≈ 16 kHz bandwidth and a focusing lens in front. It is powered by the E3630A power supply. The resulting signal is sampled by the 16-bit oscilloscope (PicoScope 4262) and the analogue input of NI-PCIe-6353 DAQ card used previously in Chapter 3.

filter to enable sufficient absorption of the incident light on the atoms in the Cs reference cell, without saturation. The ND filter as well as the Cs reference cell have all been tilted at a slight angle to prevent any optical feedback from affecting the VCSEL.

The temperature of the VCSEL was first coarsely adjusted with LabVIEW software in order to find the approximate location of the D_1 hyperfine transition.

The VCSEL driver is controlled with LabVIEW and works alongside the DAQ to obtain the spectroscopy of the Cs D_1 line. First, a command to set the temperature is sent to the VCSEL driver where the software reads the temperature until it stabilises to within 1 mK. After the temperature stabilises, a series of DAQ measurements are taken and an average DC voltage is derived and saved as a point. This process is repeated until the desired temperature range is covered. The typical temperature sweep is 0.7 °C wide, constituting $\approx$ 17 GHz scan width, to ensure that the width of the D_1 line is fully resolved. The results of this are presented in Fig. 5.25.

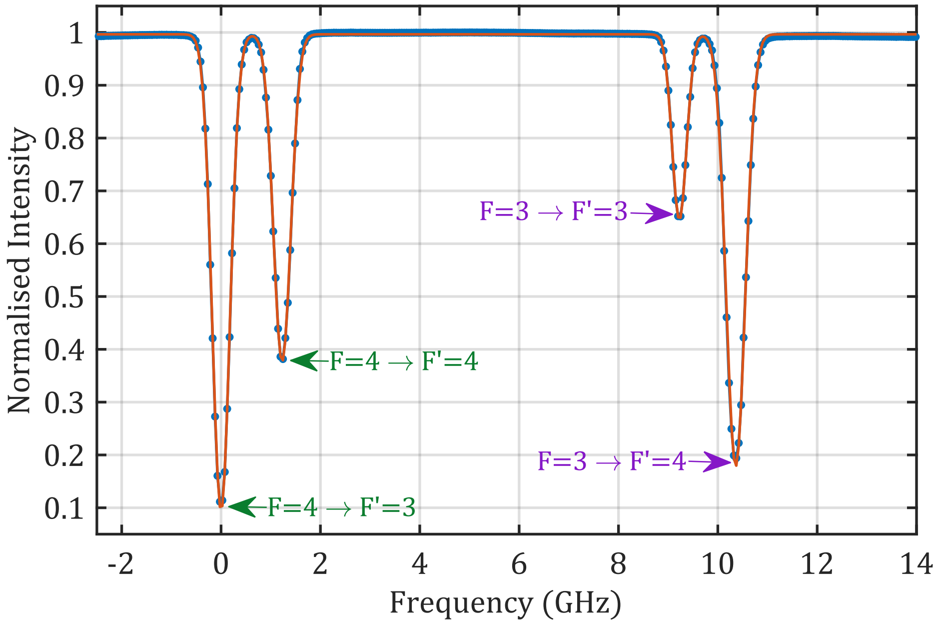

Figure 5.25 – VCSEL Cs spectroscopy results. The experimental data with a fixed baseline are presented in blue "O" markers and the fitted data (four Gaussian fit) are in red. $F = 4$ transitions are presented in green and $F = 3$ transitions in purple. The $F = 4 \rightarrow F' = 3$ transition was used as the 0 GHz detuning point, as it was done in the Cs SERF experiment.

The obtained spectroscopy shows clear absorption peaks at expected levels. After the spectroscopy was obtained, the laser was tuned to the middle of $F = 4 \rightarrow F' = 3$ transition and data was sampled for 100 seconds with a PicoScope 4262 oscilloscope in order to estimate its frequency noise contribution.

After the data was sampled it became apparent that the noise contribution was higher than expected. Plotting its NSD revealed a peak at 60 Hz, which was attributed to PID controller instability. Based on the response of NSD, the circuit was simulated using Simulation Program with Integrated Circuit

Emphasis (SPICE) software and the passive component values were optimised. The optimisation process consisted of minimisation of the pre-emphasis at 60 Hz, and optimisation of the overall gain of the transfer function. The device was then retested under the same conditions as described previously. The NSD results for the unoptimised and optimised PID are presented in Fig. 5.26.

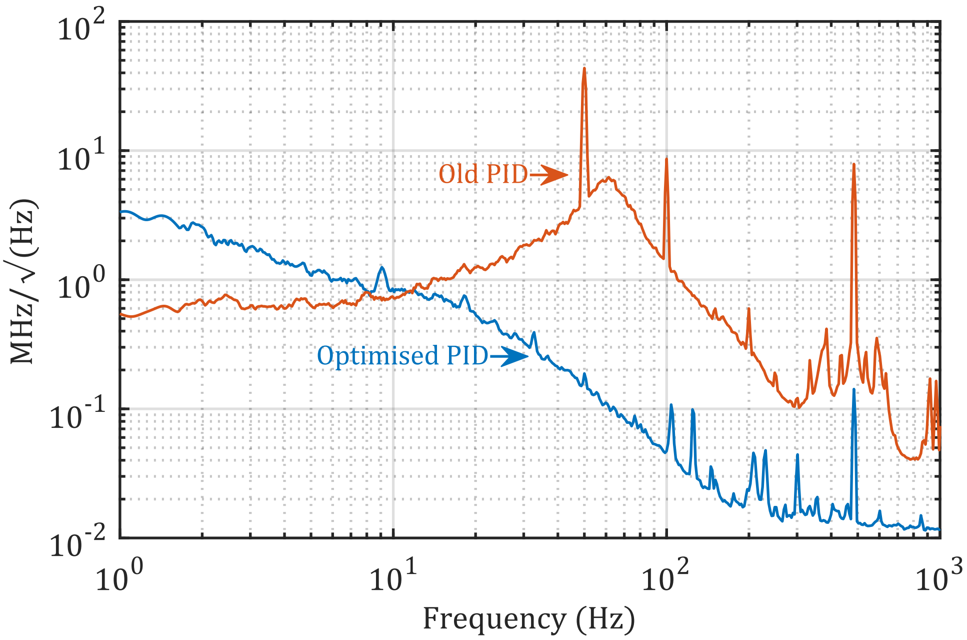

FIGURE 5.26 – NSD results of the TEC controller PID configurations. The old PID response is presented in red and the optimised PID is in blue. The NSD was obtained using a LPSD algorithm [87] made out of 1024 FFT points using a Hann window with amplitude scaling correction applied.

It can be seen that the peak at 60 Hz has disappeared and has been replaced with a decaying slope, starting at low frequencies. The raised low frequency response at 1 Hz is due to increasing the DC gain of the loop response. As mentioned previously high DC gain is beneficial as it allows for the minimisation of the error in the loop, allowing for better tracking. The time domain performance yielded $\approx$ 0.47 mK RMS noise equal to a frequency noise of $\approx$ 11 MHz RMS in the bandwidth of 0.1 Hz - 5 kHz (bandwidth of the measurement setup).

The next test involved testing the long term stability of the temperature controller. For this test, the setup from Fig. 5.24 was used following the same procedure of scanning the D_1 transition and tuning the laser to the middle of $F = 4 \rightarrow F' = 3$ transition. This time, however, the device was left for 12 hours, sampling data with the use of a PicoScope 4246 16-bit oscilloscope. The results of this test are presented in Fig. 5.27.

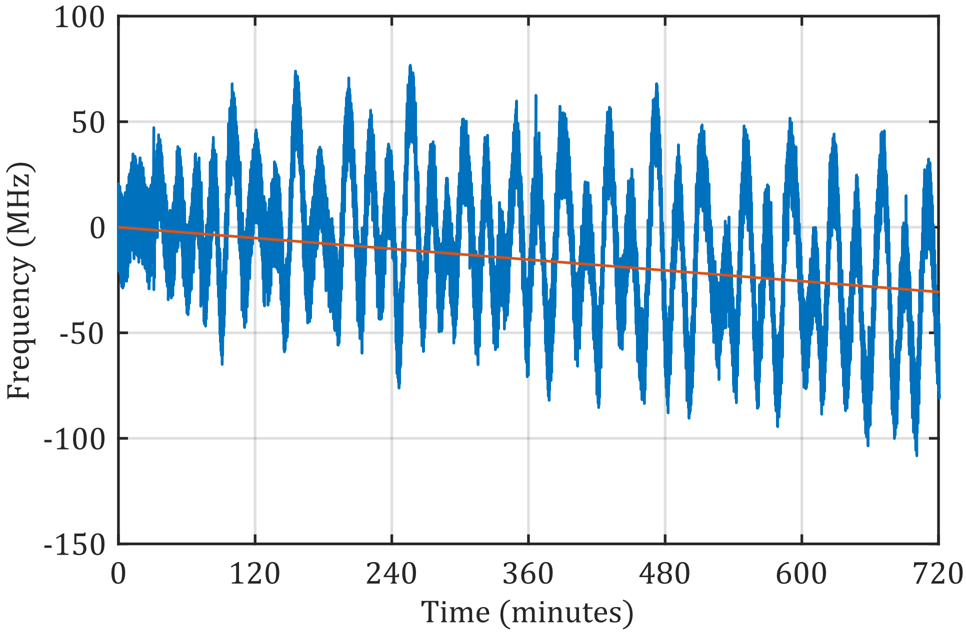

FIGURE 5.27 – VCSEL long term stability. Long term stability results of leaving VCSEL tuned to the middle of $F = 4 \rightarrow F' = 3$ for 12 hours. VCSEL response is presented in blue and a linear drift trend (obtained from the linear fit crossing through the origin) is presented in red.

From the results, it became apparent that the VCSEL features an oscillatory component with a frequency of 0.96 mHz (found using an FFT analysis) and an apparent long term drift of $\approx$ 30 MHz in 12 hours. The drift result is more than acceptable in our application of interest where pressure-broadened cells are used as it would take days to leave the transition of interest.

What is interesting here is the low-frequency component, which is believed to be the typical air conditioner cycle time in the laboratory, which would lead to ambient temperature dependence on the device.

For the purpose of testing this dependence, an ambient temperature monitoring setup was made that consists of a temperature sensor (TSIC 301) accurate to within

0.1 °C. This sensor was configured to measure the temperature every 30 seconds in 16 measurement bursts that were averaged to get higher instrument resolution. The TSIC 301 was operated with an Arduino RP2040 Connect microcontroller board and controlled with LabVIEW software.

The initial tests found little correlation between the ambient temperature and the laser frequency drift, with a Pearson coefficient [158] $\rho = 0.169$. The strongest correlation was found by lagging the temperature data by ≈ 5 minutes with respect to the spectroscopy data. The data was taken for 6 hours which is sufficient to resolve and capture many cycles of the oscillatory component.

The setup was modified to include a non-polarising beam splitter with a ratio of 50:50 to observe intensity changes through the reference cell on PD_S as well as through free space PD_M. This was done in order to decouple potential intensity noise contribution from frequency noise.

It was expected that by reading the voltage dropped across the thermistor with a high-resolution digital multimeter (DMM) to resolve μV level signals, a similar trend would be observed. The setup features two high-resolution DMMs (Agilent 3458A and Keithley Integra 2700) to monitor the voltage reference as well as the thermistor output. The redesigned setup is presented in Fig. 5.28.

The first test involving the new setup was to look at any potential correlation between intensity noise and frequency noise through the reference cell. The VCSEL was again tuned to the middle of $F = 4 \rightarrow F' = 3$ transition and left for 6 hours. This time, the correlation between spectroscopy data and the monitor was in very close agreement, reaching $\rho = 0.82$ suggesting intensity noise coupling. During this test, the VCSEL thermistor was sampled with a 6.5-digit multimeter (Keithley Integra 2700) at 4 samples per second. The results of this test are presented in Fig. 5.29.

The thermistor reading shows almost no perceivable drift in the frequency of the laser in the 6 hour period. There is also no sign of ambient temperature changes

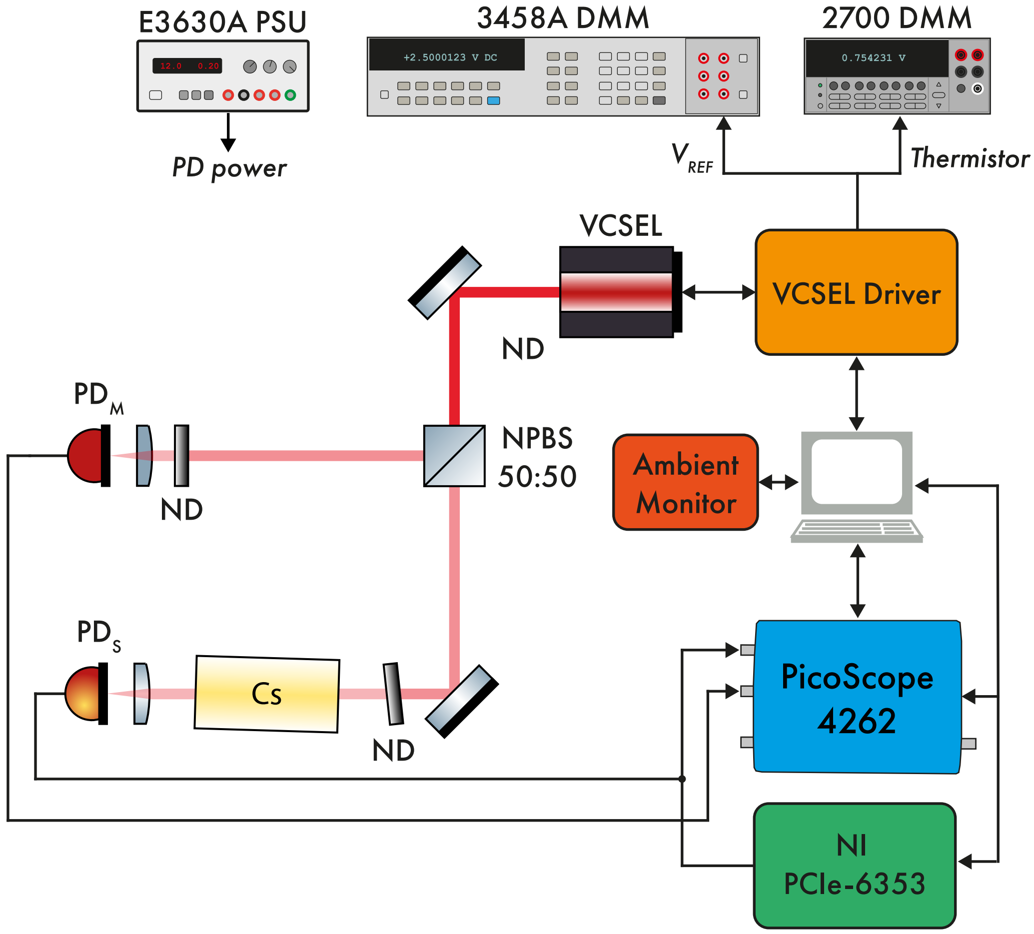

FIGURE 5.28 – Modified Cs spectroscopy setup from Fig. 5.24. NPBS: Non-polarising beam splitter, PD_M monitor photodetector, PD_S spectroscopy photodetector.

coupling into the setup. As was previously seen on the spectroscopy setup. The thermistor readout points to a peak frequency noise of $\approx \pm$ 4 MHz through the duration of the test. The correlation between the spectroscopy laser drift and the thermistor is very small $\rho = 0.09$. This points to intensity noise being the dominant factor.

As the intensity noise is directly caused by the injection current of the laser, the results obtained in Section 5.2.2.1 were compared to the spectroscopy results. The noise observed on the independent testing of the current source yielded only 2 MHz of total drift and no low frequency oscillatory components present in the spectroscopy data.

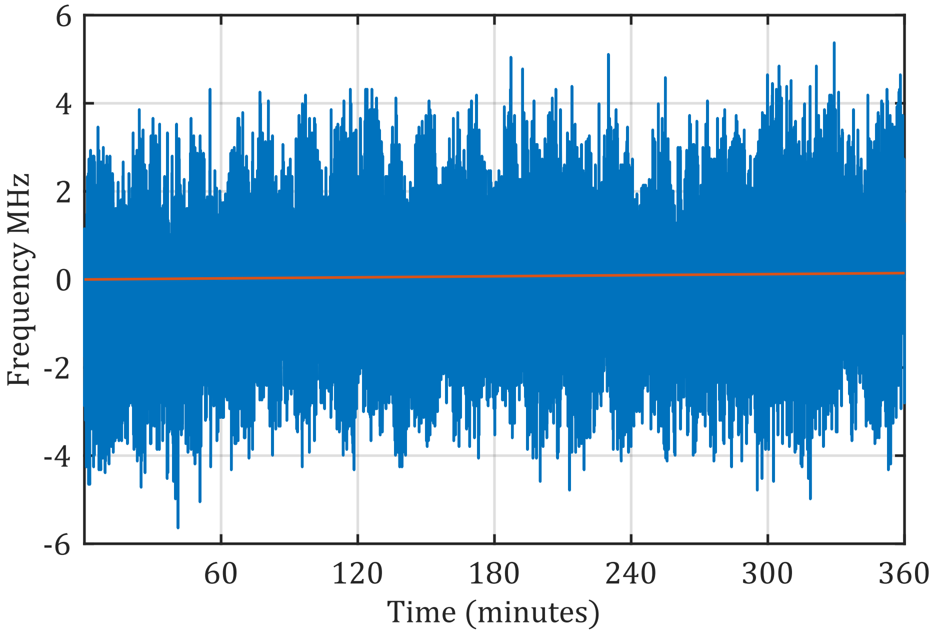

FIGURE 5.29 – VCSEL thermistor reading converted to frequency noise (in blue) during the 6 hours where the laser was tuned to the middle of $F = 4 \rightarrow F' = 3$ transition. The linear drift trend (obtained from the linear fit crossing through the origin) is presented in red.

The setup was modified to investigate this further by monitoring the voltage drop on the VCSEL with the Integra 2700 DMM used to monitor the thermistor. This would show any changes to the diode voltage drop with respect to ambient conditions. An ambient sensing board was also upgraded to include additional pressure and humidity sensors (HYT 221 [159] and MS5803-01BA [160]). These sensors are also capable of measuring ambient temperature. The modified sensor board was placed in close proximity to the VCSEL driver.

The VCSEL was again placed in the middle of $F = 4 \rightarrow F' = 3$ transition and left there for 6 hours while being monitored. The spectroscopy signal featured a very strong correlation of $\rho = 0.96$ with the VCSEL voltage drop. At the same time, it also exhibited strong anti-correlation with the ambient pressure of $\rho = -0.83$ and a small anti-correlation with humidity of $\rho = -0.25$. This leads us to believe that the VCSEL itself seems to be affected by the ambient conditions in the laboratory.

A shunt resistor was placed in series with the VCSEL, to monitor the injection current provided by the current source and monitoring it with a DMM. However, it was found that any attempt at doing so with this setup resulted in a vast amount of noise being injected into the system. This was not investigated further. It is thus ultimately unknown if the current source is the primary source of frequency noise or if the VCSEL itself is being somehow affected by the ambient pressure. However, the results obtained so far seem to show that the total laser frequency drift is not a problem for our application of interest.

5.3 Synopsis

This chapter focused on the development process of the custom low-noise photodetectors, as well as the custom VCSEL driving system.

The photodetectors achieved a spot noise of ≈ 51 nV/$\sqrt{\text{Hz}}$ at 100 Hz for 150 kV/A gain and ≈ 9 nV/$\sqrt{\text{Hz}}$ at a gain of 5 kV/A. The low noise contribution at low frequencies made it ideally suited for the SERF magnetometers covered in this thesis. These photodetectors are used in other magnetometry experiments in our group, due to their versatility in bandwidth and gain selection and ability to accept different photodiodes.

In order to replace the DBR laser source (used in portable SERF magnetometer) with the VCSEL a custom VCSEL driver was developed. The driver presents an RMS frequency noise of ≈ 11 MHz in the bandwidth of 0.1 Hz - 5 kHz and a long term drift of ≈ 30 MHz in 12 hours. Through the testing, it was revealed that an unknown low frequency component couples into the frequency drift of the laser and broadens it to ≈ 50 MHz for mid-term (≈ 1800 s) stability from ≈ 11 MHz obtained on a shorter timescale (100 s). This component was not found individually on either the current source or the TEC temperature controller driving the laser. A correlation was found between the ambient pressure in the lab and the trend of the drift, but no direct correlation to the low frequency component. This will require further investigation.

Chapter 6

VCSEL Investigation

The main disadvantage of single-transverse mode VCSELs is their modest optical power, with a typical performance of $\approx 500\ \mu$W for commercial devices. The power output is dictated by the oxide-aperture size which provides transverse optical confinement. Smaller aperture yields higher side-mode suppression however, at the same time increases the thermal resistance of the device, which leads to self-heating, limiting maximum optical power output [161].

The VCSELs that we had access to during the course of this PhD were all Vixar devices that have a maximum output optical power of $\approx 300\ \mu$W [148]. This power output is insufficient for transmission through the optically thick vapour in the SERF regime, without drastically reducing the beam size. Reducing the beam size leads to interaction with fewer atoms in the cell and reduced polarisation rate which negatively impacts the sensitivity.

As seen previously in Chapter 3, the parameter scan optimisation process revealed, that the portable Cs SERF magnetometer achieves the best sensitivity at relatively high optical powers of > 5 mW [82].

It was, however, found that good sensitivity can also be obtained at lower optical powers ≥ 1 mW while maintaining the same beam diameter. For this reason, it was decided to experimentally test the limits of the VCSELs to validate if they can be used for the Cs SERF magnetometer.

6.1 Optical power output

Before any other tests could be performed it was important to see how much optical power can be obtained from the devices and whether they can achieve the ≥ 1 mW power requirement found previously. The test setup for optical power estimation is presented in Fig. 6.1.

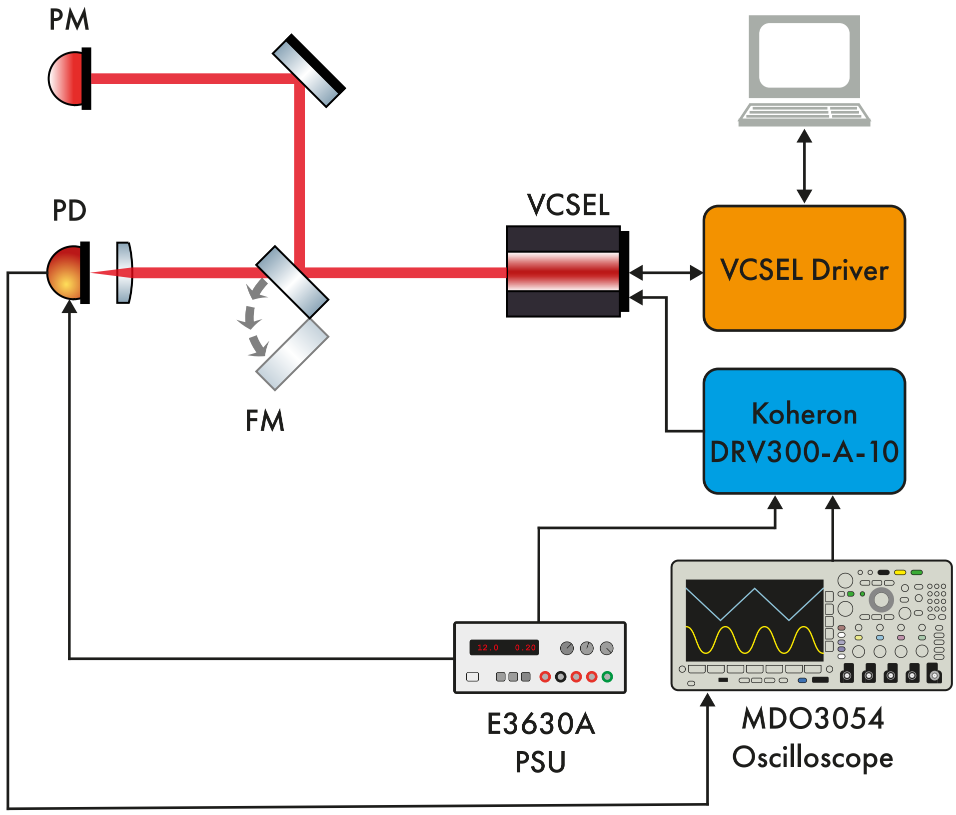

Figure 6.1 – VCSEL optical power test setup. The VCSEL temperature is controlled with the driver described in Section 5.2 while the current is provided with a low-noise current driver (Koheron DRV300-A-10) capable of outputting up to 10 mA of current. PM: Power meter (Thorlabs PM100D), PD: Photodetector from the setup in Fig. 5.28. It is powered by the E3630A power supply along with the DRV300. The signal is sampled by the oscilloscope (Tektronix MDO3054) which features a built-in function generator used to provide a modulation signal to the DRV300. The beam path is controlled with a flip mirror (FM) selecting between tests.

This setup is split into two parts controlled with a flip mirror to steer the beam into the photodetector or power meter. The power meter is used to find the static power while the photodiode is used to monitor the current modulation applied to the VCSEL. The modulation is applied through DRV300-A-10 driven by an MDO3054 oscilloscope with a built-in function generator.

The reason for using DRV300-A-10 for testing was the ease of controlling the DC current with a potentiometer and the ability to apply a modulation signal to the VCSEL from the MDO3054.

The temperature of the VCSEL was set to 55 °C and the output DC current on the driver was set to 1.5 mA. The modulation setting on DRV300 was set to 200 μA/V. The output of the MDO3054 function generator was set to 100 Hz sinewave and its amplitude was adjusted in small voltage increments. Channel 1 of the oscilloscope was used to monitor the function generator output and channel 2 was used to monitor the PD output. The values were plotted on XY mode of the oscilloscope to look for distortions in the output between the two. Any non-linearities would be shown as deviations from straight line plotted by the oscilloscope. Applying the modulation to the diode was done to limit the RMS current experienced by the diode, allowing for any non-linearities of the output to be shown without the risk of damaging the device.

After the modulation signal would cause distortion by going below the threshold current the DC value was increased in 200 μA steps. This process was repeated until distortion at the positive peaks was detected. The FM was then flipped to the other side to steer the beam to be incident on the power meter probe. The function generator output was turned off and the DC current value was set to 0 and increased in 100 μA increments to the same value where non-linearities were found using modulation. The resulting power response is presented in Fig. 6.2.

The power response results were somehow unexpected as it was anticipated that the nonlinearities would have been encountered right after 3 mA forward current (which is the absolute maximum rating of the diode [148]). It was found that the

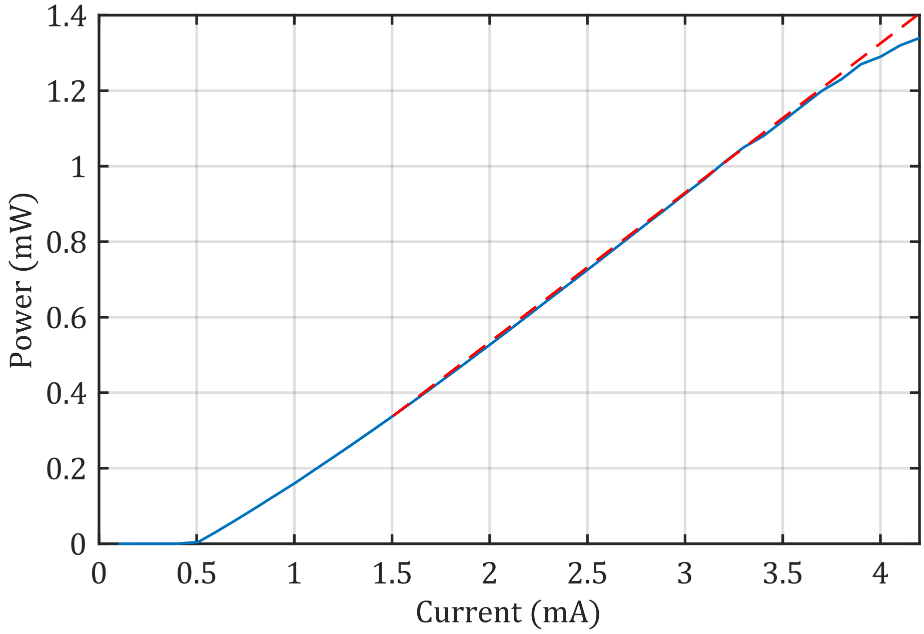

Figure 6.2 – VCSEL power response against forward current, the red dashed line shows the extrapolated linear response from 1.5 mA - 2 mA forward current region taken from the datasheet and extrapolated to 4.2 mA. The power response nonlinearity begins after 3.8 mA achieving a maximum power of ≈ 1.25 mW.

1 mW requirement can be met if the device is overdriven to at least 3.2 mA. It is however unknown how much lifetime degradation of the VCSEL this causes and would need to be investigated further.

6.2 Single mode operation

Although the optical power requirement has been met, it was important to estimate whether the device remains in single transverse mode operation and maintains its polarisation.

To test the single mode operation of the VCSEL, the setup seen in Fig. 6.1 was modified to include a wavemeter (Moglabs EWM) in place of the photodetector. The wavemeter used features a spectral resolution of 100 MHz. This resolution was expected to be enough for observing severe mode hopping or multimode operation. The setup is presented in Fig. 6.3.

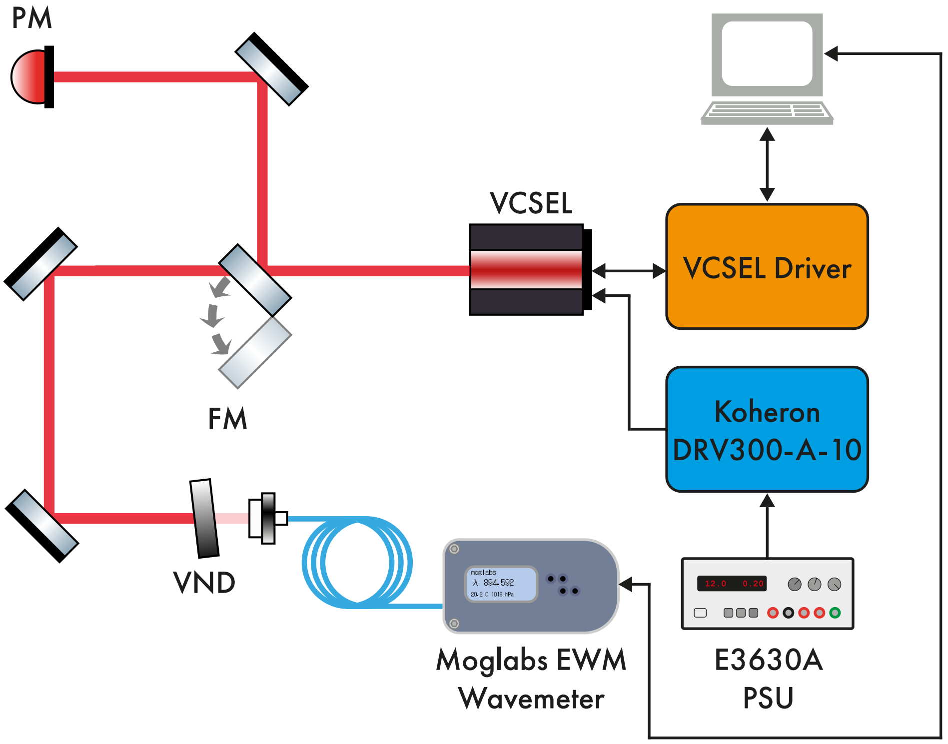

FIGURE 6.3 – VCSEL single mode test setup with a wavemeter. Setup from Fig. 6.1, has been modified to include a wavemeter in place of the photodetector. A variable neutral density (VND) filter (NDC-50C-4-B) was placed at the collimator input of the wavemeter fiber connection in order to control the intensity of input light as the VCSEL power is adjusted. The VND filter was placed at a slight angle to prevent optical feedback into the VCSEL.

The current was adjusted in 200 μA increments from 2 mA. The output power was monitored with the power meter. The VND filter was adjusted along with the increase in optical power so that the input of the wavemeter was not saturated. The results of this test are presented in Fig. 6.4. It can be seen that there is almost no difference between operation above the non-linear power point and below it. There are some signs of multimode operation (raised pedestal potentially caused by modes below the lasing threshold [162]) but no major mode splitting seems to have occurred.

To obtain a higher resolution of the VCSEL mode profile, the wavemeter was replaced with a Fabry-Pérot interferometer (FPI) (FPI 100) that features a free-spectral range (FSR) of 1 GHz and a finesse of 200 yielding a spectral resolution

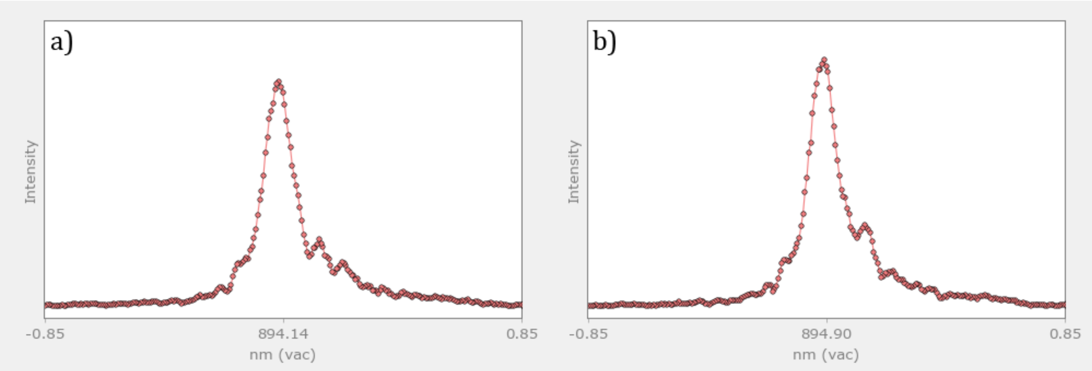

FIGURE 6.4 – VCSEL profile at a) 2 mA and b) 4 mA obtained from the wavemeter. The response looks almost identical, however, there are some signs of multimode operation at both injection currents.

of 5 MHz. The setup is presented in Fig. 6.5.

The setup uses a 4x telescope in order to minimise the beam size to fit the whole beam into the aperture of the optical isolator and FPI. The optical isolator (I-7090C-M) is used to prevent optical feedback from affecting the VCSEL that is supported by tilted VND filter. The VND filter was placed at the input to the FPI to control input intensity. The output from the photodiode was sampled by the oscilloscope with 50 Ω termination applied to increase the frequency response of the photodiode.

The current was this time adjusted in discrete values of 1, 2, 2.5, 3, 3.5 and 4.1 mA with the VND filter adjusted for each step. The results of selected settings of 1 and 4.1 mA covering free-spectral range are presented in Fig. 6.6, and a detailed response in Fig. 6.7.

It can be seen that the spectrum at 1 mA shows clear single transverse mode operation. The spectrum at 4.1 mA has been broadened and an effect of multimode operation below the lasing threshold is apparent. The expected Airy distribution [163] is skewed, which is believed to be the result associated with the imperfect alignment of the telescope that introduces astigmatism into the beam. The temperature of the VCSEL was then swept by $\pm$ 5°C but the spectrum lineshape remained the same.

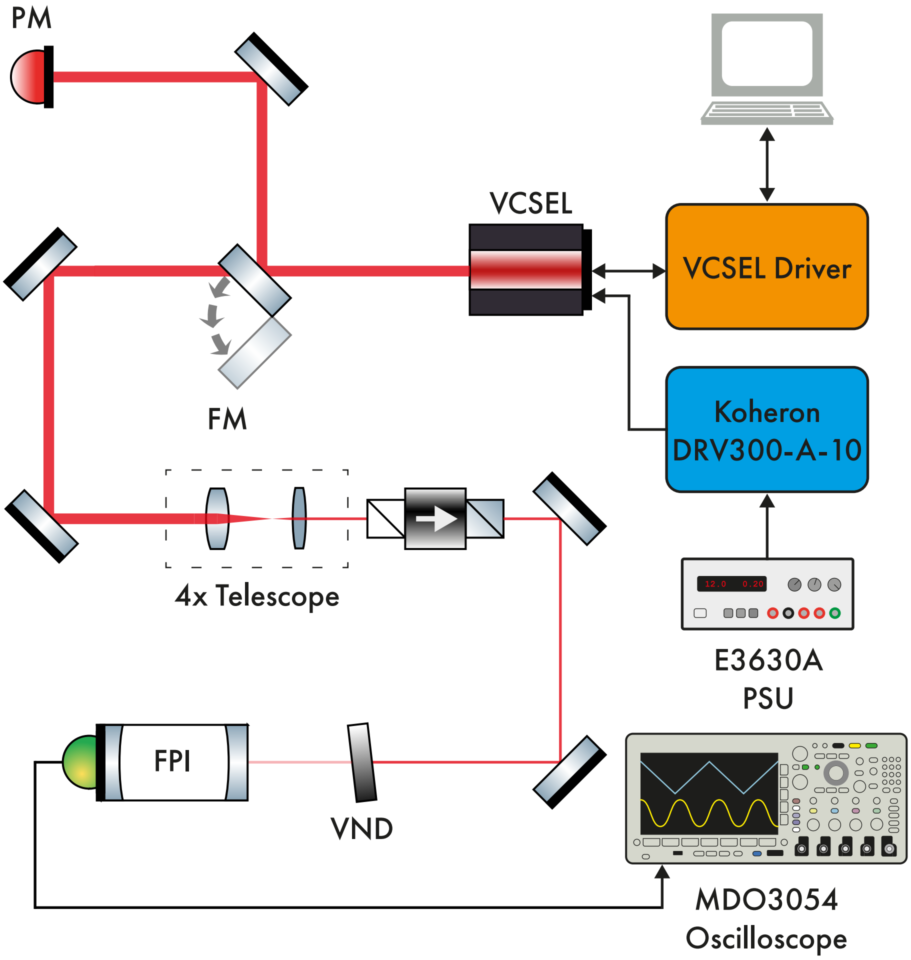

Figure 6.5 – VCSEL single mode test setup with FPI. Setup from Fig. 6.3, has been modified to replace the wavemeter with an FPI.

Although the spectrum reveals some indication of multimode operation, it is not severe and mostly manifests itself as a broadening of the spectrum. It is intended to operate the VCSEL at 3.5 mA because the overall linewidth has not been broadened too much and the modes are still below lasing threshold so most power is contained in the main mode. The level of broadening displayed here is also well below the pressure broadened linewidth of the cell ($\approx$ 3.4 GHz for D_1 transition), which makes the broadening introduced negligible.

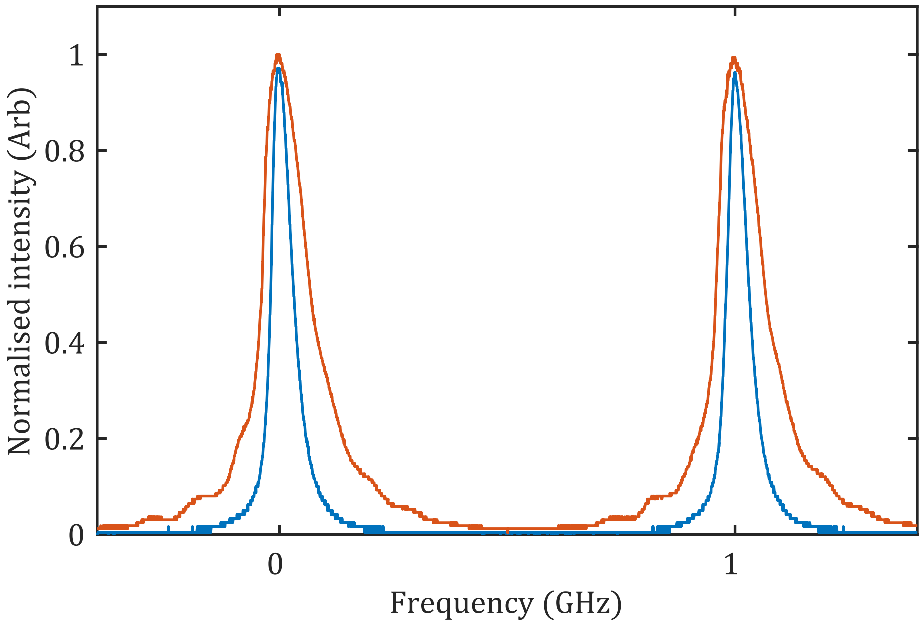

FIGURE 6.6 – FPI FSR spectrum of the VCSEL at 1 mA in blue and 4.1 mA in red.

6.3 Polarisation stability

An important aspect of coherent light sources used in optical experiments, such as optically pumped magnetometers is the ability to maintain a stable polarisation. In GSHE SERF magnetometers discussed in this thesis, circular polarisation is used to pump the atoms into orientation moment to bring the population into the dark state. The pumping efficiency depends on the degree of ellipticity of light. The deviation from a fully circular light source results in a reduction in the amplitude of the Hanle resonance negatively affecting sensitivity.

The VCSELs are likely to feature a sudden, and drastic change in output polarisation known as polarisation switching when their single mode operation changes to multimode [164, 165]. A setup was built to investigate the polarisation stability at different injection currents and is presented in Fig. 6.8.

The VCSEL injection current was set to 2 mA and the half-waveplate was adjusted until the ratio of transmitted and reflected light through the PBS was balanced.

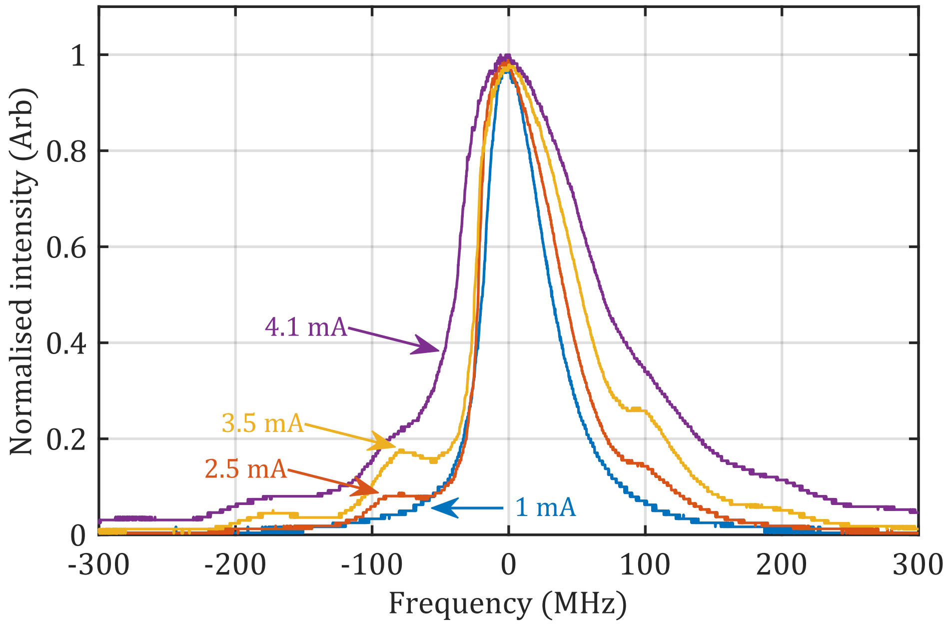

Figure 6.7 – FPI detailed spectrum of the VCSEL at different forward currents. 1 mA presented in blue, 2.5 mA presented in red, 3.5 mA in gold and 4.1 mA in purple.

The typical polarisation extinction ratio of 1000:1 for PBSs is believed to be sufficient to resolve major polarisation shifts that could occur on the VCSEL. The injection current was then increased in 100 μA steps until reaching 4.2 mA then the current was changed back to 2 mA and decreased in 250 μA increments until reaching 1 mA. The response of PD_T and PD_R has been recorded at each step. The result of this test is presented in Fig. 6.9.

It can be seen that no major polarisation shifts have occurred in the scanned injection current range. The change in the ratio of transmission to reflection is mostly linear from 1.25 mA up until $\approx$ 3.6 mA. There are three points at which the polarisation ratio changes direction, at 2.7 mA, 3.8 mA and later after 4 mA. It is important to note that the magnitude shift in polarisation detected is small and negligible to the SERF magnetometer operation. In addition, for parametric scans covered earlier in Section 3.5, the optical power would be kept at a constant maximum allowable setting.

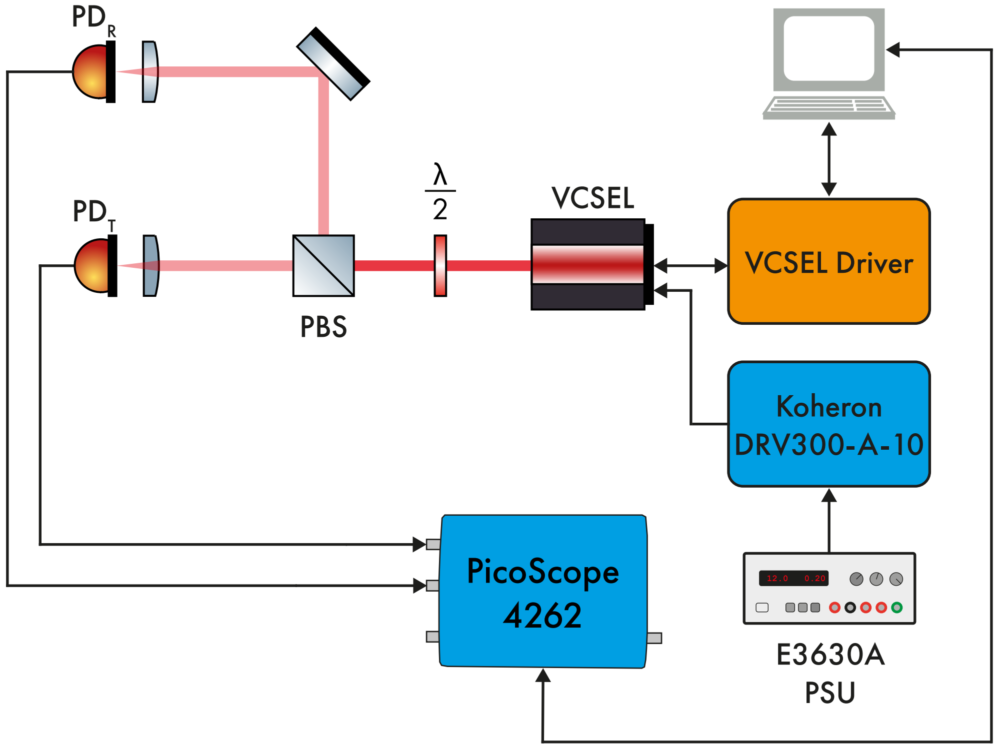

Figure 6.8 – VCSEL polarisation stability test setup. The setup consists of two identically configured photodetectors from Fig. 6.1 monitoring transmission PD_T and reflection PD_R through the polarising beam splitter (PBS). A half-waveplate ($\lambda/2$), mounted in a vernier rotation mount, is used to balance the amount of light transmitted and reflected through the PBS. The signals of PD_T and PD_R are monitored on the 16-bit oscilloscope (PicoScope 4262).

It has been previously mentioned that the DBR laser suffers from polarisation changes due to fiber not being aligned to the slow axis. To remedy this, the fiber was placed in the insulated box to minimise this effect as covered in Subsection 3.1.3. For this reason, it was decided to compare long term polarisation stability of both devices.

The injection current of the VCSEL was set to 3.5 mA in order to achieve an output optical power of $\approx$ 1.13 mW and the PBS was re-balanced with a half-waveplate. The setup was left in this configuration and data was sampled for 12 hours overnight.

After that, the VCSEL was replaced with the DBR laser and the optical power was set to 5 mW, which is the typical operational point for the magnetometer achieving

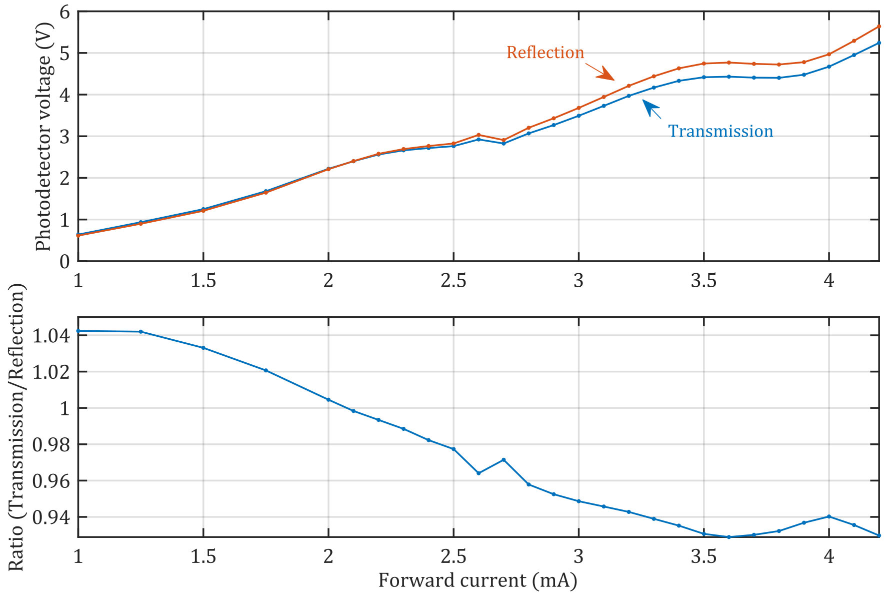

FIGURE 6.9 – VCSEL polarisation stability test results. The PD_T and PD_R individual responses are presented at the top, where PD_R response is presented in red and PD_T is presented in blue. The bottom plot shows the difference between transmission and reflection ratios balanced at 2 mA.

the best sensitivity. An 0.5 ND filter was added in front of the half-waveplate to not saturate the photodetectors. The waveplate was then used to balance the PBS and similarly, the setup was left in this configuration and data was sampled for 12 hours overnight. The results of this test are presented in Fig. 6.10.

The DBR laser polarisation exhibits major polarisation shifts up to 65 % and on some occasions flipping the polarisation around completely. The VCSEL is affected to a much lower degree, exhibiting less than 0.01 % polarisation shift in 12 hours. The apparent VCSEL polarisation shift can probably be attributed to the changes in properties of the PBS with temperature and not the VCSEL itself. The temperature in the laboratory is kept at $\approx$ 21 °C and kept stable to within $\pm$ 1 °C.

It is believed that the DBR laser performance could have been much better if the integrated fiber would have been aligned to the fast axis, presenting greater resistance to the environmental effects.

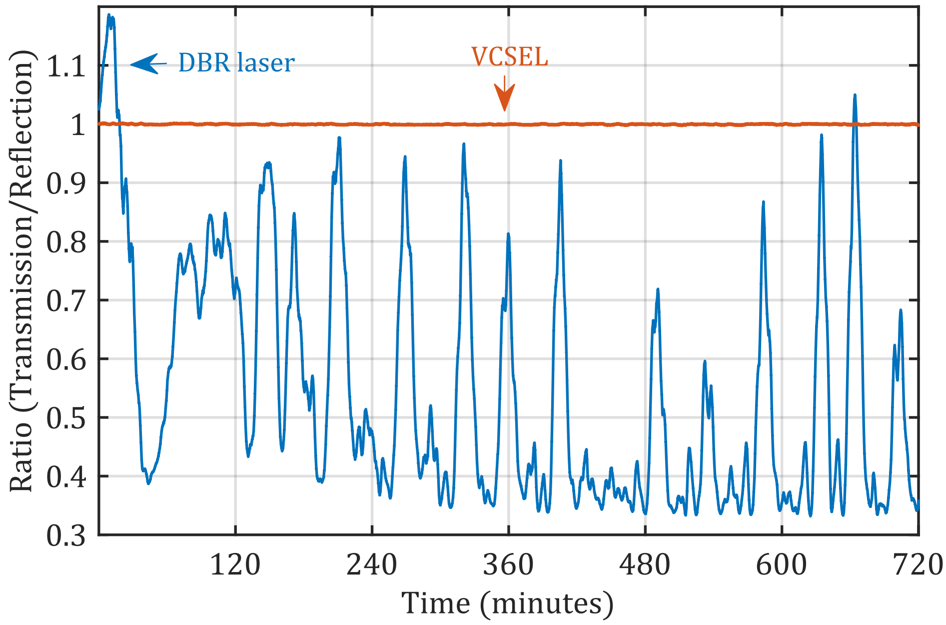

Figure 6.10 – Polarisation drift in 12 hours for VCSEL and the DBR laser. DBR laser is presented in blue and VCSEL in red. The DBR laser exhibits major polarisation shifts while VCSEL is not much affected.

6.4 Relative intensity noise

The tested VCSEL has shown that it can be overdriven to achieve desired optical power output with a slight broadening of linewidth and an ability to maintain its polarisation. What was left to check was the RIN and compare it to the DBR laser currently used in the experiment.

As seen in Section 3.3 one of the factors limiting magnetometer sensitivity is the intensity noise of the laser. The intensity noise is typically caused by the noise of current sources driving the lasers and the laser's own quantum noise. A figure of merit for the intensity noise of the laser is the relative intensity noise, which is a function of intensity noise normalised by its average optical power. A test setup for measuring the RIN of both VCSEL and the DBR currently used in the experiment is presented in Fig. 6.11.

In this setup, the VCSEL was fully controlled by the VCSEL driver covered in

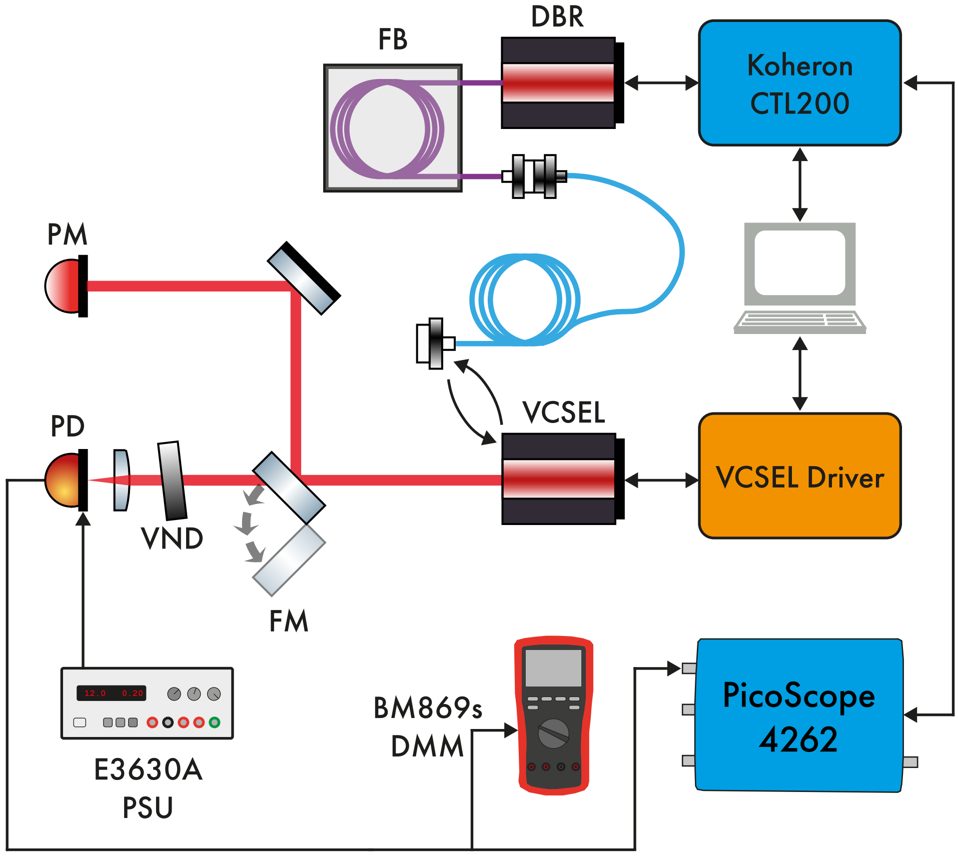

Figure 6.11 – RIN estimation test setup. The VCSEL is fully operated from the VCSEL driver unit covered in the previous section. It provides 3.5 mA of injection current to the VCSEL. The VCSEL can be swapped with the fiber collimator (CFC11A-B) of the DBR laser onto the same post.

Section 5.2. It was set to provide a constant 3.5 mA of injection current to the VCSEL and to keep its temperature to 50 °C. The optical output power of the VCSEL was measured with a power meter used previously and found to be $\approx$ 1.13 mW. The signal was then incident on the previously used photodetector PD. The gain on the PD was adjusted along with the attenuation of VND filter to obtain the maximum signal without saturating the detector output.

The PD was simultaneously plugged into an AC-coupled 16-bit oscilloscope (PicoScope 4262) and a high resolution 5.5-digit multimeter (Brymen BM869s) to measure the DC voltage level of the signal that the scope data is normalised against. The setup also features the DBR laser currently used in the Cs SERF experiment for comparison against the VCSEL.

After the VCSEL RIN measurement was performed, the VCSEL was replaced with the DBR laser's fiber collimator by mounting it to the same post to ease the re-alignment process. The DBR laser was operated at a nominal temperature of 23 °C and the injection current was set to provide an output power of ≈ 1.13 mW to match the optical power of the VCSEL. The RIN measurement results for both the DBR laser and VCSEL are presented in Fig. 6.12.

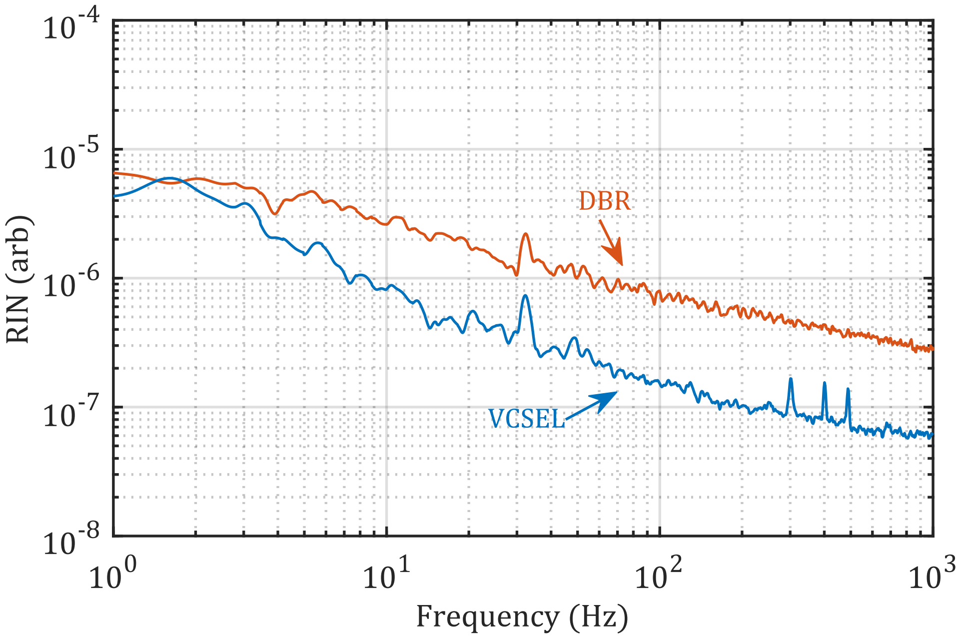

FIGURE 6.12 – RIN results for the DBR laser and the VCSEL, both providing an optical power of ≈ 1.13 mW. The VCSEL exhibits ≈ 3 times lower RIN after 10 Hz and ≈ 6 times lower RIN at a typical modulation frequency (183 Hz). The peaks at 20 and 31 Hz are believed to be coupled through the air-conditioner vibration discussed in Chapter 3, which affects the VND filter. The peaks at 300, 400 and 458 Hz are of unknown origin.

The results show that the VCSEL exhibits 3 - 6 times lower RIN compared to the DBR laser. Improving both the performance in the magnetometer bandwidth of interest as well as improving sensitivity. The performance displayed here would without a doubt improve the performance of the magnetometer at lower optical powers. The move from the DBR to a more compact, higher efficiency laser device would greatly improve the SWaP of the whole system.

It is not known how much is the VCSEL lifetime affected by the increase in injection current. The VCSEL used for the experiments was previously used in another magnetometer sensor head (operated at nominal injection current) for about a year before being overdriven and tested here. The VCSEL has been operated at 3.5 mA for about 4 months now, with no changes to its operational parameters or performance.

6.5 Synopsis

This chapter focused on the investigation of the VCSEL diodes and their potential use as a replacement for the DBR laser used in portable SERF magnetometer described in Section 3.5. Through the investigation, the VCSEL has shown superiority to the DBR laser in almost every way. It is expected that in the future the VCSEL will be used in place of the DBR laser for the portable SERF magnetometer. This should help reduces the intensity noise and improve polarisation stability, while at the same time reducing the SWaP of the system. There is however a trade-off between the power output of the VCSEL and the DBR laser. It is however believed that the advantages in other areas, such as lower intensity noise outweigh the lower maximum output power of the VCSEL. The VCSEL has not been yet tried in the portable magnetometer but will be in the future.

Chapter 7

Conclusions and Outlook

The work undertaken in this thesis focused on the design of two spin-exchange relaxation-free (SERF) magnetometers, each utilising a different alkali species, with a primary focus on the development process of their associated instrumentation. The Rb SERF magnetometer, which is a large-scale experiment built on an optics table, served its purpose as an investigation into a single-beam, absorptive measurement magnetometer relying on the ground-state Hanle effect as its detection mechanism. The Rb SERF magnetometer, through specially designed custom instrumentation, achieved a sensitivity of ≈ 24.7 fT/$\sqrt{\text{Hz}}$ (at 10 Hz) and ≈ 18.5 fT/$\sqrt{\text{Hz}}$ (at 60 Hz). This sensitivity is believed to be limited by the coil driver output. By optimising the maximum output current range (or bandwidth of the driver) higher sensitivity could potentially be achieved. The thermal noise of the mu-metal shield, which is specified to be ≈ 16 fT/$\sqrt{\text{Hz}}$ at frequencies below 50 Hz and ≈ 10 fT/$\sqrt{\text{Hz}}$ after 1 kHz is believed to be the next dominant source of noise, potentially limiting the performance. When the shield noise becomes the next primary noise source, it can be replaced with a mu-metal shield with a ferrite inner layer to further improve the sensitivity. With the current sensitivity, the experiment could be used for investigating low magnetic field applications, such as looking at nuclear magneto resonance (NMR) in liquid samples, which is an ongoing discussion with colleagues at Strathclyde.

The lab-based experiment also served as a test bed for different design aspects, such as the use of 3D printed materials for its oven structure, custom low inductance heaters that produce a minimal external magnetic field, the use of separate signal and monitor photodiode to cancel common mode intensity noise in the system, and specially designed instrumentation that is common to both experiments. The ability to programmatically control most of the operational parameters of the experiment allowed for the use of optimisation algorithms to quickly find the optimal magnetometer operational point. This capability allowed us to gauge improvements from optimising the physical setup.

The custom photodetectors developed over the course of this thesis feature selectable gain and bandwidth, an adjustable bias and an ability to accept different photodiodes. This makes the design very versatile and not limited only to SERF magnetometer applications. The photodetectors as well as their transimpedance amplifier (TIA) architecture are now widely used in our group as a low noise light detection source. The performance of the custom photodetectors has shown an ability to be limited only by the photon shot noise and light intensity noise of the laser under every operational condition for both experiments. The results described in this thesis prove their usefulness as a detection mechanism for SERF magnetometry applications. One aspect that could be added in the future is the pre-amplified alternating current (AC) coupled output on the photodetectors, which would remove the need for an external pre-amplifier used for magnetometer noise estimation.

The total electronic and photon shot noise contribution of the combined monitor and signal photodetectors was found to be very small 88.2 nV/$\sqrt{\text{Hz}}$ (6.2 fT/$\sqrt{\text{Hz}}$). However, this contribution could in the future be further reduced. Self-balancing detection with matched transistors used as current splitting diodes would minimise the 3 dB penalty imposed by two uncorrelated devices [88].

During the duration of the project work, custom, ultra-low noise, bipolar current sources were developed for driving nulling coils in SERF experiments. The low current source (LCS) can be configured to provide up to ± 50 mA and the high current source (HCS) provides up to ± 250 mA of current. The devices both feature ppb noise performance and their current range complement each other by overlapping the gap between current ranges. They feature digital control of current on three independent channels, in both directions with 16-bit resolution. The design features a common digital/signal conditioning chain for both devices. This allows for user customisation of aspects such as bandwidth, noise or stability. This ability was demonstrated by reconfiguring the maximum output current capability which allowed the device to alter its maximum output current while maintaining the dynamic range. These user customisations of the current range and bandwidth allow for the device to be tailored to a particular coil geometry or application.

The devices were subjected to a variety of tests, ranging from noise performance to stability. The LCS configured to provide 10 mA achieved 146 pA/$\sqrt{\text{Hz}}$ at 10 Hz, demonstrating a relative noise of 15 ppb/$\sqrt{\text{Hz}}$. The HCS configured to provide 250 mA achieved 4.1 nA/$\sqrt{\text{Hz}}$ at 10 Hz, demonstrating a relative noise of 16 ppb/$\sqrt{\text{Hz}}$. Due to the use of a common signal chain, both devices feature a narrow 1/f region with a corner frequency of approximately 1 Hz. This makes both devices a good fit for generation of low noise magnetic fields for OPM application. Another benefit of using common architecture for both devices is that their stability performance is almost identical. Featuring ppm stability well suited for coil control in most OPM applications that primarily rely on short term stability.

It was also revealed through the accuracy tests, that the coil driver does not require to be calibrated in order to provide adequate performance. It was however shown, that for applications that required high accuracy a calibration can be performed and allow for monotonic accuracy of ± 1 least significant bit (LSB) over its full range.

The coil drivers in both LCS and HCS configurations are widely used high-performance current sources in the magnetometry group for all experiments including both SERF experiments, RF magnetometers and FID magnetometers. In the future, the low-noise current source could be further expanded to target higher currents of up to 1 A in order to cover more kinds of coil geometries. It would also be beneficial to feature an on-board USB isolator rather than having to rely on externally plugged isolators.

The knowledge gathered from the design of the Rb SERF magnetometer was used in the design of the portable Cs SERF magnetometer. The portable SERF experiment was miniaturised with the use of small, mm-scale optics, 3D-printed structures that house optics and the cell, PCB bi-planar field nulling coils and an external transimpedance amplifier based around the design of the custom photodetector. The coil driver designed in Chapter 4 was also used for the generation of nulling fields for the experiment. The ability to modify the current range of the coil driver was useful for the portable experiment, where the coils with different (to the lab-based SERF magnetometer) field to current ratios were used. The miniaturisation of SERF magnetometer allows it to be used for biomedical applications. Testing for human biomagnetic signals was performed during field trials at Nottingham University, and a human heartbeat was successfully detected. Details of this can be found in Rachel Dawson's thesis.

Both lab-based and portable magnetometers have highlighted problems with a commercially off-the-shelf DBR fiber-coupled laser, which exhibits polarisation drift and intensity noise above the photon shot noise limit of the detectors. An alternative laser source based on vertical-cavity surface-emitting lasers (VCSELs) was identified and tested beyond its rated capabilities, displaying better performance in almost every regard in comparison to the DBR with the main improvement in polarisation stability (up to 6500 times better stability) and relative intensity noise (up to 6 times lower noise).

A custom low-noise VCSEL driver was developed to replace the DBR laser source used for portable magnetometer with the VCSEL. The laser driver offers very low root-mean-square (RMS) current noise, corresponding to a laser frequency noise of $\approx$ 11 MHz in the bandwidth of 0.1 Hz -5 kHz. The driver features a long term drift of $\approx$ 30 MHz in 12 hours. Testing the driver, revealed an unknown low frequency component, propagating as a frequency drift of the laser. This drift broadens the effective linewidth of $\approx$ 50 MHz on a timescale of 1800 s. It was shown that the component is not present on either the thermo-electric cooler (TEC) temperature controller or the current source driving the laser. Ambient monitoring of the laboratory was implemented and a correlation was found between the ambient pressure in the lab and the trend of the drift, however, no direct correlation to the low frequency component was found. This phenomenon will require further investigation. The low frequency component encountered is not a limitation at present for magnetometry applications that use pressure-broadened cells. As it stands replacing the DBR laser source with a VCSEL driven by the custom driver would improve the intensity noise and polarisation stability.

In the future, it would be good to add a current modulation input, which could be used for laser locking or pulse laser control, required for some applications, such as Bell-Bloom type magnetometers.

The VCSEL driver developed is currently used in a total field magnetometer sensor developed in our group. The device is an improvement over a laser driver that was previously used. It is planned to also replace the fiber-coupled DBR laser in the portable SERF magnetometer with the VCSEL and use it with the newly developed VCSEL driver.

Another aspect that was limiting the performance of the lab-based magnetometer was the 16-bit DAQ cards used for both experiments, where the noise floor of the acquisition system was much higher than the photodetector noise floor. In the future, a custom portable version of the DAQ would be developed in order to further reduce the SWaP of the whole system. When that is completed, all of the other design elements could be combined into a portable system with separate sensor head and control electronics.

Appendices

Appendix A

Circuit simulation methodology

Designs covered in this thesis have been simulated using the following SPICE software packages:

- **LTspice** (Linear Technologies (now part of Analog Devices))
- **TINA-TI** (Texas Instruments)

These tools were used for both the AC and DC analysis of the circuits developed during the duration of this project.

Appendix B

VCSEL driver schematic

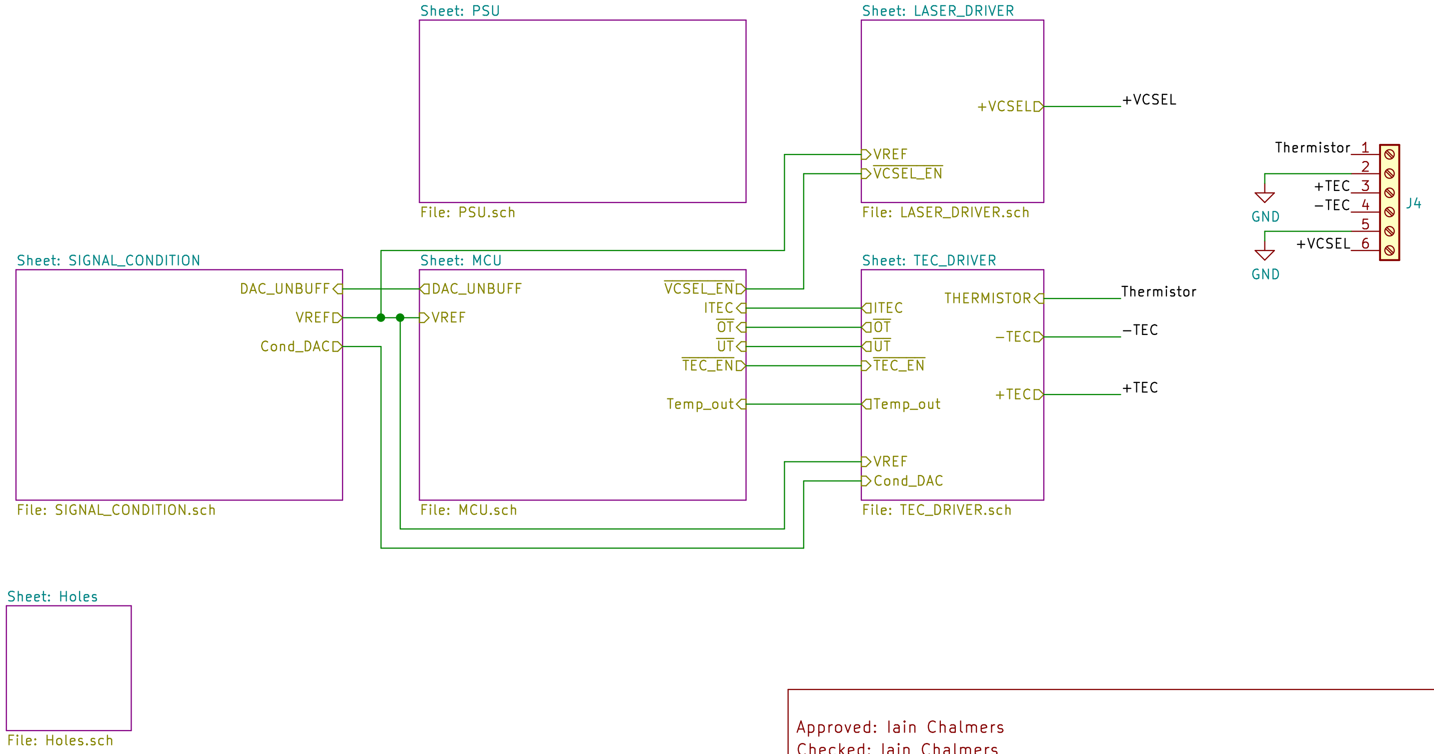

Approved: Iain Chalmers
Checked: Iain Chalmers
Designed: Marcin Mrozowski
Strathclyde University
Sheet: /
File: VCSEL_driver.sch
Title: VCSEL Driver
Size: A4 Date: 2022-02-08 **Rev: 2.0.0**
KiCad E.D.A. kicad (5.1.10)-1 Id: 1/7

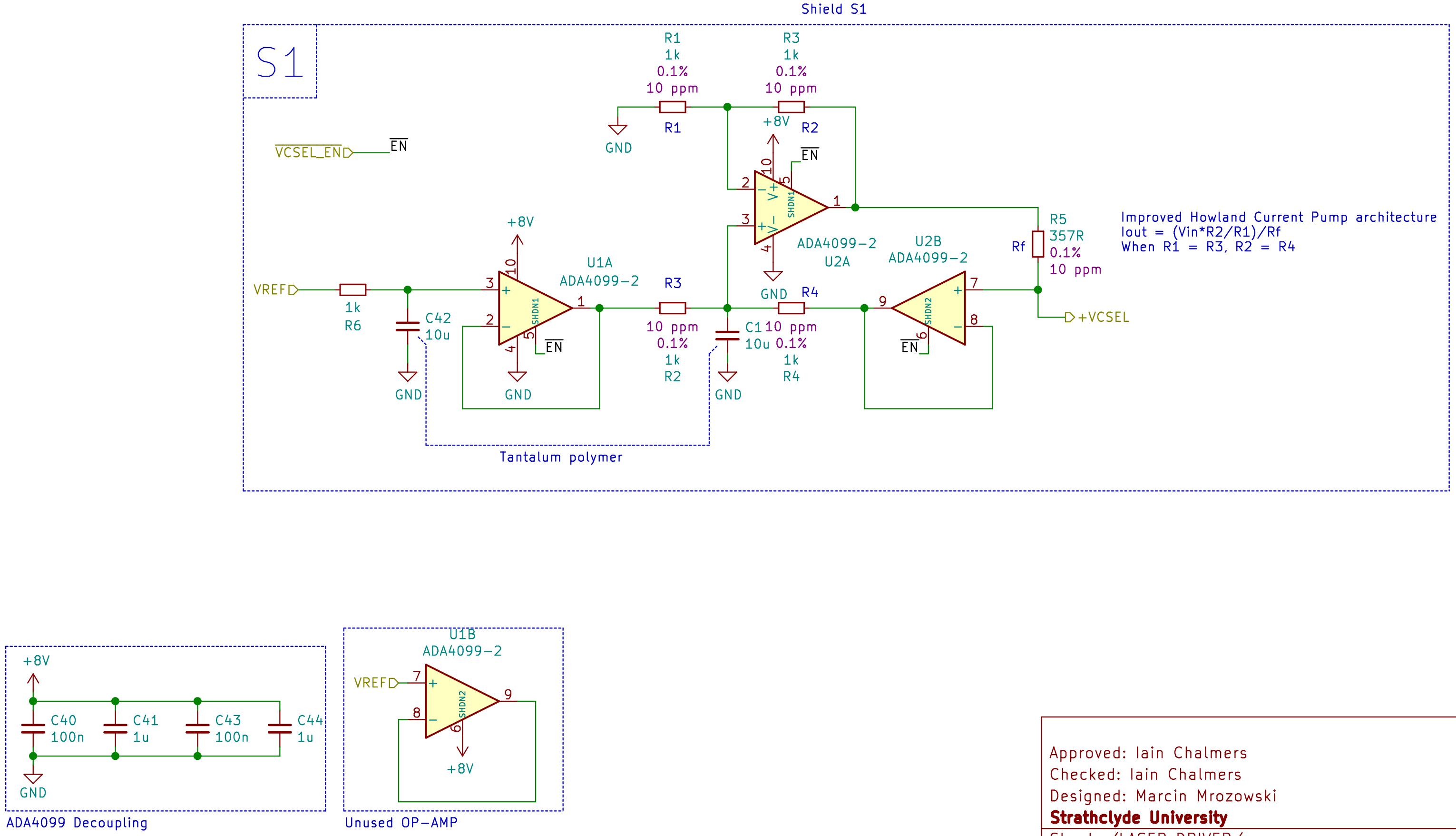

Approved: Iain Chalmers
Checked: Iain Chalmers
Designed: Marcin Mrozowski
Strathclyde University
Sheet: /LASER_DRIVER/
File: LASER_DRIVER.sch

Title: VCSEL Driver

Size: A4 | Date: 2022-02-08 | **Rev: 2.0.0**
KiCad E.D.A. kicad (5.1.10)-1 | Id: 2/7

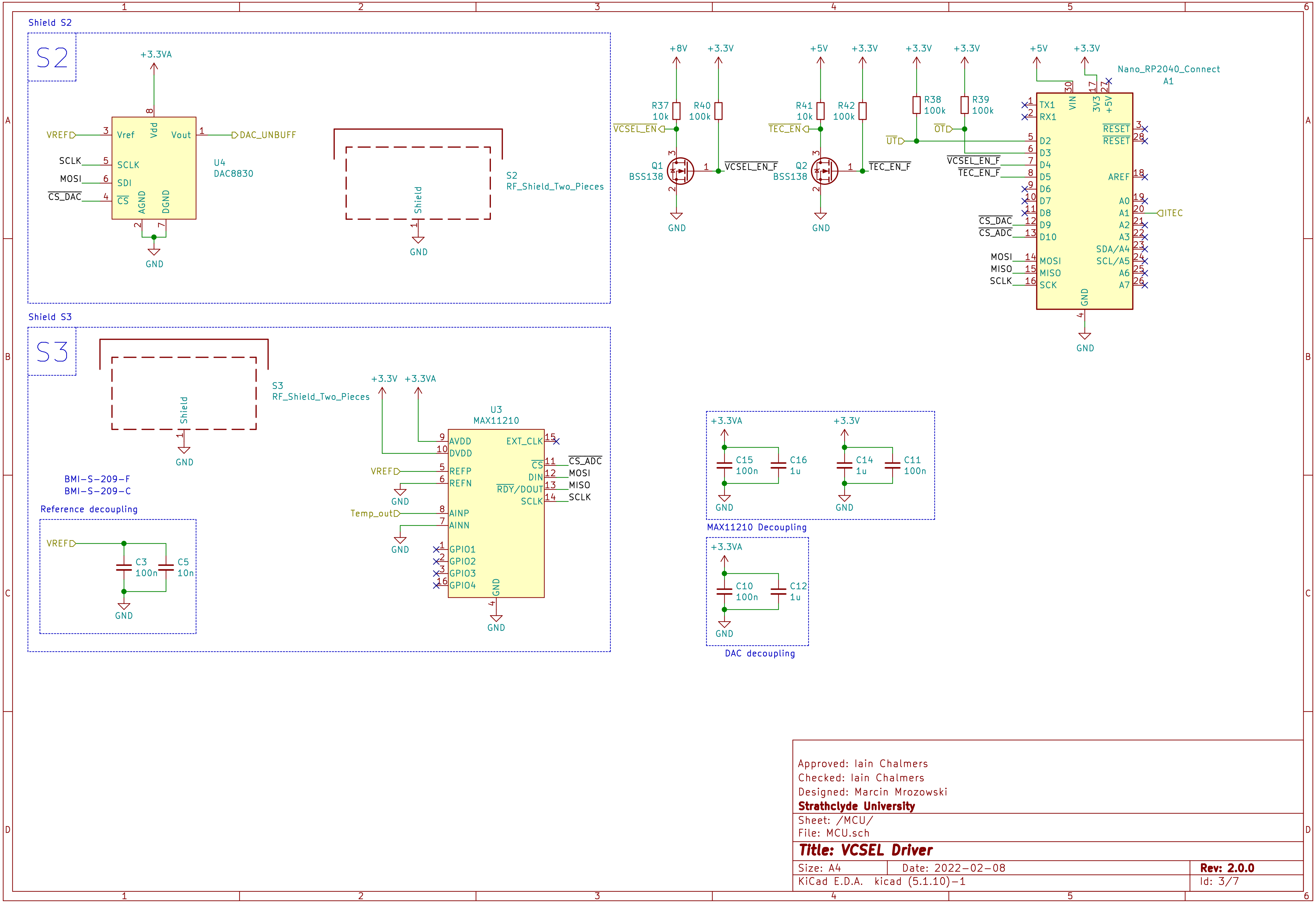
Shield S2
S2
+3.3VA
VREF
SCLK
MOSI
CS_DAC
Vref
Vdd
Vout
SCLK
SDI
CS
AGND
DGND
DAC_UNBUFF
U4
DAC8830
GND
S2
RF_Shield_Two_Pieces
Shield
GND
Shield S3
S3
S3
RF_Shield_Two_Pieces
Shield
GND
BMI-S-209-F
BMI-S-209-C
Reference decoupling
VREF
C3
100n
C5
10n
GND
+3.3V
+3.3VA
U3
MAX11210
AVDD
DVDD
REFP
REFN
AINP
AINN
GPIO1
GPIO2
GPIO3
GPIO4
EXT_CLK
CS
DIN
RDY/DOUT
SCLK
GND
CS_ADC
MOSI
MISO
SCLK
VREF
Temp_out
GND
+8V
+3.3V
R37
10k
R40
100k
VCSEL_EN
Q1
BSS138
VCSEL_EN_F
GND
+5V
+3.3V
R41
10k
R42
100k
TEC_EN
Q2
BSS138
TEC_EN_F
GND
+3.3V
+3.3V
R38
100k
R39
100k
UT
OT
+5V
+3.3V
Nano_RP2040_Connect
A1
VIN
3V3
+5V
TX1
RX1
D2
D3
D4
D5
D6
D7
D8
D9
D10
MOSI
MISO
SCK
RESET
RESET
AREF
A0
A1
A2
A3
SDA/A4
SCL/A5
A6
A7
GND
VCSEL_EN_F
TEC_EN_F
CS_DAC
CS_ADC
MOSI
MISO
SCLK
ITEC
GND
+3.3VA
+3.3V
C15
100n
C16
1u
C14
1u
C11
100n
GND
MAX11210 Decoupling
+3.3VA
C10
100n
C12
1u
GND
DAC decoupling
Approved: Iain Chalmers
Checked: Iain Chalmers
Designed: Marcin Mrozowski
Strathclyde University
Sheet: /MCU/
File: MCU.sch
Title: VCSEL Driver
Size: A4
Date: 2022-02-08
Rev: 2.0.0
KiCad E.D.A. kicad (5.1.10)-1
Id: 3/7

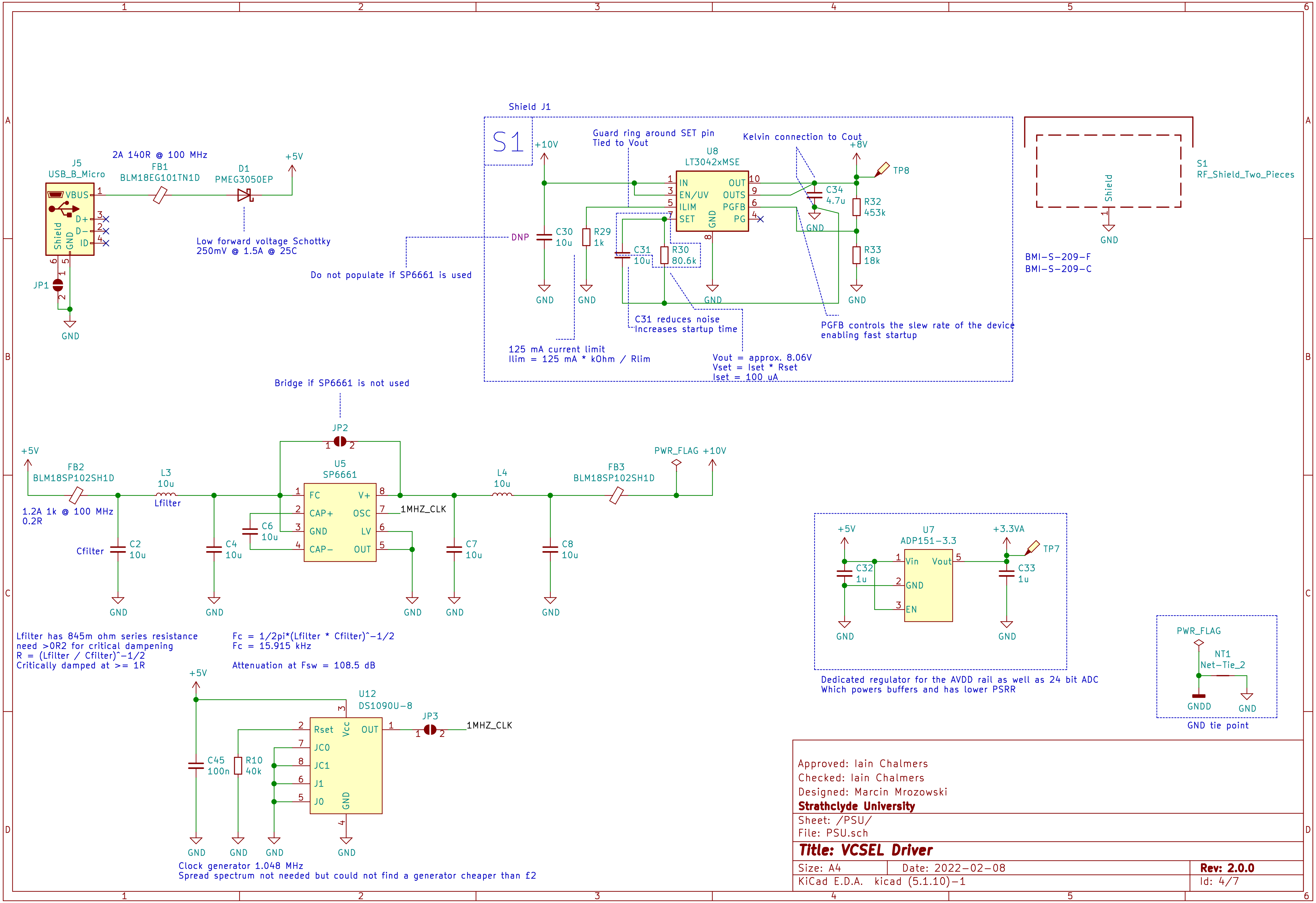

Shield J1
S1
+10V
Guard ring around SET pin
Tied to Vout
Kelvin connection to Cout
+8V
U8
LT3042xMSE
IN
EN/UV
ILIM
SET
GND
OUT
OUTS
PGFB
PG
TP8
C34
4.7u
R32
453k
R33
18k
DNP
C30
10u
R29
1k
C31
10u
R30
80.6k
GND
Do not populate if SP6661 is used
C31 reduces noise
Increases startup time
PGFB controls the slew rate of the device
enabling fast startup
125 mA current limit
Ilim = 125 mA * kOhm / Rlim
Vout = approx. 8.06V
Vset = Iset * Rset
Iset = 100 uA
S1
RF_Shield_Two_Pieces
Shield
BMI-S-209-F
BMI-S-209-C
J5
USB_B_Micro
VBUS
D+
D-
ID
Shield
GND
JP1
2A 140R @ 100 MHz
FB1
BLM18EG101TN1D
D1
PMEG3050EP
+5V
Low forward voltage Schottky
250mV @ 1.5A @ 25C
Bridge if SP6661 is not used
JP2
U5
SP6661
FC
CAP+
GND
CAP-
V+
OSC
LV
OUT
1MHZ_CLK
+5V
FB2
BLM18SP102SH1D
1.2A 1k @ 100 MHz
0.2R
L3
10u
Lfilter
Cfilter
C2
10u
C4
10u
C6
10u
C7
10u
L4
10u
C8
10u
FB3
BLM18SP102SH1D
PWR_FLAG +10V
Lfilter has 845m ohm series resistance
need >0R2 for critical dampening
R = (Lfilter / Cfilter)^-1/2
Critically damped at >= 1R
Fc = 1/2pi*(Lfilter * Cfilter)^-1/2
Fc = 15.915 kHz
Attenuation at Fsw = 108.5 dB
+5V
U7
ADP151-3.3
Vin
GND
EN
Vout
+3.3VA
TP7
C32
1u
C33
1u
Dedicated regulator for the AVDD rail as well as 24 bit ADC
Which powers buffers and has lower PSRR
PWR_FLAG
NT1
Net-Tie_2
GNDD
GND
GND tie point
U12
DS1090U-8
Rset
JC0
JC1
J1
J0
Vcc
OUT
GND
JP3
1MHZ_CLK
C45
100n
R10
40k
Clock generator 1.048 MHz
Spread spectrum not needed but could not find a generator cheaper than £2
Approved: Iain Chalmers
Checked: Iain Chalmers
Designed: Marcin Mrozowski
Strathclyde University
Sheet: /PSU/
File: PSU.sch
Title: VCSEL Driver
Size: A4
Date: 2022-02-08
Rev: 2.0.0
KiCad E.D.A. kicad (5.1.10)-1
Id: 4/7

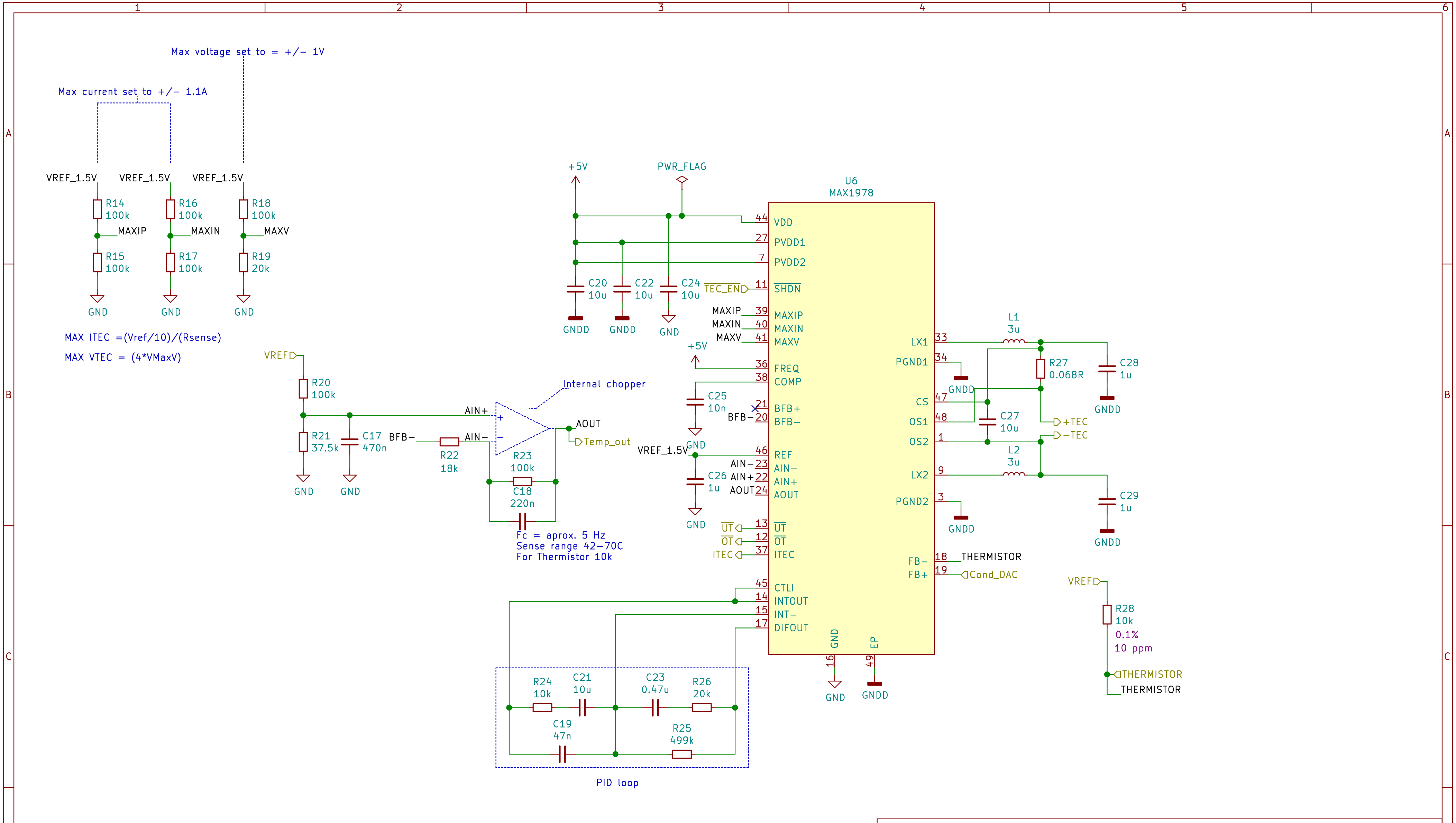

Approved: Iain Chalmers
Checked: Iain Chalmers
Designed: Marcin Mrozowski
Strathclyde University
Sheet: /TEC_DRIVER/
File: TEC_DRIVER.sch

Title: VCSEL Driver

Size: A4 Date: 2022-02-08 **Rev: 2.0.0**
KiCad E.D.A. kicad (5.1.10)-1 Id: 5/7

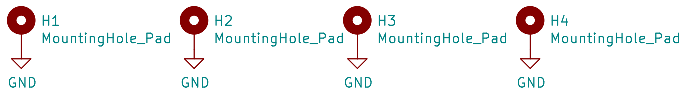

Approved: Iain Chalmers
Checked: Iain Chalmers
Designed: Marcin Mrozowski
Strathclyde University
Sheet: /Holes/
File: Holes.sch

Title: VCSEL Driver

Size: A4	Date: 2022-02-08	**Rev: 2.0.0**
KiCad E.D.A. kicad (5.1.10)-1		Id: 6/7

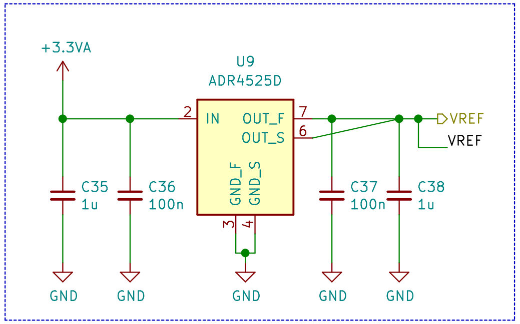

2.5V Voltage reference in hermetically sealed package
0.4 ppm
Provide cutout to reduce thermal gradients and forces coupling through substrate
(LT Application Note 82)
Decoupling provided through Class 1 MLCCs

Shield J2

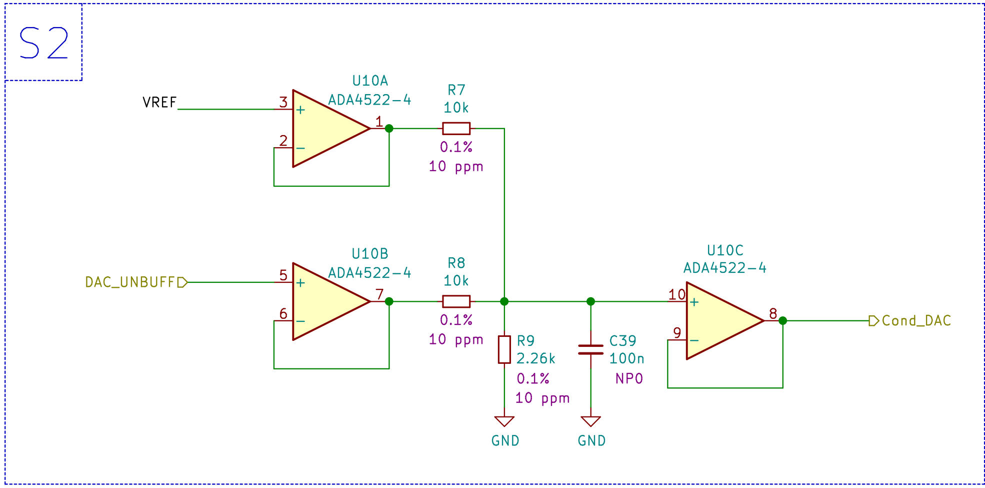

Setpoint signal conditioning
Low TC components <10 ppm
Class 1 Filter capacitor

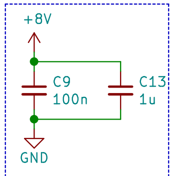

ADA4522 Decoupling

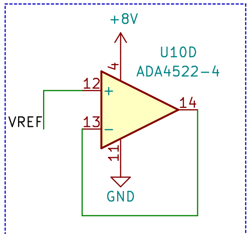

Unused OP-AMP

Approved: Iain Chalmers
Checked: Iain Chalmers
Designed: Marcin Mrozowski
Strathclyde University
Sheet: /SIGNAL_CONDITION/
File: SIGNAL_CONDITION.sch

Title: VCSEL Driver

Size: A4	Date: 2022-02-08	**Rev: 2.0.0**
KiCad E.D.A. kicad (5.1.10)-1		Id: 7/7

Bibliography

[1] É. du Trémolet de Lacheisserie, D. Gignoux, and M. Schlenker, "Magnetism, from the dawn of civilization to today", in *Magnetism*, edited by É. du Trémolet de Lacheisserie, D. Gignoux, and M. Schlenker (Springer New York, New York, NY, 2002), pp. 3–18.

[2] S. R. C. Malin and D. R. Barraclough, "150th anniversary of Gauss's first absolute magnetic measurement", Nature **297**, 285–285 (1982).

[3] J. C. Ørsted, H. C. Ørsted, K. Jelved, A. D. Jackson, O. Knudsen, and A. D. Wilson, "Experiments on the effect of a current of electricity on the magnetic needle (1820)", in *Selected scientific works of Hans Christian Ørsted* (Princeton University Press, 1998), pp. 417–420.

[4] M. Faraday, T. Martin, W. Bragg, and R. I. of Great Britain, *Faraday's Diary (7 Vol. Set): Being the Various Philosophical Notes of Experimental Investigation Made by Michael Faraday* (G. Bell and sons, Limited, 2008).

[5] D. Macaluso and O. M. Corbino, "Sopra una nuova azione che la luce subisce attraversando alcuni vapori metallici in un campo magnetico", Il Nuovo Cimento **8**, 257–258 (1898).

[6] W. E. Bell and A. L. Bloom, "Optical detection of magnetic resonance in alkali metal vapor", Physical Review **107**, 1559 (1957).

[7] S. Groeger, A. S. Pazgalev, and A. Weis, "Comparison of discharge lamp and laser pumped cesium magnetometers", Applied Physics B: Lasers and Optics **80**, 645–654 (2005).

[8] "Principles of operation of the rubidium vapor magnetometer", Applied Optics **1**, 61–68 (1962).

[9] J. Dupont-Roc, S. Haroche, and C. Cohen-Tannoudji, "Detection of very weak magnetic fields (10^{-9} gauss) by ^{87}Rb zero-field level crossing resonances", Physics Letters A **28**, 638–639 (1969).

[10] A. Kastler, "The hanle effect and its use for the measurements of very small magnetic fields", Nuclear Instruments and Methods **110**, 259–265 (1973).

[11] "Sensitive magnetometry based on nonlinear magneto-optical rotation", Physical Review A **62**, 043403 (2000).

[12] B. Chesca, R. Kleiner, and D. Koelle, "SQUID Theory", in *The SQUID Handbook* (John Wiley & Sons, Ltd, 2004) Chap. 2, pp. 29–92.

[13] J. C. Allred, R. N. Lyman, T. W. Kornack, and M. V. Romalis, "High-sensitivity atomic magnetometer unaffected by spin-exchange relaxation", Physical Review Letters **89**, 130801 (2002).

[14] I. K. Kominis, T. W. Kornack, J. C. Allred, and M. V. Romalis, "A subfemtotesla multichannel atomic magnetometer", Nature 2003 422:6932 **422**, 596–599 (2003).

[15] L. A. Liew, S. Knappe, J. Moreland, H. Robinson, L. Hollberg, and J. Kitching, "Microfabricated alkali atom vapor cells", Applied Physics Letters **84**, 2694 (2004).

[16] V. K. Shah and R. T. Wakai, "A compact, high performance atomic magnetometer for biomedical applications", Physics in Medicine & Biology **58**, 8153 (2013).

[17] M. P. Ledbetter, I. M. Savukov, D. Budker, V. Shah, S. Knappe, J. Kitching, D. J. Michalak, S. Xu, and A. Pines, “Zero-field remote detection of nmr with a microfabricated atomic magnetometer”, Proceedings of the National Academy of Sciences of the United States of America **105**, 2286–2290 (2008).

[18] S. Knappe, O. Alem, D. Sheng, and J. Kitching, “Microfabricated optically-pumped magnetometers for biomagnetic applications”, Journal of Physics: Conference Series **723**, 012055 (2016).

[19] J. Sheng, S. Wan, Y. Sun, R. Dou, Y. Guo, K. Wei, K. He, J. Qin, and J. H. Gao, “Magnetoencephalography with a Cs-based high-sensitivity compact atomic magnetometer”, Review of Scientific Instruments **88**, 094304 (2017).

[20] R. Zhang, W. Xiao, Y. Ding, Y. Feng, X. Peng, L. Shen, C. Sun, T. Wu, Y. Wu, Y. Yang, Z. Zheng, X. Zhang, J. Chen, and H. Guo, “Recording brain activities in unshielded Earth’s field with optically pumped atomic magnetometers”, Science Advances **6**, 8792–8804 (2020).

[21] T. M. Tierney, N. Holmes, S. Mellor, J. D. López, G. Roberts, R. M. Hill, E. Boto, J. Leggett, V. Shah, M. J. Brookes, R. Bowtell, and G. R. Barnes, “Optically pumped magnetometers: from quantum origins to multi-channel magnetoencephalography”, NeuroImage **199**, 598–608 (2019).

[22] H. B. Dang, A. C. Maloof, and M. V. Romalis, “Ultrahigh sensitivity magnetic field and magnetization measurements with an atomic magnetometer”, Applied Physics Letters **97**, 151110 (2010).

[23] R. Zhang, E. Klinger, F. P. Bustos, A. Akulshin, H. Guo, A. Wickenbrock, and D. Budker, “Stand-off magnetometry with directional emission from sodium vapors”, Physical Review Letters **127**, 173605 (2021).

[24] M. C. Tayler, T. Theis, T. F. Sjolander, J. W. Blanchard, A. Kentner, S. Pustelny, A. Pines, and D. Budker, “Invited review article: instrumentation

for nuclear magnetic resonance in zero and ultralow magnetic field", Review of Scientific Instruments **88**, 091101 (2017).

[25] S. Bodenstedt, M. W. Mitchell, and M. C. Tayler, "Fast-field-cycling ultralow-field nuclear magnetic relaxation dispersion", Nature Communications **12**, 1–8 (2021).

[26] L. Marmugi and F. Renzoni, "Electromagnetic induction imaging with atomic magnetometers: progress and perspectives", Applied Sciences **10**, 6370 (2020).

[27] K. Jensen, M. Zugenmaier, J. Arnbak, H. Stærkind, M. V. Balabas, and E. S. Polzik, "Detection of low-conductivity objects using eddy current measurements with an optical magnetometer", Physical Review Research **1**, 033087 (2019).

[28] F. Renzoni, L. Marmugi, and C. Deans, "Active underwater detection with an array of atomic magnetometers", Applied Optics **57**, 2346–2351 (2018).

[29] S. Afach, D. Budker, G. DeCamp, V. Dumont, Z. D. Grujić, H. Guo, D. F. J. Kimball, T. W. Kornack, V. Lebedev, W. Li, H. Masia-Roig, S. Nix, M. Padniuk, C. A. Palm, C. Pankow, A. Penaflor, X. Peng, S. Pustelny, T. Scholtes, J. A. Smiga, J. E. Stalnaker, A. Weis, A. Wickenbrock, and D. Wurm, "Characterization of the global network of optical magnetometers to search for exotic physics (GNOME)", Physics of the Dark Universe **22**, 162–180 (2018).

[30] M. E. Limes, D. Sheng, and M. V. Romalis, "He 3-Xe 129 Comagnetometery using Rb 87 Detection and Decoupling", Physical Review Letters **120**, 033401 (2018).

[31] R. M. Hill, E. Boto, M. Rea, N. Holmes, J. Leggett, L. A. Coles, M. Papastavrou, S. K. Everton, B. A. Hunt, D. Sims, J. Osborne, V. Shah, R. Bowtell, and M. J. Brookes, "Multi-channel whole-head OPM-MEG:

Helmet design and a comparison with a conventional system", NeuroImage **219**, 116995 (2020).

[32] M. S. Mrozowski, I. C. Chalmers, S. J. Ingleby, P. F. Griffin, and E. Riis, "Ultra-low noise, bi-polar, programmable current sources", Review of Scientific Instruments **94**, 014701 (2023).

[33] I. I. Sobel'man, *Atomic spectra and radiative transitions*, eng, 2nd ed.., Springer series on atoms + plasmas ; 12 (Springer-Verlag, Berlin ; New York, 1992).

[34] D. A. Steck, "Cesium D Line Data", (2019).

[35] S. J. Seltzer, "Developments in alkali-metal atomic magnetometry", PhD thesis (Princeton University, 2008).

[36] C. J. Foot, in *Atomic physics* (Oxford University Press, 2014).

[37] J. Vanier, *The quantum physics of atomic frequency standards*, eng (Hilger, Bristol, 1989).

[38] P. Bevington, "Developments in alkali-metal atomic magnetometry", PhD thesis (Strathclyde University, 2021).

[39] M. Levitt, *Spin dynamics: basics of nuclear magnetic resonance*, Spin Dynamics: Basics of Nuclear Magnetic Resonance (Wiley, 2001).

[40] H. J. Michael, *Modern spectroscopy.* eng, 2nd ed.. (John Wiley and Sons, 1992).

[41] R. J. Rafac, C. E. Tanner, A. E. Livingston, and H. G. Berry, "Fast-beam laser lifetime measurements of the cesium $6p^2P_{1/2,3/2}$ states", Phys. Rev. A **60**, 3648–3662 (1999).

[42] L. Young, W. T. Hill, S. J. Sibener, S. D. Price, C. E. Tanner, C. E. Wieman, and S. R. Leone, "Precision lifetime measurements of Cs 6p $^2P_{1/2}$ and 6p $^2P_{3/2}$ levels by single-photon counting", Phys. Rev. A **50**, 2174–2181 (1994).

[43] J. M. Amini and H. Gould, "High precision measurement of the static dipole polarizability of cesium", Physical Review Letters **91**, 153001 (2003).

[44] J. E. Simsarian, L. A. Orozco, G. D. Sprouse, and W. Z. Zhao, "Lifetime measurements of the $7p$ levels of atomic francium", Phys. Rev. A **57**, 2448–2458 (1998).

[45] U. Volz and H. Schmoranzer, "Precision lifetime measurements on alkali atoms and on helium by beam–gas–laser spectroscopy", Physica Scripta **65**, 48–56 (1996).

[46] R. F. Gutterres, C. Amiot, A. Fioretti, C. Gabbanini, M. Mazzoni, and O. Dulieu, "Determination of the ^{87}Rb $5p$ state dipole matrix element and radiative lifetime from the photoassociation spectroscopy of the Rb_2 $0_g^-(P_{3/2})$ long-range state", Phys. Rev. A **66**, 024502 (2002).

[47] R. Loudon, *The quantum theory of light*, eng, 3rd ed.., Oxford science publications (Oxford University Press, Oxford ; New York, 2000).

[48] D. Budker, *Atomic physics : an exploration through problems and solutions* (Second edition. Oxford ; New York : Oxford University Press, 2008., 2008).

[49] D. Budker, D. F. Kimball, S. M. Rochester, and J. T. Urban, "Alignment-to-orientation conversion and nuclear quadrupole resonance", Chemical Physics Letters **378**, 440–448 (2003).

[50] N. Castagna and A. Weis, "Measurement of longitudinal and transverse spin relaxation rates using the ground-state hanle effect", Physical Review A **84**, 53421 (2011).

[51] W. Hanle, "Über magnetische beeinflussung der polarisation der resonanzfluoreszenz", Zeitschrift für Physik **30**, 93–105 (1924).

[52] A. Corney, *Atomic and laser spectroscopy*, eng, Oxford Classic Texts in the Physical Sciences (Oxford University Press, Oxford, 2006).

[53] S. Y. Park, "Construction of a Single Beam SERF Magnetometer using Potassium Atoms for GNOME", PhD thesis (Oberlin College, 2019).

[54] S. Appelt, A. B.-A. Baranga, C. J. Erickson, M. V. Romalis, A. R. Young, and W. Happer, "Theory of spin-exchange optical pumping of ^{3}He and ^{129}Xe", Phys. Rev. A **58**, 1412–1439 (1998).

[55] H. N. D. Freitas, M. Oria, and M. Chevrollier, "Spectroscopy of cesium atoms adsorbing and desorbing at a dielectric surface", Applied Physics B: Lasers and Optics **75**, 703–709 (2002).

[56] V. G. Lucivero, A. Zanoni, G. Corrielli, R. Osellame, and M. W. Mitchell, "Laser-written vapor cells for chip-scale atomic sensing and spectroscopy", Optics Express **30**, 27149 (2022).

[57] R. Straessle, M. Pellaton, C. Affolderbach, Y. Pétremand, D. Briand, G. Mileti, and N. F. D. Rooij, "Microfabricated alkali vapor cell with anti-relaxation wall coating", Applied Physics Letters **105**, 043502 (2014).

[58] M. A. Rosenberry, J. P. Reyes, D. Tupa, and T. J. Gay, "Radiation trapping in rubidium optical pumping at low buffer-gas pressures", Physical Review A - Atomic, Molecular, and Optical Physics **75**, 023401 (2007).

[59] N. N. Bezuglov, A. N. Klucharev, B. Taratin, T. Stacewicz, A. F. Molisch, F. Fuso, and M. Allegrini, "Radiation trapping in an alkali-vapor-noble-gas mixture excited by a strong laser pulse", Optics Communications **120**, 249–256 (1995).

[60] A. P. Colombo, T. R. Carter, A. Borna, Y.-Y. Jau, C. N. Johnson, A. L. Dagel, and P. D. D. Schwindt, "Four-channel optically pumped atomic magnetometer for magnetoencephalography", Optics Express **24**, 15403 (2016).

[61] I. A. Sulai, Z. J. Deland, M. D. Bulatowicz, C. P. Wahl, R. T. Wakai, and T. G. Walker, "Characterizing atomic magnetic gradiometers for fetal magnetocardiography", Review of Scientific Instruments **90**, 085003 (2019).

[62] T. G. Walker and W. Happer, "Spin-exchange optical pumping of noble-gas nuclei", Reviews of Modern Physics **69**, 629 (1997).

[63] W. Happer and H. Tang, "Spin-exchange shift and narrowing of magnetic resonance lines in optically pumped alkali vapors", Physical Review Letters **31**, 273 (1973).

[64] W. Happer and A. C. Tam, "Effect of rapid spin exchange on the magnetic-resonance spectrum of alkali vapors", Physical Review A **16**, 1877 (1977).

[65] C. B. Alcock, V. P. Itkin, and M. K. Horrigan, "Vapour pressure equations for the metallic elements: 298–2500k", Canadian Metallurgical Quarterly **23**, 309–313 (2013).

[66] A. Ben-Amar Baranga, S. Appelt, M. V. Romalis, C. J. Erickson, A. R. Young, G. D. Cates, and W. Happer, "Polarization of ^{3}He by Spin Exchange with Optically Pumped Rb and K Vapors", Physical Review Letters **80**, 2801–2804 (1998).

[67] W. Happer, "Optical pumping", Reviews of Modern Physics **44**, 169 (1972).

[68] N. Beverini, P. Minguzzi, and F. Strumia, "Foreign-gas-induced cesium hyperfine relaxation", Physical Review A **4**, 550 (1971).

[69] N. D. Bhaskar, J. Pietras, J. Camparo, W. Happer, and J. Liran, "Spin destruction in collisions between cesium atoms", Physical Review Letters **44**, 930 (1980).

[70] E. Vliegen, S. Kadlecek, L. W. Anderson, T. G. Walker, C. J. Erickson, and W. Happer, "Faraday rotation density measurements of optically thick alkali metal vapors", Nuclear Instruments and Methods in Physics Research Sec-

tion A: Accelerators, Spectrometers, Detectors and Associated Equipment **460**, 444–450 (2001).

[71] A. Borna, T. R. Carter, A. P. Colombo, Y.-Y. Jau, J. McKay, M. Weisend, S. Taulu, J. M. Stephen, and P. D. D. Schwindt, "Non-invasive functional-brain-imaging with an opm-based magnetoencephalography system", PLoS ONE **15**, e0227684 (2020).

[72] V. Wienert, H. Sick, and J. zur Mühlen, "Local thermal stress tolerance of human skin", Anasthesie, Intensivtherapie, Notfallmedizin **18**, 88–90 (1983).

[73] formlabs, *Material data sheet: High Temp Resin for Heat Resistance*, Rev. 2 (2018).

[74] T. Williams, "Chapter 15 - Shielding", in *EMC for Product Designers (Fifth Edition)*, edited by T. Williams, Fifth Edition (Newnes, 2017), pp. 435–456.

[75] S. F. Watanabe and H. G. Robinson, "Motional narrowing of Zeeman resonance lineshapes. I. Theoretical development", Journal of Physics B: Atomic and Molecular Physics **10**, 931 (1977).

[76] N. Castagna, G. Bison, G. D. Domenico, A. Hofer, P. Knowles, C. Mac-Chione, H. Saudan, and A. Weis, "A large sample study of spin relaxation and magnetometric sensitivity of paraffin-coated cs vapor cells", Applied Physics B: Lasers and Optics **96**, 763–772 (2009).

[77] *795 nm, 40 mW DBR Butterfly Laser with Isolator, PM Fiber*, Rev. C, Thorlabs, Inc) (2019).

[78] G. P. Agrawal, "Chapter 6 - polarization effects", in *Nonlinear fiber optics (sixth edition)*, edited by G. P. Agrawal, Sixth Edition (Academic Press, 2019), pp. 189–244.

[79] X. Pan, H. Olesen, and B. Tromborg, "A Theoretical Model of Multielectrode DBR Lasers", IEEE Journal of Quantum Electronics **24**, 2423–2432 (1988).

[80] J. Talghader and J. S. Smith, "Thermal dependence of the refractive index of gaas and alas measured using semiconductor multilayer optical cavities", Applied Physics Letters **66**, 335–337 (1995).

[81] T. Murphy, "1.5-W Loudspeaker Amplifier Delivers Sound Performance", Analog Dialogue **32**, 5–5 (1998).

[82] R. Dawson, C. O'Dwyer, E. Irwin, M. S. Mrozowski, D. Hunter, S. Ingleby, E. Riis, and P. F. Griffin, "Automated machine learning strategies for multi-parameter optimisation of a caesium-based portable zero-field magnetometer", Sensors **23**, 4007 (2023).

[83] *MS-1L Compact Magnetic Shield*, Twinleaf LLC, `https://twinleaf.com/shield/MS-1L/`.

[84] T. W. Kornack, S. J. Smullin, S. K. Lee, and M. V. Romalis, "A low-noise ferrite magnetic shield", Applied Physics Letters **90**, 223501 (2007).

[85] *MS-1LF Ferrite Magnetic Shield*, Twinleaf LLC, `https://twinleaf.com/shield/MS-1LF/`.

[86] S. K. Lee and M. V. Romalis, "Calculation of magnetic field noise from high-permeability magnetic shields and conducting objects with simple geometry", Journal of Applied Physics **103**, 084904 (2008).

[87] M. Tröbs and G. Heinzel, "Improved spectrum estimation from digitized time series on a logarithmic frequency axis", Measurement **39**, 120–129 (2006).

[88] P. C. D. Hobbs, "Ultrasensitive laser measurements without tears", Applied Optics **36**, 903–920 (1997).

[89] W. C. Griffith, S. Knappe, J. Kitching, D. Budker, M. Romalis, W. Kornack, J. C. Allred, and M. V. Romalis, "Femtotesla atomic magnetometry in a microfabricated vapor cell", Optics Express **18**, 27167–27172 (2010).

[90] J. Kitching, “Chip-scale atomic devices”, Applied Physics Reviews **5**, 031302 (2018).

[91] *High power aluminum nitride, wraparound surface mount, precision thin film non-magnetic chip resistor*, 1, Vishay Intertechnology, Inc. (2023).

[92] A. J. Mäkinen, R. Zetter, J. Iivanainen, K. C. J. Zevenhoven, L. Parkkonen, and R. J. Ilmoniemi, “Magnetic-field modeling with surface currents. part i. physical and computational principles of bfieldtools”, Journal of Applied Physics **128**, 063906 (2020).

[93] R. Zetter, A. J. Mäkinen, J. Iivanainen, K. C. J. Zevenhoven, R. J. Ilmoniemi, and L. Parkkonen, “Magnetic field modeling with surface currents. part ii. implementation and usage of bfieldtools”, Journal of Applied Physics **128**, 063905 (2020).

[94] *895 nm, 12 mW DBR Butterfly Laser with Isolator, PM Fiber*, Rev. B, Thorlabs, Inc) (2019).

[95] *SFH 205 FA Silicon PIN Photodiode with Daylight Blocking Filter*, 1.4, OSRAM (2022).

[96] J. G. Graeme, *Photodiode amplifiers : op amp solutions*, eng (McGraw Hill, Boston, Mass., 1996).

[97] J. Lazar, P. Jedlička, O. Číp, and B. Růžička, “Laser diode current controller with a high level of protection against electromagnetic interference”, Review of Scientific Instruments **74**, 3816–3819 (2003).

[98] W. W. Sullivan, D. Mauch, A. Bullick, C. Hettler, A. Neuber, and J. Dickens, “A compact 45 kV curve tracer with picoampere current measurement capability”, Review of Scientific Instruments **84**, 034702 (2013).

[99] N. Goren, J. Avery, T. Dowrick, E. Mackle, A. Witkowska-Wrobel, D. Werring, and D. Holder, “Multi-frequency electrical impedance tomography and neuroimaging data in stroke patients”, Scientific Data **5**, 180112 (2018).

[100] T. Liu, A. Schnabel, J. Voigt, W. Kilian, Z. Sun, L. Li, and L. Trahms, "A built-in coil system attached to the inside walls of a magnetically shielded room for generating an ultra-high magnetic field homogeneity", Review of Scientific Instruments **92**, 024709 (2021).

[101] C. O'Dwyer, S. J. Ingleby, I. C. Chalmers, P. F. Griffin, and E. Riis, "A feed-forward measurement scheme for periodic noise suppression in atomic magnetometry", Review of Scientific Instruments **91**, 045103 (2020).

[102] X.-T. Xu, Z.-Y. Wang, R.-H. Jiao, C.-R. Yi, W. Sun, and S. Chen, "Ultra-low noise magnetic field for quantum gases", Review of Scientific Instruments **90**, 054708 (2019).

[103] R. Li, F. N. Baynes, A. N. Luiten, and C. Perrella, "Continuous high-sensitivity and high-bandwidth atomic magnetometer", Phys. Rev. Applied **14**, 064067 (2020).

[104] E. Boto, N. Holmes, J. Leggett, G. Roberts, V. Shah, S. S. Meyer, L. D. Muñoz, K. J. Mullinger, T. M. Tierney, S. Bestmann, G. R. Barnes, R. Bowtell, and M. J. Brookes, "Moving magnetoencephalography towards real-world applications with a wearable system", Nature **555**, 657–661 (2018).

[105] R. Hari and R. Salmelin, "Magnetoencephalography: from squids to neuroscience: neuroimage 20th anniversary special edition", NeuroImage **61**, Neuroimaging: Then, Now and the Future, 386–396 (2012).

[106] J. Belfi, G. Bevilacqua, V. Biancalana, S. Cartaleva, Y. Dancheva, and L. Moi, "Cesium coherent population trapping magnetometer for cardiosignal detection in an unshielded environment", J. Opt. Soc. Am. B **24**, 2357–2362 (2007).

[107] M. Mrozowski and I. Chalmers, *Strathclyde-eqop/vernier-current-driver: v1.1.0*, version v1.1.0, Available at https://github.com/Strathclyde-EQOP/Vernier-Current-Driver, 2022.

[108] *TPS7A470x 36-V, 1-A, 4-μVRMS, RF LDO Voltage Regulator*, Rev. F, Texas Instruments Inc. (2014).

[109] *TPS7A33–36-V, 1-A, Ultralow-Noise Negative Voltage Regulator*, Rev. C, Texas Instruments Inc. (2015).

[110] *ATmega4808/4809 Data Sheet*, Rev. C, Microchip Technology (2021).

[111] *DAC8814, Quad, Serial Input 16-Bit Multiplying Digital-to-Analog Converter*, Rev. B, Texas Instruments Inc. (2006).

[112] W. Kester, "SECTION 8-1 - Precision Measurement and Sensor Conditioning", in *Data conversion handbook*, edited by W. Kester (Newnes, Burlington, 2005), pp. 539–561.

[113] C. D. Motchenbacher and J. A. Connelly, "Low-noise electronic system design", in, Vol. 11 (John Wiley & Sons, 1993), pp. 297–298.

[114] *LTC6655LN, 0.25ppm Noise, Low Drift Precision References*, Rev. J, Analog Devices Inc. (2021).

[115] *OPAx210 2.2-nV/$\sqrt{Hz}$ Precision, Low-Power, 36-V Operational Amplifiers*, Rev. F, Texas Instruments Inc. (2021).

[116] I. A. Sulai, Z. J. DeLand, M. D. Bulatowicz, C. P. Wahl, R. T. Wakai, and T. G. Walker, "Characterizing atomic magnetic gradiometers for fetal magnetocardiography", Review of Scientific Instruments **90**, 085003 (2019).

[117] J. Karki, *Analysis of the Sallen Key architecture*, tech. rep. (Texas Instruments, Dallas, Texas 75265, 2002).

[118] D. H. Sheingold, "Impedance & admittance transformations using operational amplifiers", Lightning Empiricist **12**, 7 (1964).

[119] R. A. Pease, *A comprehensive study of the Howland current pump*, tech. rep. (National Semiconductor (now part of Texas Instruments), Dallas, Texas 75265, 2008).

[120] M. Lis, *Trade-offs Between CMOS, JFET, and Bipolar Input Stage Technology Application Report Trade-offs Between CMOS, JFET, and Bipolar Input Stage Technology*, SBOA355 (Texas Instruments, Inc, 2019).

[121] *2SA2013/2SC5566 Bipolar Transistors*, Semiconductor Components Industries (2013).

[122] M. Busier, *ThermalTrak audio output transistors*, tech. rep. (ONSEMI, 2005).

[123] *PicoScope 4262, High-Resolution USB Oscilloscope*, Pico Technology (2017).

[124] *E3620A and E3630A Non-programmable DC Power Supplies*, Keysight Technologies (2018).

[125] *B2900A Series Precision Source/Measure Unit*, Keysight Technologies (2020).

[126] D. Allan, "Statistics of atomic frequency standards", Proceedings of the IEEE **54**, 221–230 (1966).

[127] D. Howe, D. Allan, and J. Barnes, "Properties of signal sources and measurement methods", in Thirty fifth annual frequency control symposium (1981), pp. 669–716.

[128] P. A. Koss, R. T. Dinani, L. Bienstman, G. Bison, and N. Severijns, "Optical-magnetometry-based current source", Phys. Rev. Applied **16**, 014011 (2021).

[129] I. Fan, R. Behr, D. Drung, C. Krause, M. Götz, E. Pesel, and H. Scherer, "Externally Referenced Current Source With Stability Down to 1 nA/A at 50 mA", IEEE Transactions on Instrumentation and Measurement **68**, 2129–2135 (2019).

[130] *CSB Low Noise Bipolar Current Supply*, Available at https://twinleaf.com/current/CSB/, Twinleaf LLC ().

[131] *6220 DC Current Source Datasheet*, Tektronix ().

[132] *B2961B and B2962B 6.5 Digit Low Noise Power Source Datasheet*, Keysight Technologies (2022).

[133] G. Scandurra, G. Cannatà, G. Giusi, and C. Ciofi, "Programmable, very low noise current source", Review of Scientific Instruments **85**, 125109 (2014).

[134] J. Williams, *775 Nanovolt Noise Measurement for a low Noise Voltage Reference*, tech. rep. An124f (Linear Technology Corporation (now part of Analog Devices), 630 McCarthy Blvd., Milpitas, CA 95035-7417, 2009).

[135] *ADA4523-1, 36 V, Low Noise, Zero Drift Op Amp*, Rev. 0: Initial Version, Analog Devices Inc. (2020).

[136] "SECTION 5-3 - Time Domain Response", in *Op Amp Applications Handbook*, edited by W. Jung (Newnes, Burlington, 2005), pp. 323–324.

[137] M. Mrozowski and I. Chalmers, *Strathclyde-eqop/nv-hunter-voltage-probe: v1.0a*, version v1.0A, Available at https://github.com/Strathclyde-EQOP/nV-Hunter-voltage-probe, 2020.

[138] R. Hui, "Photodetectors", Introduction to Fiber-Optic Communications, 125–154 (2020).

[139] C. Cohen-Tannoudji, J. Dupont-Roc, S. Haroche, and F. Laloë, "Diverses résonances de croisement de niveaux sur des atomes pompés optiquement en champ nul. i. théorie", Revue de Physique Appliquée **5**, 95–101 (1970).

[140] J. Tang, Y. Liu, Y. Wang, B. Zhou, B. Han, Y. Zhai, and G. Liu, "Enhancement of bandwidth in spin-exchange relaxation-free (serf) magnetometers with amplitude-modulated light", Applied Physics Letters **120**, 084001 (2022).

[141] *BPW 34 S Silicon PIN Photodiode*, 1.7, OSRAM (2021).

[142] *Si photodiodes*, Hamamatsu (2021).

[143] *ADA4625, 36 V, 18 MHz, Low Noise, Fast Settling Single Supply, RRO, JFET Op Amp*, Rev. A, Analog Devices Inc. (2019).

[144] L. Orozco, "Programmable-gain transimpedance amplifiers maximize dynamic range in spectroscopy systems", Analog Dialogue **47**, 1–5 (2013).

[145] A. Devices, *LT3042, 20V, 200mA, Ultralow Noise, Ultrahigh PSRR RF Linear Regulator*, Rev. C (2021).

[146] *LT3093, -20V, 200mA, Ultralow Noise, Ultrahigh PSRR Negative Linear Regulator*, Rev. 0, Analog Devices (2019).

[147] R. A. Seymour, N. Alexander, S. Mellor, G. C. O'Neill, T. M. Tierney, G. R. Barnes, and E. A. Maguire, "Interference suppression techniques for opm-based meg: opportunities and challenges", NeuroImage **247**, 10.1016/J.NEUROIMAGE.2021.118834 (2022).

[148] *895nm Single-Mode VCSEL 895S-0000-X005*, Vixar (subsidiary of Osram) (2017).

[149] D. K. Serkland, K. M. Geib, G. M. Peake, R. Lutwak, A. Rashed, M. Varghese, G. Tepolt, and M. Prouty, "VCSELs for Atomic Sensors", (2007).

[150] *LT3092, 200mA 2-Terminal Programmable current source*, Rev. D, Linear technology (now part of Analog Devices, Inc) (2020).

[151] *Series or shunt voltage reference?*, AN4003 (Maxim Integrated (now part of Analog Devices, Inc), 2014).

[152] B. Whelan, "How to choose a voltage reference", Linear Technology Magazine **19**, 14–19 (2009).

[153] R. Fiore, *Circuit designer's notebook (piezoelectric effect in ceramic capacitors)* (American Technical Ceramics Corp., 2005), pp. 7–7.

[154] C. Shannon, "Communication in the presence of noise", Proceedings of the IRE **37**, 10–21 (1949).

[155] H. Barkhausen, *Lehrbuch der elektronen-röhren und ihrer technischen anwendungen*, Lehrbuch der elektronen-röhren und ihrer technischen anwendungen v. 3, [Textbook of Electron Tubes and their Technical Applications] (in German) (S. Hirzel, 1935).

[156] *MAX1978/MAX1979 Integrated Temperature Controllers for Peltier Modules*, 3 (2010), pp. 16–18.

[157] *Simple methods reduce input ripple for all charge pumps*, AN2027 (Maxim Integrated (now part of Analog Devices, Inc), 2003).

[158] K. Pearson, "Note on regression and inheritance in the case of two parents", Proceedings of the Royal Society of London Series I **58**, 240–242 (1895).

[159] *HYT 221 Digital Humidity and Temperature Module*, 2.3.5, Innovative Sensor Technology ().

[160] *MS5803-01BA Miniature Variometer Module*, Measurement Specialties, Inc., a TE Connectivity company (2017).

[161] P. Zhou, W. Quan, K. Wei, Z. Liang, J. Hu, L. Liu, G. Hu, A. Wang, and M. Ye, "Application of vcsel in bio-sensing atomic magnetometers", Biosensors **12**, 1098 (2022).

[162] X. Ii, Y. Zhou, X. Zhang, J. Zhang, Y. Zeng, Y. Ning, L. Wang, X. Ii, Y. Zhou, X. Zhang, J. Zhang, Y. Zeng, Y. Ning, and L. Wang, "High-power single-mode 894 nm VCSELs operating at high temperature ($>$ 2 mW @ 365 K)", Applied Physics B **128**, 16 (2022).

[163] N. Ismail, C. C. Kores, D. Geskus, M. Pollnau, C. Fabry, A. Pérot, J. M. Llorens, J. Buencuerpo, and P. A. Postigo, "Fabry-Pérot resonator: spectral line shapes, generic and related Airy distributions, linewidths, finesses, and

performance at low or frequency-dependent reflectivity", Optics Express **24**, 16366–16389 (2016).

[164] H. Lin, A. Khurram, M. D. Black-Ingersoll, and A. Valle, "Polarization and modal dynamics of multimode vertical-cavity surface-emitting lasers subject to optical feedback and current modulation", Optics Communications **350**, 178–188 (2015).

[165] T. Ackemann and M. Sondermann, "Characteristics of polarization switching from the low to the high frequency mode in vertical-cavity surface-emitting lasers", Applied Physics Letters **78**, 3574 (2001).